The Pennsylvania State University

The Graduate School

Department of Engineering Science and Mechanics

DEVELOPMENT OF A PIEZOELECTRIC ULTRASONIC ARRAY SENSOR FOR NUCLEAR REACTOR APPLICATIONS

A Dissertation in

Engineering Science and Mechanics

by

David Parks

Submitted in Partial Fulfillment
of the Requirements
for the Degree of

Doctor of Philosophy

May 2012

The dissertation of David Parks was reviewed and approved* by the following:

Bernhard R. Tittmann
Schell Professor and Professor of Engineering Science and Mechanics
Dissertation Advisor
Chair of Committee

Joseph L. Rose
Paul Morrow Professor and Professor of Engineering Science and Mechanics

Shujun Zhang
Associate Professor of Materials Science and Engineering

Albert E. Segall
Professor of Engineering Science and Mechanics

Judith A. Todd
P. B. Breneman Department Head

*Signatures are on file in the Graduate School

ABSTRACT

The recent Fukushima disaster has again demonstrated the need for improvements in nuclear power technology. The Fukushima disaster was essentially unstoppable once initiated, however the research herein has the potential to help prevent such disasters. The inflection point in the course of events which lead to the numerous explosions began with the generation of hydrogen from the zirconium alloy cladding. This hydrogen is generated when the cladding temperature exceeds specified limits, in this case due to the inability to pump coolant, and occurs with all metal cladding materials (Pool, 2011).

The objective of this dissertation is the development sensors that will greatly facilitate the design of improved nuclear materials, and as such has the potential to eliminating the danger of hydrogen release from the cladding, which represents only one of many potential benefits of in-core ultrasonic sensors. In addition to utilizing the sensors in material test reactors, their use for structural health monitoring of operating nuclear power plants is very feasible.

The research herein begins with testing of new high temperature piezoelectric materials, namely the rare earth oxyborates and bulk single crystal aluminum nitride. An extensive review of the radiation effects on piezoelectric materials is then presented and candidate materials are selected based on the knowledge obtained therein. The most promising material, aluminum nitride, is then tested in a reactor core for three months confirming its viability. Optimization of an ultrasonic phased array composed of radiation hard materials is then performed by way of diffraction beam and finite element analyses.

Contents

List of Figures

List of Tables

Acknowledgements

I would like to express my gratitude to my family for the inspiration to pursue higher education in the first place, although I was completely unreceptive to this possibility until nineteen years old. I would also like to thank them for supporting me throughout this process and listening considerately to my occasional griping.

I would also like to thank, my advisor, Dr. Bernhard Tittmann, for his patience and encouragement. Had he not suggested I obtain a PhD, and not settle for a Masters, I most likely would not have. It must be also mentioned that, Aluminum Nitride was first brought to the author's attention by Ray Blasi of Bechtel-Bettis.

Additionally I thank the remainder of my committee for their willingness to read my dissertation and provide feedback. To that end I also owe gratitude to Dr. Zhang for providing me with materials for testing, free of charge or excessive pressure for results.

1 Introduction

The aim of this dissertation is the development of a piezoelectric ultrasonic array for use in a nuclear reactor core. However, the concepts developed herein are applicable to any high temperature weakly corrosive environment. This work focuses on the use of piezoelectric ultrasonic sensors due to their ability to produce ultrasound in the MHz range, which is not readily accomplished by way of magnetostrictive transducers. The advantage of operating in this frequency range is primarily the increased spatial resolution which scales with frequency.

The remote harsh location of the reactor core suggests the use of an array sensor due to the difficulties one will encounter if mechanical translation is attempted during the ultrasonic inspection and the need for inspecting a large volume of material with a high level of spatial resolution. We consider the possibility of using a sparse array due to the high cost of each electrical lead into the reactor core and the decrease in spatial resolution with decreasing array length. As a result an increase in resolution is sought by considering sparse arrays.

One must note, that the geometry of the objects to be inspected implies that the use of guided waves has the potential to dramatically increase the imaging volume. This method would require careful consideration; particularly due to the desire to operate in immersion mode and to detect both bulk as well as surface features.

The immersion mode is preferred because it is likely to be less invasive and require the least modification to existing architecture. In this way ultrasonic sensors have

unparalleled potential for improving the safety of nuclear reactors. The improvements will come about by way of application of ultrasonic sensors in both advanced test reactors and in power reactors. The former case is the driving force for this work which has been developed in collaboration with Battelle Northwest Labs and Idaho National Labs as an advanced design for future advanced test reactor insertion (ATR). The latter case has been utilized and continues to develop.

The ultrasonic sensor will obtain valuable information several thousand times per second. The data from the pulse echo sensor will provide temperature measurements and material properties both of which are desperately needed to facilitate new physics based radiation damage models. As such this presents an alternative the use of ultrasonic sensors will move the field beyond "cook and look" procedure illustrated in Figure 1-4.

The remainder of this chapter introduces the fundamental background information, motivation and a literature review.

1.1 The Reactor Core

A sketch of a pressurized water reactor (PWR) is provided in Figure 1-1. The core is the region of primary interest in this work. In a typical (PWR) the core consists of fuel rods, composed of ^{235}U and encapsulated in a cladding material, which are immersed in a fluid coolant.

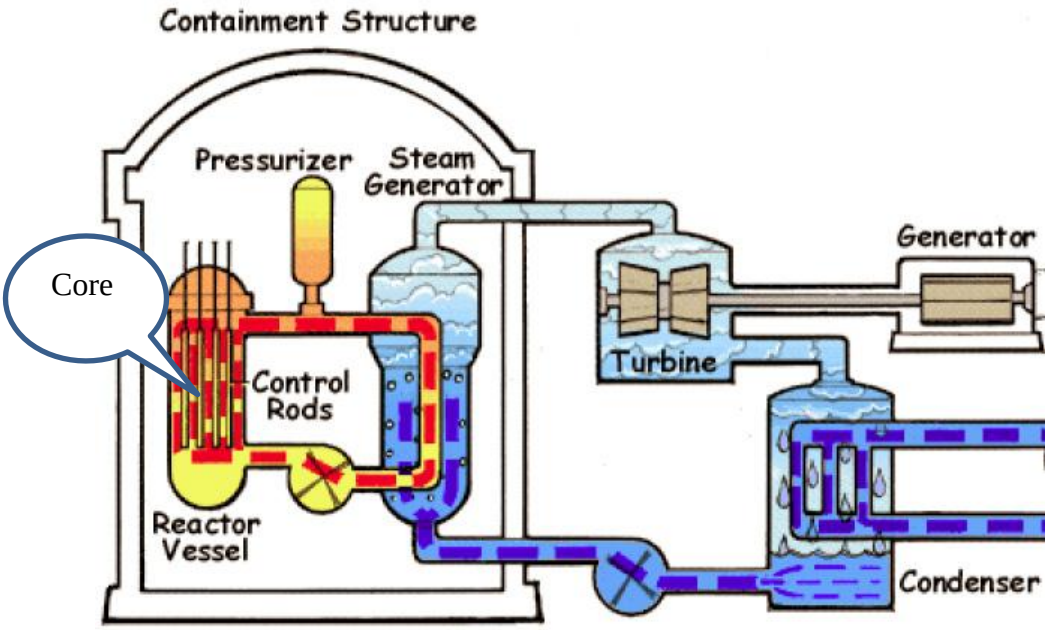

Figure 1-1: A typical pressurized water nuclear reactor

The cladding prevents the products of the ^{235}U fission from being released into the coolant and as is critical for safety purposes. A containment breach is a much more serious issue if accompanied by ruptured cladding. As one may recall there was a shortage of iodine supplements after the Fukushima disaster, which was caused by a desire to saturate the thyroid with stable iodine thereby preventing the absorption of radiative iodine isotopes that are generated in the fission process but typically contained within the cladding.

The level of enrichment and the fuel geometry are crucial and must be designed to ensure that criticality is readily achieved. Criticality is achieved when every fission generates one neutron that goes onto induce a fission. In the event that less than one fission inducing neutron is generated, referred to as subcritical, the chain reaction dies

out. Conversely if more than one fission inducing neutron is generated one has a supercritical situation and reason for concern. Fission inducing neutrons may be captured by control rods, which typically contain materials such as boron with high absorption cross sections.

Essentially every component in Figure 1-1is subject to harsh conditions which will degrade material properties overtime. For example, the pressure in a vessel in a typical pressurized light water reactor (PLWR) is typically subjected to 11 MPa at roughly 300^{o} C and may be expected to see some 10^{19} n/cm^2 (Tipping, 1996) over 40 full power years. At this fluence mitigation of embrittlement by way of thermal annealing is required. Inside the pressure vessel the flux and temperature are higher and hence material degradation is of great concern, particularly in the cladding and the fuel itself which experiences tremendous thermal gradients.

The ultimate goal of this work is to develop a means of conducting ultrasonic NDE in a material test reactor or MTR. A MTR is a ^{235}U thermal fission reactor and hence the spectrum from this type of neutron source will be utilized in calculations. Prior to moderation the ^{235}U thermal fission spectrum can be described by a Maxwellian distribution (Chilton, Shultis, & Faw, 1984) which is given by 1-1 and illustrated in Figure 1-2 where E is in MeV and T=1.29.

$$\chi(E) = \frac{1}{2\pi T^{3/2}} \sqrt{E}\, e^{-E/T}$$

1-1

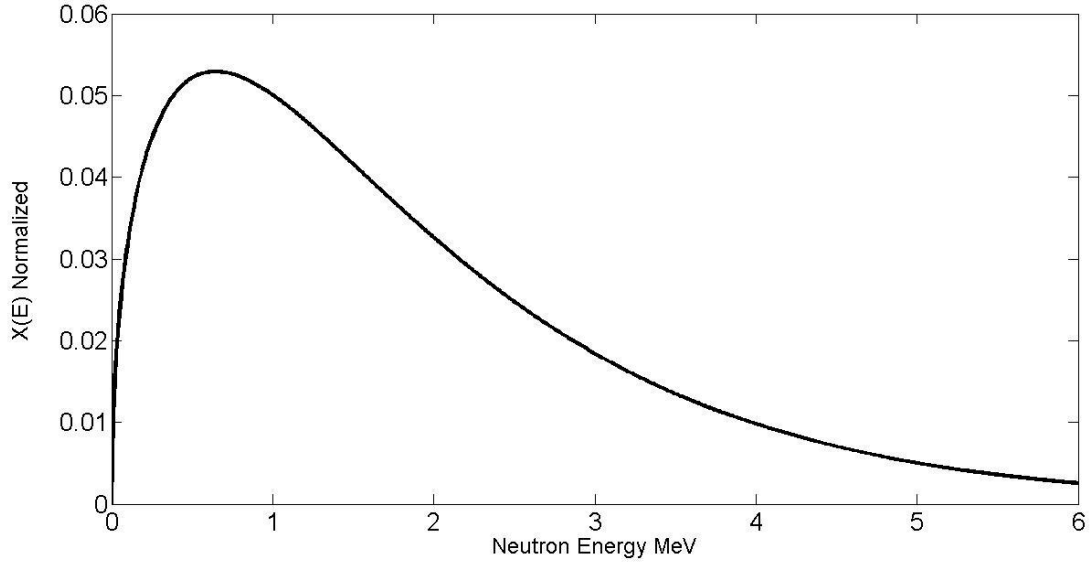

Figure 1-2: U-235 thermal fission spectrum prior to moderation

The neutrons must pass through various materials, namely the fuel cladding and possibly the moderator, before arriving at the location of the transducer. These materials distort or moderate the spectrum, resulting in peaks not only at roughly 1 MeV as a result of the initial spectrum, but an additional peak at thermal energies (0.025 eV). The 1 MeV neutrons are often referred to as "fast" neutrons and the 0.025 eV neutrons are referred to as "thermal". In the dry tube of the Penn State TRIGA reactor the flux was $4.2X10^{12}$ $n/cm^2/s$ fast, $13X10^{12}$ $n/cm^2/s$ thermal and $0.22X10^{12}$ $n/cm^2/s$ epithermal.

The nuclear cross section, σ, is an indication of the probability that a given event will occur when a material composed of the selected atoms is exposed to a neutron flux. The cross section has units of $[cm^2]$ and hence if a material of atomic density N $[\#/cm^3]$ is exposed to a fluence of neutrons φ $[n/cm^2]$ one can expect $\sigma N\varphi$ events to take place per unit volume in the material. This typical treatment assumes that the neutron flux is

constant throughout the volume of the material, which for the relatively small (largest dimensions on the order of 1") transducers given typical neutron ranges of several feet.

The fluence is a measure of total neutron exposure and is given by the flux integrated over time, often specified as thermal or fast. Common cross sections are on the order of 10^{-24} cm^2 or one barn. Common fluxes in core are 10^{12} -10^{14} $n/cm^2/s$ the goal is to ultimately develop a transducer that will withstand 10^{21} n/cm^2.

Aside from the neutron spectrum one can expect the in-core sensor to be exposed to copious amounts of gamma radiation. The vast majority of the gamma photons generated in the ^{235}U fission are in the range of 0.3 to 1 MeV. Both neutron and gamma radiation will be considered in the proceeding sections in piecemeal manner since they affect the material in their own unique ways.

Utilization of the piezoelectric sensor in a MTR reactor core demands that the piezoelectric be able to withstand temperature of up to 500^{o} C. There are many such materials; however this dissertation focuses on the following selection given in Table 1-1.

Material	Transition temperature C	Transition type	Electromechanical coupling coefficient	Problematic atomic species (ENDF)
AlN	2800-e	melt	0.2-a	^{14}N
$LiNbO_3$-b	1050-1210	Curie temperature	0.46	^{6}Li
$GaPO_4$-c	970	α–β	0.16	
Bi_3TiNbO_9-c	909	Curie temperature		
$[ReCa_4O(BO_3)_3]$-c	1500	melt	0.06-0.31	^{10}B
ZnO	~2000	melt	0.4	
$La_2Ga_5SiO_{14-d}$	1470	melt		

Table 1-1: Preliminary candidate piezoelectric materials

a-Kazys et al., (2005)
b-Wong (2002)
c-Zhang et al., (2011).
d-Zhang et al., (2008)
e-Berger (1997)

Upon the arrival of an energetic particle in the crystal lattice the following "primary" mechanisms occur (Dienes & Vineyard, 1957):

- Atomic displacements
- Ionization
- Atomic and electronic excitation without displacement
- Transmutation of Nuclei

In a reactor core neutrons will cause damage primarily by way of atomic displacements, unless high transmutation cross section materials are involved. The atomic displacement process begins with the generation of a primary knock on atom, or PKA, when a high energy neutron collides with a lattice atom. The PKA is often in a charged state and thus interacts with both the electrons and the nuclei causing a diverse array of damaging

process that will be described in chapter 3. The gamma radiation will primarily result in ionization, which can also result in lattice damage in ceramics in a process referred to as radiolysis.

A fairly general tabulation, Figure 1-3, may be made of the radiation damage processes induced by neutrons. From left to right the diagram terminates with the damage mechanism, such as a displacement cascade or radiolysis. The dominate mechanisms are in dark red blocks whereas secondary effects are in pink blocks. The blocks just after the "neutrons" block represent the so called channel, each of which is described explicitly in sections 3.2.1 through 3.2.6.

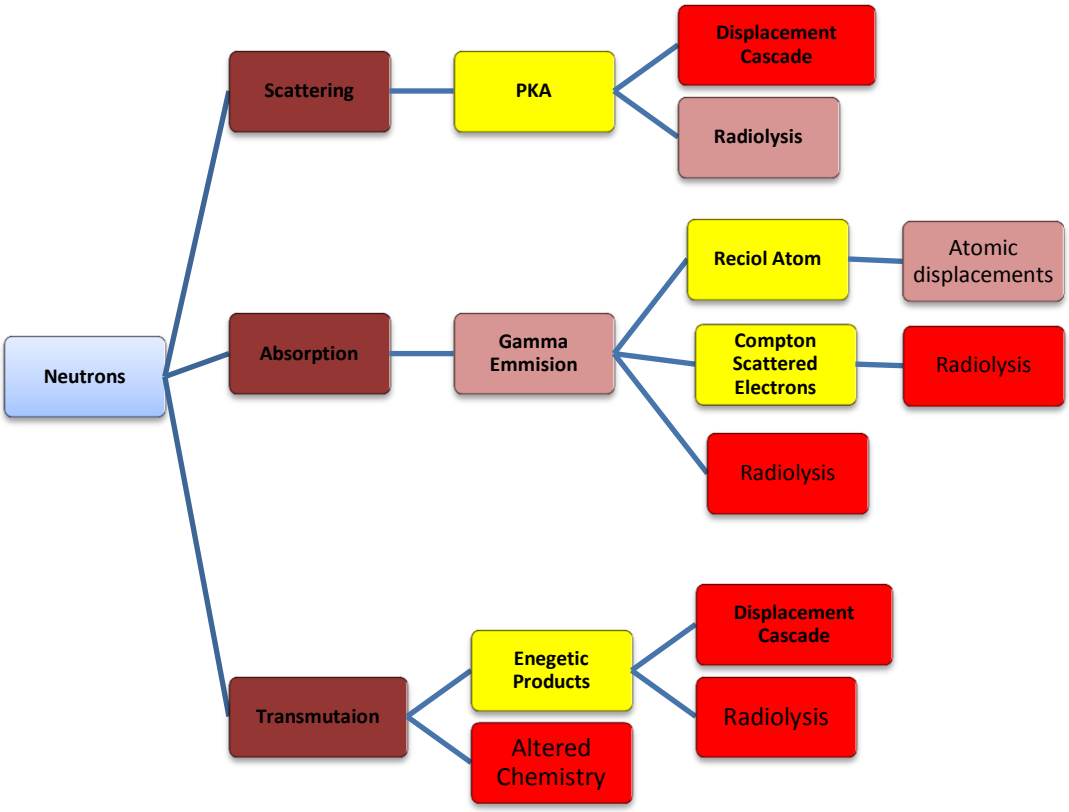

Figure 1-3: The possible damage mechanisms from neutron irradiation. Note a "displacement cascade" involves the displacement of on the order of 100 atoms, whereas "atomic displacements" refer to less than 10 displaced atoms.

It is important to separate the concept of *radiation damage* from the concept of *radiation effects.* This distinction is crucial given that damage in terms of displacements per atom assumes nothing in regard to recovery or damage morphology, and the link between *damage* and *effects* is anything but straightforward.

1.2 Background and Motivation

1.2.1 Materials Testing Reactors

Nuclear power plants of all sorts provide harsh environments in and near the core that can severely alter material performance, and limit component operational life. The currently utilized cook and look method, Figure 1-4, requires the dose rate be increased to obtain the target fluence for long term effects testing. Thus, dose rate is assumed to have no effect on the damage or is accounted for theoretically. However, improved mechanistic physics based models are desired as current approaches have failed to anticipate effects to the desired level of accuracy. To this end several Department of Energy Office of Nuclear Energy (DOE-NE) research programs have sprung up, which are calling for the evaluation of long duration radiation performance of fuels and materials.

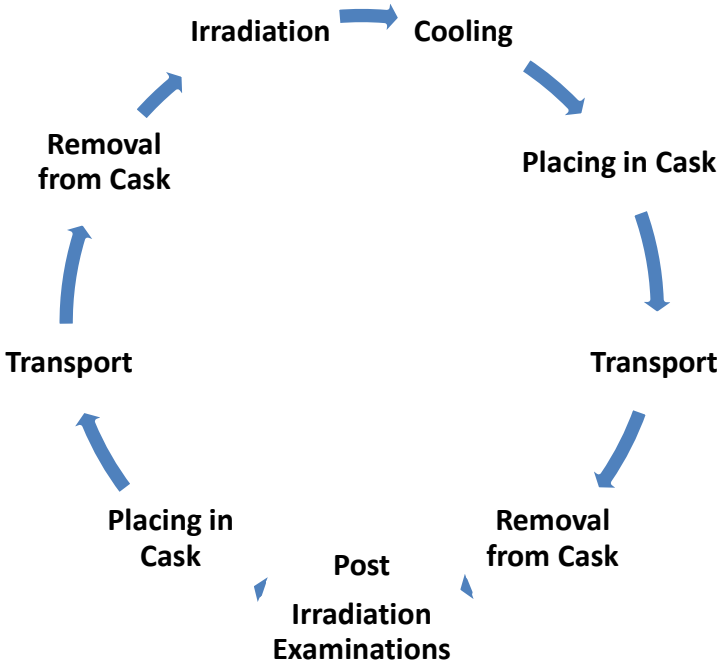

Figure 1-4: The cook and look procedure for irradiation effects analysis

Additional down sides of the cook and look procedure include: high cost, time consuming and does not allow for in flux conditions to be measured. Particularly, a single cook and look cycle investigating irradiation assisted stress corrosion cracking will take between 4 to 6 years (Sickafus, Kotomin, & Ub, 2007)

The most basic form of ultrasonic inspection, namely the A-scan, yields a wealth of data in a single waveform. These data include:

- Time of flight
    - Dimensional changes
    - Elastic moduli
    - Porosity

    - Temperature.
- Non-Linear Parameter β
    - Micro-crack formation growth
    - Dislocation density.
- Ultrasonic Attenuation
    - Porosity
    - Viscoelastic effects

This list essentially sells itself, although bringing such a method to fruition for in core applications has been delayed by the lack of a suitable ultrasonic sensor.

The physics based models, being called for by the DOE, will be facilitated by ultrasonic data in a twofold manner. First the irradiation conditions will be made known with greater certainty and resolution. Secondly, the material evolution will be tracked with time or exposure.

1.2.2 Structural Health Monitoring

There are many developed and yet unrealized applications for ultrasonic sensors in structural health monitoring of operating reactors. For example, fuel pellets undergo substantial degradation, often in the form of an increase in porosity, which has the potential to alter the reactivity adversely. To this end it has been shown that longitudinal velocity is capable of monitoring fuel pellet porosity (Phani, Sanyal, & Sengupta, 2007).

The fuel cladding has two critical tasks; containing fission products and ensuring controlled heat flux. Both of these tasks are critical to reactor safety and require the

cladding to maintain its physical integrity. Ultrasonic sensors may be used to search for rupturing which would allow the release of fission products into the primary coolant and interrupt the passage of thermal energy. The same ultrasonic sensor, likely in the form of an array, would allow for the detection of a loss of contact between the fuel and the cladding, which would cause a potentially catastrophic increase in fuel temperature.

The coolant level is naturally of utmost importance. Again, ultrasonic sensors have been utilized in numerous contexts for fluid level monitoring. The monitoring of coolant levels in a nuclear reactor is yet another application of ultrasonic sensors in a nuclear reactor, and is currently under development.

The following applications are well established:

- Condition monitoring of check valves in nuclear power plants (J. Lee, Lee, Kim, Luk, & Jung, 2006)
- Ultrasonic thermometers (Rempe 2011a)

The following applications are currently under concerted development:

- Ultrasonic fission gas release monitor (Villard & Schyns, 2009)
- Under sodium viewing transducer (Kažys, Voleišis, & Voleišienė, 2008)
- Fuel porosity measurements (Phani et al., 2007)

Moreover, offline ultrasonic inspection has been common place for quite some time. The typical offline monitoring methods are described in the text by Krautkramer (Krautkramer & Krautkramer, 1977).

1.2.3 Sparse Arrays

In many cases, including the context of this work, the desire for a beam of a specified width and a specified side lobe level for a particular application will result in a filled array possibly leaving something to be desired. For example; in ultrasonic pulse-echo breast imaging, a side lobe level of -70 dB is desired to distinguish small cysts from tumors. This is said to require 10,000 elements, which is an impractical from the standpoint of system complexity and cost (Schwartz & Steinberg, 1998). Additionally, mutual coupling effects can be lessened by use of a sparse array (Hansen, 1997). In the case of sparse arrays the benefit lies in the fact that the beam width is "strongly dependent on the source dimension but weakly dependent on the number of elements" (Bucci, 2010). On the other hand, sparse arrays may be used to lower side lobes and in fact are capable of producing both a narrower beam and a lower maximum side lobe level.

Choosing the proper distribution of the elements then becomes and nonlinear optimization problem where the number of variables is equal to the number of array elements, N, minus one if the phase and amplitude of the element excitation remains prescribed. This problem has been studied by many researchers each with their own optimization criteria.

1.3 Literature review

1.3.1.1 Radiation Damage in Ceramics

Unless specified, the JANIS (Java-based nuclear information software) software is utilized for calculations that involve nuclear data and for obtaining nuclear cross

section data from the Evaluated Nuclear data Files, (ENDF). The ENDF is a database of nuclear data available to the public on the International Atomic Energy Agency website (Evaluated Nuclear Data File (ENDF) , 2011). In the remainder of this section a literature review is presented by way of describing radiation effects with a heavy emphasis on the literature.

The effects of ionizing and displacing radiation on ceramic materials are widely varied form one ceramic to the next. The existence mixed ionic and covalent bonding is a primary cause of the increased complexity in the radiation response of ceramics, in contrast to metals with their isotropic metallic bonding (Hobbs, Clinard, Zinkle, & Ewing, 1994). The requirement of charge neutrality often results in stable lattice defects forming as a result of ionization, referred to as radiolysis. In general one is concerned with three distinct forms of metastable radiation damage;

- **isolated defects**
- **defect aggregates**
- **phase transitions.**
    - Referred to in the literature as metamictization, amorphization or phase transitioning

It is known however that high concentrations of the former two will lead to the latter, due to the increase in internal energy caused by defects, which eventually drives the solid to lower its Gibbs free energy by disordering (Sickafus, Kotomin, & Ub, 2007).

All three mechanisms have the potential to degrade the efficiency of a piezoelectric material but only phase transitions are certain to do so. Moreover isolated defects and defect aggregates are unlikely to affect the macroscopic polarization since they are highly localized as was described quantified by (C. Miclea, Tanasoiu, Miclea, Spanulescu, & Cioangher, 2005).

There have been impressive steps towards a quantitative theoretical prediction of radiation tolerance in ceramic materials. The most rigorous of these would follow the framework suggested by (Becquart, Domain, & Society, 2010). The process describe by Becquart may be a bit excessive. Moreover, the author's investigations, discussed at length in chapter 3.5.3, reveal that given equivalent radiation conditions the initial damage generation in dpa does not vary to a significant extent unless transmuting atomic species such as ^{6}Li or ^{10}B are present. Therefore the calculation of initial damage need not be done for every material individually. On the other hand the morphology of the damage and the stability of it may vary by 2 orders of magnitude (Sickafus, Kotomin, & Ub, 2007). Thermal and displacement spikes represent a particular example of morphology that we focus on in chapter 3.6 .

As mentioned above only phase transitions, specifically to the amorphous state, are certain to eliminate the piezoelectric response. Moreover, amorphization has received a generous amount of attention as it becomes of substantial importance when doping semiconductors by way of ion implantation. As a result models have been developed to predict the materials resistance to amorphization. Hobbs et al. have shown a strong correlation between the topology of the crystal structure and the radiation tolerance

(Hobbs, 1995), (Hobbs et al., 1994), (Hobbs, Jesurum, & Berger, 1999). Others have made a convincing argument that the iconicity of the chemical bonds within the material is all one needs to consider (Trachenko, 2004) (Naguib & Kelly, 1974). The two methods are undoubtedly based on the same underlying physical principle, as the nature of the bond determines the bond angles and thereby the topology.

In general the materials are more readily amorphized at lower temperatures and there is a specific temperature at which, the recrystallization rate exceeds the generation rate of amorphous material and amorphization is not possible with the available sources of damaging radiation. Examples of this critical temperature are provided in Table 1-2.

Material	Critical Temperature C^o	Reference
$LiNbO_3$	600	(Meldrum, Boatner, Weber, & Ewing, 2002)
$LiTaO_3$	650	(Meldrum et al., 2002)
$BaTiO_3$	550	(Meldrum et al., 2002)
AlN	-193	(Zingle, Snead, Eartherly, Jones, & Hensley, 1991), (Kucheyev et al., 2002)
SiO_2	1173	(L. M. Wang, Wang, Gong, Ewing, & Weber, 1998)

Table 1-2: Amorphization critical temperature of selected piezoelectric materials

Both Hobbs and Trachenko have supported their theoretical development by compiling large databases on the amorphization of various ceramics. Of particular relevance, Trachenko has reported that ZnO and AlN are radiation tolerant whereas $GaPO_4$, silicates, and titanates are not. The later three groups of materials readily form cation –O chains without concern for long range order. Additionally the Wurtzite structure is shown to be 10 times more radiation tolerant than the Perovskite materials (Hobbs et al., 1999).

Unfortunately, every rule predicting the resistance to amorphization is plagued by somewhat numerous exceptions. For example AlN should be much less resistant than observed based on the iconicity criteria (Naguib & Kelly, 1974). Trachenko has dealt with this disparity by asserting that the iconicity is calculated incorrectly by typical methods such as Pauling's electronegativity method. Trachenko then calculates the iconicity of some materials using rather involved simulations of electron density to get more agreeable results.

To predict a materials radiation tolerance by way of the topology of the crystal structure, the freedom, f a number in the range of -10 and 2 is calculated by way of combinatorial geometry. The amorphization dose is then given by (Hobbs et al., 1999)

$$f = 3 - 2.51D^{0.187}$$

1-1

where D is the dose in eV/atom. The Wurtzite structure yields f=-3 and pertains to AlN and ZnO, hence an amorphization dose of 106 eV/atom which amounts to roughly 2 displacement per atom or 2 dpa. In chapter 3 we will show that our target fluence

corresponds to roughly 1 dpa. However many researchers report that AlN cannot be amorphized even at temperatures as low as -193 C as indicated in Table 1-2.

In the case of the perovskite structure, which many high temperature piezoelectrics exhibit, Hobbs performs calculations based on the three separate polytopes that compose the structure. Once the three polytopes are considered the appropriate weighting is attempted but proves incorrect to give a result the does not agree with numerous experiments. Ultimately Hobbs determines the appropriate value for the topological freedom by examining the experimental data (Hobbs et al., 1999) and reports it as -1, giving a dose of roughly 10eV/atom or 0.2 dpa.

1.3.2 Radiation Effects in Piezoelectric Ceramics

Although the discussion of chapter 1.3.1.1 applies to piezoelectric ceramics, the focus of the publication discussed was not on the piezoelectric effect, this section discusses publications that address the effect of damaging radiation on the piezoelectric properties of materials. A somewhat chronological development is utilized.

The radiation hardness of piezoelectric sensors has been the subject of research since at least 1956 (Rogers, 1956). It appears that as was stated in the Endevco technical report 258 the effect appears to be depolarization (Thomas, 1973). In addition to depolarization the literature review conducted by the author indicates that the dielectric properties change as well. A summary of the literature can be found in Table 1-3, in this table a change in the piezoelectric response is reported if it exceeds 50%.

Material	Piezoelectric Response	Loss	Fluence	Reference
PZT (soft)	decrease	decrease	10^{18}	(C. Miclea et al., 2005)
PZT (hard)	decrease	decrease	10^{18}	(C. Miclea et al., 2005)
Barium Titanate	decrease	increase	10^{18}	(Lefkowitz, 1958)
Lithium Niobate	decrease	negligible	10^{19}	(Primak & Anderson, 1975)
Bismuth Titanate	decrease	increase	8×10^{19}	(Meleshko et al., 1986)
Strontium Niobate	decrease	increase	10^{20}	(Broomfield, 1984)

Table 1-3: summary of literature on neutron effects on piezoelectric materials

There are in fact many more papers which report radiation effects on piezoelectric materials, but the polarization and the losses are not clearly stated.

In some of earliest relevant research Rogers subjected polycrystalline ferroelectric barium titanate to in–pile radiation and performed pre/post irradiation testing of the dielectric(Rogers, 1956). It was found that the dielectric constant is reduced by the neutron bombardment and that the Curie peak disappeared from the dielectric constant versus temperature curve. This work was plagued by an atypical pre-irradition value that was not explained as pointed out by (Lefkowitz, 1958). In the following year radiation induced phase transitioning from the piezoelectric tetragonal state to the cubic state in barium titanate was observed (Wittels & Sherrill, 1957). Lefkowitz took the work a step further and measured the polarization hysterises and discovered an antiferroelectric behavior, thus linking the lattice changes measured by Wittels and Sherrill to a change in

the most relevant material property. The elimination of the ferroelectric state is consistent with the changes in the dielectric behavior observed by Rogers.

The reversibility of the radiation induced transition in barium titanate was also investigated. It was known that a metastable phase of cubic barium titanate is formed when grown from melt at 850^{o} C and the tetragonal phase is recovered from this metastable phase when the material is heated to 1000^{o} C. This recovery was not possible with the irradiated crystals.

The inability to return to the pre-irradiated state was said to be the result of generated defects which "locked-in" the room temperature state. A similar effect was also observed in quartz (Wittels & Sherril, 1954). In this work the inability to recover the pre-irradiated phase was manifested as lack of latent heat at the $\alpha \leftrightharpoons \beta$ phase transition in the quartz and was accompanied by a loss of piezoelectricity. In fact four SiO_2 structures where investigated; (1) quartz, (2) low cristobalite, (3) low tridymite, and (4) glass, all of which reduced to an isotropic glass phase. However, all the materials where successfully recrystallized after irradiation to form polycrystalline α quartz by way of annealing for 16 hours at 930^{o} C.

Early on it was realized that, in addition to damage introduced by way of energetic collisions, the altering the chemical nature of the constituent atoms when high energy photons are present is a very efficient manner of damaging some piezoelectric materials. This phenomena was investigated at length (Chynoweth, 1959) by observing the changes in the polarization hysteresis loops and by direct observation of the domain orientation in single crystal ferroelectric triglycine after x-ray and electron irradiation.

Although it is true that high energy electrons have the potential for displacing atoms this is not likely to be the cause of damage as very few atoms are displaced in this way. Rather, the segregating and reorientation of domains was attributed "ionization followed by chemical reactions resulting in molecular rearrangements". This process is referred to as radiolysis and is known to be problematic in silicates (Hobbs et al., 1994). In this context this would apply to the high quartz homeotypes such as gallium phosphate.

The effects of radiation damage on PZT were investigated by (Glower, Hester, & Warnke, 1965). Additionally, the dielectric loss was measured during irradiation and found to increase by 25% while the radiation was present, this was the only transient property observed. This is not a surprising result of the generation of electron hole pairs by way of ionizing radiation. A double hysteresis loop, characteristic of an anti-ferroelectric state was observed after irradiation, the same result was found by Chynoweth in the work described above. The results of this work show many similarities to that of Chynoweth and revealed that the material evolves into a state where the macroscopic remnant polarization of the material is dramatically reduced by the irradiation. Also notable is the fact that the fired on platinum electrodes utilized in this work withstood the irradiation, whereas Rogers had found fired on silver electrodes to transform into a "dark brown non-conducting coating".

The trend of phase transitioning due purely to radiation as opposed to bulk temperature appears to be quite common as the previous paragraphs and the review articles (Thomas, 1973) and (Anon, 1971). This is of substantial importance; given the generation of point defects and defect aggregates is frequently the crux of theoretical

treatments on radiation damage. The number of point defects and defect aggregates are known to have a dramatic effect on thermal and elastic properties, however the impact on piezoelectric properties is less well documented. However, a study conducted by (C. Miclea et al., 2005) shows that the decrease in the piezoelectric effect in PZT due to neutron irradiation anticipated from displacement damage is only 0.1% whereas the observed decrease was substantially higher. This research seems to indicate that point defects and defect aggregates are not the real issue.

Given it seems clear that the effect of radiation on piezoelectric materials appears largely due phase transitions being manifested in the piezoelectric response as an apparent depolarization, it would seem logical to select a material with a high Curie temperature. This trend has in fact been observed as stated in (Thomas, 1973) and in general the high the Curie temperature the more radiation hard the material. One such material that comes to mind is lithium niobate. A very relevant investigation was conducted on lithium niobate (Primak & Anderson, 1976), the results of which were a bit unexpected. It was found that thermal neurons very quickly reduced the crystal to a nearly isotropic state with a corresponding steep drop in the piezoelectric response. This effect was referred deemed to be metamictization, a term coined by geologist to describe crystalline minerals which contain radioactive elements that reduce the originally anisotropic crystal to an isotropic state. The radioactive elements in the metamikt mineral are in fact quite similar to instable isotopes that developed from ^{6}Li in the presence of thermal neutrons.

So it is now clear that in addition to a high Curie temperature a low neutron transmutation cross section is a requirement. The evaluated nuclear data files (ENDF), readily available online, allow one to check the atoms within any given piezoelectric for such transmutation issues. The metamictization of lithium niobate was allegedly overcome by isotope tailoring, as is reported secondhand by (Holbert, Sank, & McCready, 2005). The original report mentioned by Holbert does not appear to be available in the public realm and contacting the organization responsible for the work, Harwell U.K., has proven fruitless. A similar effort was made with AlN in which the ^{14}N was replaced with ^{15}N leaving only 0.3% ^{14}N. The isotope tailoring of AlN was motivated by a similar but much less pronounced trasnmutation cross section for ^{14}N. However, the effect of the isotope tailoring of AlN was negligible. In fact the reduction in mobility, which assists the annealing of damage, caused by the introduction of the slightly heavier ^{15}N appears to have reduced the radiation tolerance of AlN. This work investigated radiation tolerance by way of the radiation induced changes in macroscopic length changes and thermal diffusivity (Yano, Inokuchi , Shikama , & Ukai , 2004).

The work of (Kažys, Voleišis, & Voleišienė, 2008) is particularly relevant and current and as such deserves attention. This article is the only publicly available information on the effect of radiation on the piezoelectric response of AlN throughout extensive exposure. It was found that AlN thin film was completely unaffected by extensive, 18.7 MGy, γ radiation. Additionally materials; $GaPO_4$, $Bi_4Ti_3O_{12}$, PZT, and $LiNbO_3$ where tested under similar conditions. This work developed a complete ultrasonic transducer, with each of the materials listed above as the active element, and tested them in a γ field. Additionally, the transducers where subjected to temperatures of

up to 350^{o} C. Particularly important is the discussion of the coupling material which reveals that ceramic powder/silica solution type adhesives become "porous and brittle" in a radiation environment and hence should not be utilized as a couplant. In this work AlN was given the "best" rating. However, the effect of neutron irradiation was not considered.

While on the subject of AlN, the work of (Atobe, Okada, & Nakagawa, 2000) deserves mention. This work irradiated AlN in several different neutron spectra and measured the defect concentration by way of electron spin resonance (ESR). When the ESR results where compared to the predicted damage inventory it was found that only 10% of the theoretical damage was produced. It was concluded that generation of the nitrogen vacancy "center and the heavy irradiation annealing of the defect occur simultaneously under the irradiation". The author's experimental investigation of numerous AlN samples has revealed a deficiency in nitrogen is correlated with low piezo-activity and higher conductivity.

Now to return to the 80s, there was a good deal of research done in the Soviet Union and the relevant articles measured the piezoelectric response directly by way of a applying a pulse via an external device and measuring the output voltage, which is the same method utilized by Primak in his testing of lithium niobate. The most interesting aspect of this work, from the prospective of this dissertation, was the testing of bismuth titanate nobate. The bismuth titanate niobate displayed a 60% decrease in pulse conversion at 3X10^{20} n/cm^{2}, and showed a negligible decrease at 10^{19} n/cm^{2} (Meleshko, Karpechko, Leont'ev, Nalivaev, Nikiforov, & Smirnov, 1986). Additional materials

including various PZT forms where tested (Meleshko, Babaev, Karpechko, Nalivae, Safin, & Smirnov, 1984), (Baranov & Martynenko, 1982) but none faired nearly as well as the bismuth titanate niobate.

Further evidence of the stability of AlN is provided by the research of Ito (Ito, et al., 2002). In this work aluminum was irradiated with 190 keV N^+ ions. It was found that when the fluence exceeded a threshold level oriented AlN was formed. Moreover, as the fluence was increased to the point that the ion penetration depth was less than the thickness on the AlN layer the nitrogen migrated further into the Al by way of diffusion. The diffusing nitrogen formed oriented AlN beyond the penetration depth of the ions. This finding along with those of (Atobe, Okada, & Nakagawa, 2000), (Zingle et al., 1991) and (Kucheyev et al., 2002) clearly demonstrates the radiation tolerance of AlN, largely a credit to the hexagonal Wurtzite structure.

1.3.3 Ultrasonic Arrays

A book dedicated solely to high level theory and advanced methods of ultrasonic arrays does not appear to exist. However, several texts referenced frequently in this work have numerous chapters devoted to this subject; one such book is (Szabo, 2004). Additionally, with due caution, the majority of the theoretical basis needed for modeling arrays may be obtained from texts such as (Hansen, 1997), (Mahafza, 2009) and (Begaud, 2011) on electromagnetic arrays. The primary differences in the common electromagnetic array and the ultrasonic array lie in the fact that ultrasonic arrays typically rely on broadband pulses, may be operated in a regime where the Fraunhofer approximation may not be valid and may suffer due to mode conversion. However,

accounting for these differences is a very tractable task and some of these scenarios are discussed in the context of electromagnetic arrays. There are also numerous texts available from companies which manufacture and sell ultrasonic phased arrays, such as Olympus; however these books are more or less user's manuals, as the company providing the book has no desire to make their manufacturing expertise and the more esoteric nuances of ultrasonic arrays common knowledge.

1.3.4 Sparse Arrays

Past works have utilized three primary classes of sparse array; periodic, deterministic aperiodic, and random, each of which is discussed in chapter 8. It has been stated that no distribution of elements will compensate for reduced aperture efficiency (Bucci, 2010). However, a tradeoff between beam width and side lobe energy may be tailored to suit the particular application. In the literature the optimization problem is commonly referred to as array synthesis.

The general methods of array synthesis are discussed in texts by (Hansen, 1997), (Szabo, 2004), (Collin & Zucker, 1969) and (Haupt & Werner, 2007). As early as 1968, minimum redundancy arrays where investigated for observations of extragalactic radio sources (Moffet, 1968). The minimum redundancy array is defined in an absolute sense for arrays of 4 or fewer elements. Beyond 4 elements a numerical method must be used and the minimum redundancy estimated. A minimum redundancy array will give the highest possible angular resolution for a given number of elements, but little assurance is given in regard to the resulting side lobe level.

More recently a modification to the deterministic approach was presented in (Bucci, D'Urso, Isernia, Angeletti, & Toso, 2010). The deterministic approach involves mimicking an amplitude distribution by way of altering the density of elements in the array. The amplitude distributions are typically those which have been determined in a closed form from a linear optimization procedure.

The element location optimization on the other hand is a non-linear problem and as such is a prime candidate for the genetic algorithm. Relevant work on ultrasonic arrays synthesized via genetic algorithms has been presented by (Yang, Chen, & Shi, 2006). The Yang et al. synthesized several 16 element arrays with the genetic algorithm. One of the optimized arrays utilized 10 element positions as determined by Moffet and the genetic algorithm was utilized to place the remaining 6 elements. The hybrid minimum redundancy-genetic array outperformed the purely genetic arrays and the filled array in terms of spatial resolution. However, the contrast resolution appears to have been at its best with the filled array. This could be attributed to a higher side lobe level which was roughly 3 dB higher with the minimum redundancy-genetic array. However the hybrid array had the lowest side lobes and narrowest beam among the sparse arrays with a 3 dB beam width of 1.3^{o} compared to 3.3^{o} for the filled array. Additionally, Yang et al. describe an efficient method for computing the redundancy of an array regardless of array length based on the aperture distribution's autocorrelation.

In ultrasonic inspections one is typically concerned with the two way radiation pattern, which adds a degree of freedom in the array synthesis problem by allowing dissimilar transmit and receive arrays (Lockwood, Li, O'Donnell, & Foster, 1996).

Lockwood et al. assumed farfield or near focus conditions, which they pointed out are equivalent. They then showed that the effective aperture is given by cross correlation of the transmit and receive apertures. The two way beam pattern is then obtained by way of a Fourier transform of this effective aperture. In this light one may seek to find the optimum aperture based on a priori knowledge as opposed to seeking the optimum beam directly. Supporting experimental results confirmed the theoretical development.

1.4 Dissertation Impact and Scope

This dissertation reports the findings of extensive experimentation, simulation and literature review all focused on the development of an ultrasonic array for use in a nuclear reactor core. The information herein may be readily extended to any situation where an ultrasonic sensor is desired for operation in an environment comprised of relatively inert fluids and gases that regularly approaches 500^{o} C. Naturally the impact of this work extends to other environments, for example on satellites, where high levels of radiation are present.

A portion of this dissertation is committed to the optimization of an ultrasonic array for a given number of electrical channels, due to the high cost of each channel in the reactor core. This optimization is intended to be as general as possible. The generality is limited by a number of unavoidable physical realities. First of all when speaking of apertures there are three parameters that invariably will arise in any given treatment of a physically realizable situation; aperture geometry, field position and wavelength. Without defining these three parameters one cannot produce a cost function to utilize in an optimization procedure

The development of a piezoelectric sensor for use in high temperature, high radiation environments requires, as a first step, a suitable piezoelectric material. Additionally, the applications necessitate atypical passive components and design concepts. A temperature resistant and radiation hard matching layer for an immersion transducer is an excellent example of such passive component and the use of sparse array is a an example of the later. Therefore, this dissertation has two primary objectives:

- Materials Testing
- Sensor Optimization

The first objective utilizes a literature review and experimentation to develop a design premise for a single element monolithic piezoelectric sensor. A discussion on the theoretical treatment of radiation effects on piezoelectric materials is presented and radiation hardness testing of a piezoelectric transducer, composed of bulk single crystal AlN, is performed. Aside from the piezoelectric material itself, an ultrasonic sensor designed for use in a reactor core requires.

a. Radiation hard coaxial cable
b. Radiation hard ultrasonic couplant
c. Radiation hard housing
d. Radiation hard backing material

All of which have been considered and instated as explained in chapter 5.1.

Additionally, extensive testing of piezoelectric transducers at high temperatures has been conducted and is discussed herein. The high temperature testing focused on

AlN, $LiNbO_3$ and $YCa_4O(BO_3)_3$ or YCOB for short. While, AlN has been tested both at elevated temperatures (Patel & Nicholson, 1990) (Stubbs & Dutton , 1996) and in a radiation environment (Kazys, et al., 2005), the AlN has always been in thin film form, hence the issues with bulk AlN for such an application have not been researched elsewhere. The radiation testing presented in (Kazys, et al., 2005) involved only gamma and thermal neutron radiation. Moreover, the results of thermal neutrons on AlN are not presented in (Kazys, et al., 2005), rather, the fact that the testing was carried out is simply stated and one is left to speculate as to what the results were and why they are not presented.

$LiNbO_3$ is likely the most widely researched and utilized high temperature piezoelectric material. Several researchers have operated $LiNbO_3$ for short periods of time at high temperatures (Baba, Searfass, & Tittmann, 2010), (Schmarje, Kirk , & Cochran, 2007). Additionally, there have been reports which place the long term maximum operating temperature at roughly 400-600^o C due to ionic conductivity, and admittedly the conductivity appears suspect as has been shown in (Jorgensen & Bartlett, 1969). This maximum temperature has been alluded to in many publications (Holbert, Sank, & McCready, 2005), (Kažys, Voleišis, & Voleišienė, 2008), however, when Primak stated this limitation radiation effects were also presumed. Other researchers have assumed low oxygen partial pressure such as that that may be found in common hermetic packaging. A publication which decisively concludes a maximum long term operating temperature of $LiNbO_3$ as a piezoelectric ultrasonic transducer simply does not exist. However, commercial accelerometers based on $LiNbO_3$ have been rated for continuous operation up to 650^o C (Turner, Fuierer, Newnham , & Shrout, 1994), (Genral

Catalog, 1989) but we may speculate that careful packaging is utilized to elimante loss of oxygen. Moreover, it is known that $LiNbO_3$ decomposes above 600^o C (Svaasand, Eriksrud, Nakken, & Grande, 1974). This dissertation investigates the maximum long term operating temperature of $LiNbO_3$ at atmospheric oxygen partial pressure explicitly of the context of ultrasonic transduction.

YCOB is a relatively new material and has not been researched as a piezoelectric ultrasonic transducer element. This material exhibits excellent stability of piezoelectric properties in the range of room temperature up to 1000^o C and a resitivity of more than 1 MΩcm at 1000^oC (S Zhang et al., 2008).

The second primary objective of this dissertation, sensor optimization, involves modeling of phased arrays with atypical components and features as necessitated by the harsh environment. The sensor application portion is guided by the robustness requirements and by the desire to maximize inspection volume while achieving a high level of image resolution.

2 Testing of High Temperature Piezoelectric Materials

2.1 Overview of Tested Materials

Of the three materials studied in this dissertation, $LiNbO_3$ is likely the most commonly used due to its availability, affordability and strong piezoelectric response. The nominal properties of the three materials tested are provided in Table 2-1.

Material and orientation	**AlN (Z)**	**LN (Y-36^{o})**	**YCOB (XYlw -15° /45°)**
k	**0.2**	**0.46**	**0.125**
Phase Transistion [C^{o}]	**melt 2800**	**Curie temp 1150**	**melt 1500**

Table 2-1: Nominal properties of high temperature materials

The parameters in the table above are a bit limited in scope as far as indicating how well materials will actually perform in the MHz range as a transducer. For instance, the transducer will perform better when it's the electrical impedance matches that of the pulser/receiver. To get a feel for this an experiment was performed wherein the frequency and surface area of the crystals were nearly equal to roughly 9 MHz and 15 mm^2 for all three materials so that the diffraction loss and attenuation effects were similar. As a result a comparison of the echo amplitude of each piezoelectric is meaningful indicator of the performance of the piezoelectric material. The results are summarized in Table 2-2. Note the Q value is measure of the pulse bandwidth when the material is excited with a spike pulse.

Room Temp	Insertion Loss [dB]	Q	f
AlN	-69	9.5	9.5
YCOB	-81	7.4	8.8
LiNbO3	-49	9.4	8.8
500 C	**Insertion Loss [dB]**	**Q**	**f**
AlN	-82	25.9	9.1
YCOB	-93	12.9	8.5
LiNbO3	-66	19.4	8.2

Table 2-2: Insertion loss, Q value (Q), and center frequency (f) form the three materials tested at room temperature and 500^{o} C. The transducers where excited with a 100 volt spike pulser

2.2 Bulk Aluminum Nitride

This section deals with bulk AlN at high temperature, and is a summary of the findings of over 30 individual experiments, the data from a select few experiments are presented and these data are entirely representative of all the findings. Two experimental configurations are utilized, (1) adhesive couplant and (2) metal foil couplant.

2.2.1 Demonstration of High Temperature Capability

When adhesive couplant is utilized at temperatures above 300^{o} C it is safe to assume the bond will be rigid and as such necessities matching the coefficient of thermal expansion of the AlN to that of the ultrasonic propagation medium. To this end two materials have been utilized:

- Kovar (Ni 29% Co 17% Mn 0.3% Si 0.2% C<0.01% Fe balance)
    - Matched from room temperature to 400^{o} C
- SiC (polycrystalline bulk).
    - Matched from room temperature to 1000^{o} C

Both of these materials are at least semiconducting and serve as an electrode as well as the propagation medium. The upper electrode consists of a Ni based high temperature conducting adhesive. This Ni based adhesive is used to attach Ni-Cr wire leads to both electrodes which exit the furnace to meet a coaxial cable with alligator clips.

The adhesive of choice consisted of alumina particles in a silica solution. This adhesive is commercially available from Aremco and Sauereisen among other companies. Other mineral based adhesives, such as those utilizing MgO in a silica solution work as well.

The data in Figure 2-1 shows the variation in the echo amplitude versus temperature. Substantial variation is observed form one experiment to the next, as a result of varied crystal quality, and temperature ramp rate. The data in blue is the result of a relatively rapid ramp rate at more than 10^{o} C per minute.

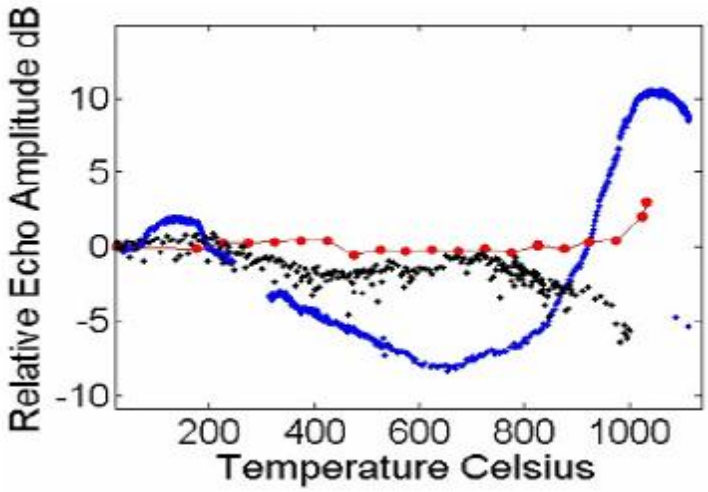

Figure 2-1: Echo amplitude from the bulk AlN transducer bonded to bulk polycrystalline SiC on 3 separate experiments

Although this experiment proves that AlN functions as an ultrasonic transducer up to 1000^{o} C it was destructive upon cooling as the crystal deboned. The waveforms corresponding to the data in red of Figure 2-1 are provided as raw waveforms in Figure 2-2. The experiments utilizing Kovar produced nearly identical results and allowed operation up to 1000^{o} C despite the thermal expansion mismatch above 400^{o} C.

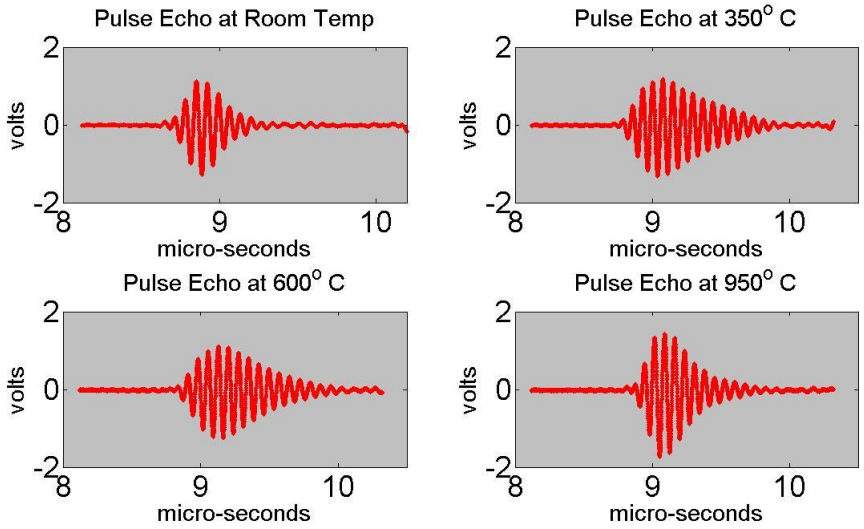

Figure 2-2: Waveforms from the bulk AlN transducer bonded to bulk polycrystalline SiC

2.2.2 Demonstration of Varied Quality and Performance

The following experiments utilized mechanical pressure provided by a spring (UNS S66286 wave spring) to compress the piezoelectric material to the ultrasonic propagation medium with roughly 150 psi. A thin piece of metal foil was used as a gasket to improve the continuity between the piezoelectric material and the propagation medium. For the experiments discussed in this chapter Al foil was utilized on an Al waveguide. In all cases the propagation medium (waveguide) cylinder was 12 mm long.

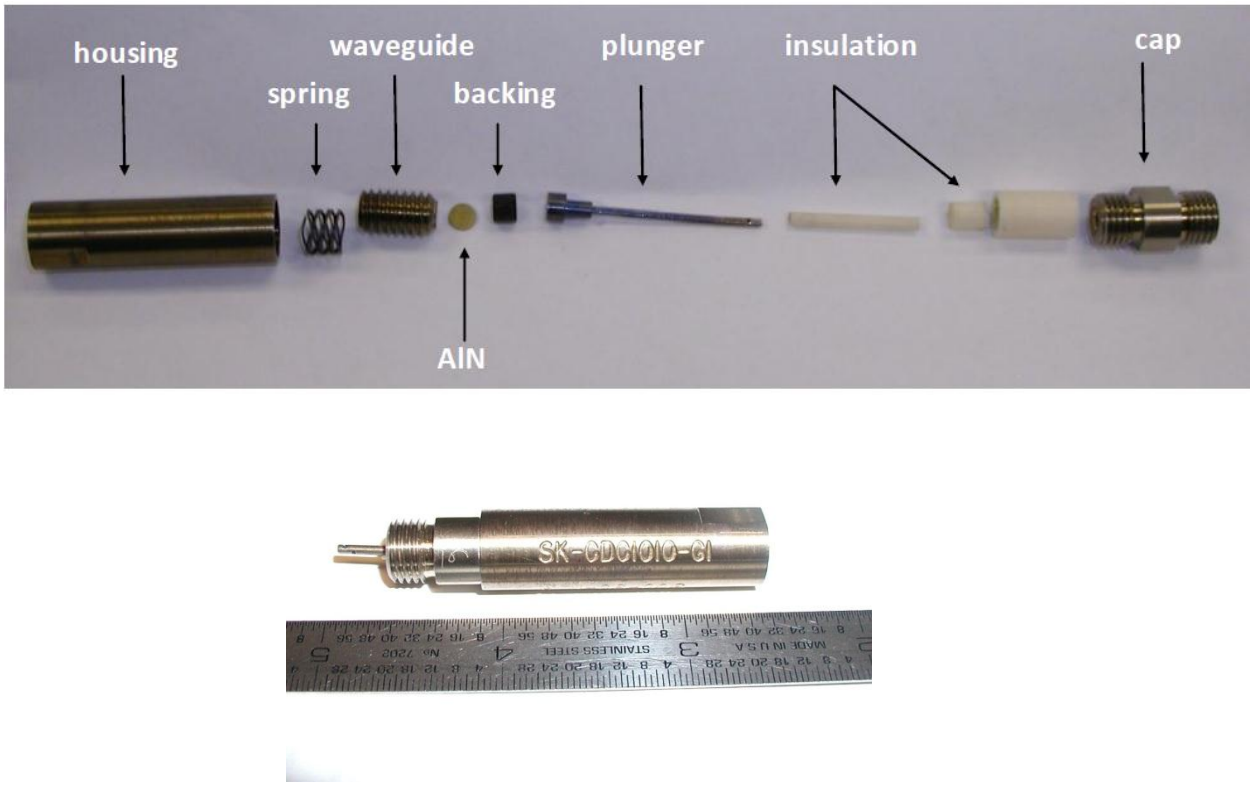

Figure 2-3**:** Experimental fixture

The arrangement shown in Figure 2-3 was constructed and the cap was tightened until a pressure of roughly 150 psi developed. The setup was then heated to roughly 500^{o} C and held there for 5 minutes. This procedure softens the aluminum foil and increases the contact pressure, improving the signal dramatically. In several experiments, the AlN was brazed securely by the procedure. The data is then obtained by cooling the setup to room temperature at a rate of roughly 5 degrees per minute.

The data of three such experiments is presented in Figure 2-4 and is consistent with numerous repetitions of the same experiment. This data shows that varied crystalline quality has a pronounced effect on the ultrasonic transduction and eventually eliminates the signal at high temperatures in some cases. As the legend in Figure 2-4

indicates the performance was strongly correlated with the elevated temperature resistivity of the samples.

The data for all the materials tested shows a decrease in signal strength at the upper and lower ends of the temperature range. This is attributed to the softening of the couplant, which h improves the signal and the softening of the spring, which degrades the signal. However, the rapid decrease in amplitude for the two low resistivity samples is due largely to the crystal itself and has been demonstrated with the adhesive type couplant as well (Parks, Tittmann, & Kropf, 2009).

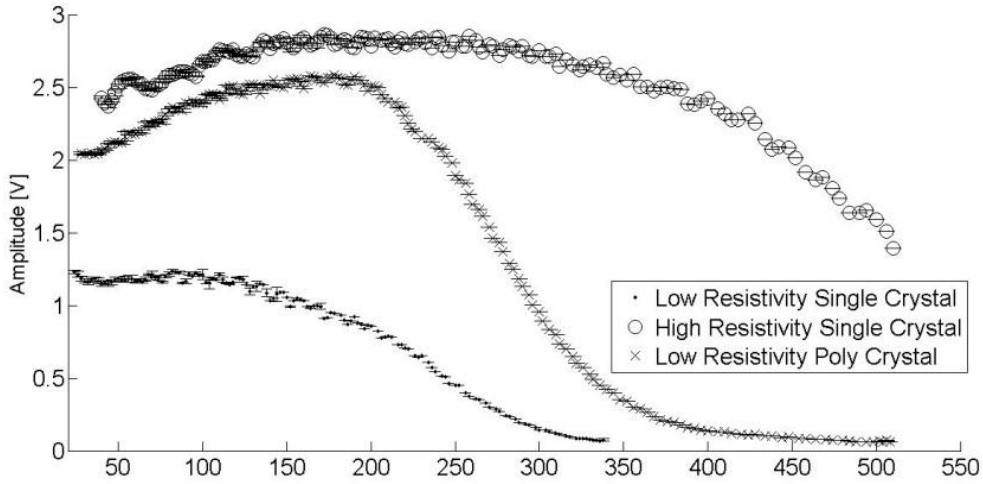

Figure 2-4: Echo amplitude obtained from 3 different bulk AlN crystals coupled to an Al cylinder via Al foil and pressure

The elevated temperature resistivity of the three samples utilized for the experiments is provided in Figure 2-5. Notice that the crystals which have poor ultrasonic transduction have resistivity 2 orders of magnitude less than the crystal which performs well for room temperature up to 500^{o} C.

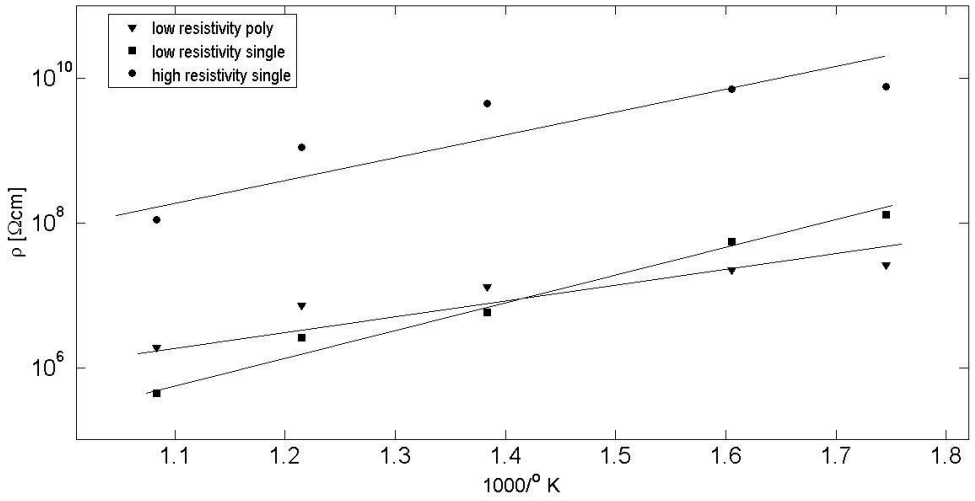

Figure 2-5: Resistivity the 3 AlN crystals tested above

Several other observations, shown in Table 2-3: Potential quality assurance parameters, have been made on various AlN crystals which may be utilized as potential guidelines for quality assurance. The date from the crystals described in rows 1, 3 and 4 are presented in this work.

Table 2-3: Potential quality assurance parameters

High Temperature Capable	**Appearance**	**frequency dependent capacitance**	**room temperature loss tangent at 1 kHz**	**d_{33} [pC/N]**	**Crystallinity**
yes	**opaque/black**	**no**	**< 0.1**	**5**	**single**
yes	**translucent/colorless**	**no**	**< 0.1**	**5**	**single**
no	**translucent/yellow**	**increases with increasing frequency**	**> 0.1**	**2**	**single**
no	**translucent/yellow**	**no**	**> 0.1**	**5**	**textured poly**

2.2.3 Defect Characterization

To get an idea as to the mechanism responsible for the low resistivity and poor transduction several AlN samples were analyzed with energy diffraction x-ray spectroscopy (EDX). This analysis provides the stoichiometry, at least near the surface, of the crystals and revealed that the samples which performed poorly possessed a deficiency of nitrogen. Additionally, it is known that the nitrogen vacancy is one to the defects commonly found in as grown samples due to its low formation energy (Rauschenbach, 2000).

2.2.4 Conclusions

Commercially available bulk AlN is of varied crystalline quality and quality assurance must be obtained for any given application. This varied crystalline quality results in poor transduction and low resistivity, both of which become more pronounced at elevated temperatures. The crystals to be avoided for this application appear to be those which contain a significant amount of nitrogen vacancies.

2.3 Rare Earth Oxyborates

The rare earth oxyborates, formula $ReCa_4O(BO_3)_3$, were first reported in 1992 (S Zhang et al., 2008). However, to date application as the active material in an ultrasonic transducer at elevated temperatures has yet to be investigated despite the lack of any phase transition up to the melting point of ~1500^o C. Additionally this family of materials possesses exceptionally high resistivity greater than 1 MΩcm exhibits less than

20% variations in the piezoelectric properties over the remarkable range of room temperature up to 1000^{o}C (S Zhang et al., 2008).

Here yttrium is utilized as the rare earth and hence $YCa_4O(BO_3)3$, or YCOB for short is tested. A double rotated cut XYlw -15° /45° was selected as it is efficient in the thickness mode, and hence is suitable for a longitudinal contact transducer(S Zhang et al., 2008). It should be note that the choice of rare earth element has a substantial effect on the piezoelectric and dielectric properties as discussed in (Shujun Zhang & Yu, 2011).

The experimental apparatus above shown in Figure 2-3 was utilized for the following experiments with the following modifications.

Waveguide: Stainless steel 316

Couplant: Ag foil

Housing: Kovar

The choice of materials above was necessitated by the melting temperature of Al which eliminated it as a possibility for use much above 600^{o} C. The waveforms obtained from this experiment are provided in Figure 2-6 and demonstrate that it is operational up to 950^{o} C.

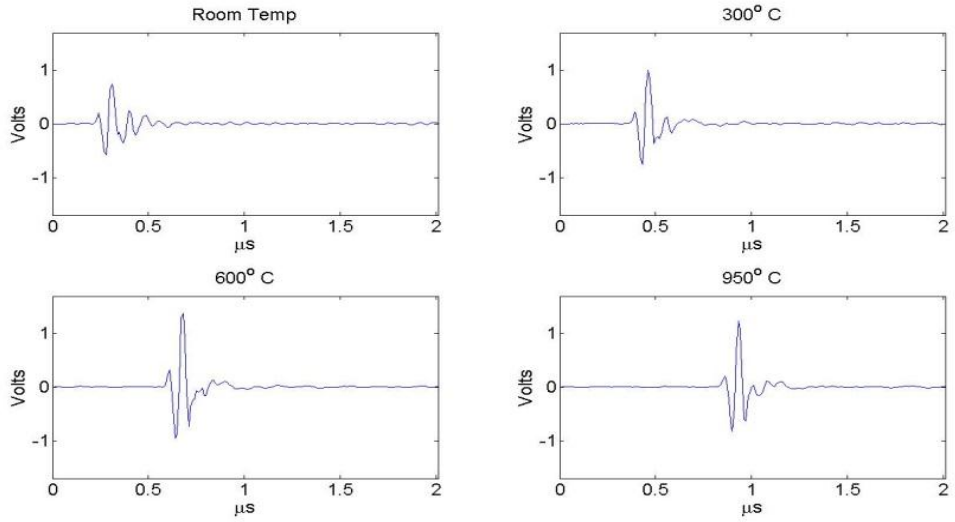

Figure 2-6: YCOB high temperature waveforms

As one can see from Figure 2-6 YCOB performs quite satisfactory up to 950^{o} C, moreover chapter 2.5.2 will reveal that this material is operable in this temperature range for extended periods of time. One also notices the ringing is substantially lower in from the YCOB, Figure 2-6, as compared to the AlN, Figure 2-2. This is likely due to the experimental configuration, as both materials are intrinsically high Q and the majority of bandwidth increases in this type of experiment are due to the external loading/damping of the crystal. One may also notice a large shift in time in Figure 2-6 as compared Figure 2-2, which is due to the greater thermal expansion in the stainless steel waveguide and a greater decease in elastic modulus with temperature. This results in a greater decrease in ultrasonic velocity and an increase in path length, hence the greater time shift with temperature.

2.4 In-Situ High Temperature Longevity Testing

The design of high temperature piezoelectric ultrasonic transducer becomes substantially more challenging when the longevity is a concern. Electrical leads begin to oxidize, structural components begin to yield and the piezoelectric may degrade. For example it has long been know that $LiNbO_3$ decomposes above 600^o C particularly at low oxygen partial pressure. Often times a sensor for use at high temperatures is hermetically sealed and low oxygen partial pressure may be expected.

The first experiment conducted monitored the pulse echo response of the AlN single crystal coupled via adhesive to the SiC. This configuration produced clear signals at 1000^o C for nearly 8 hours at which point the experiment was terminated. The relative echo amplitude is displayed in Figure 2-7, note that the initial erratic behavior corresponds to the heating which was quite rapid and corresponds to the blue curve in Figure 2-1. This experiment revealed that AlN is capable of performing at least as well as indicated by the graph. However, the numerous other features of the experimental setup also have the potential to degrade of the course of the experiment. These confounding factors drove home the importance of passive component selection and the need for a more controlled experiment.

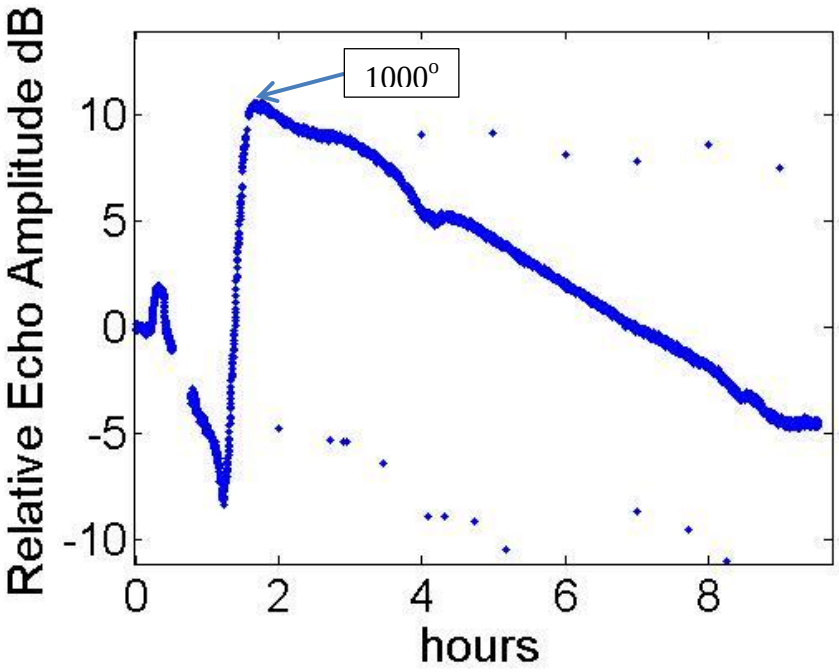

Figure 2-7: Relative echo amplitude of AlN on SiC over a period of 8 hours at 1000° C

A second attempt at in-situ high temperature longevity testing was made with the metal foil and pressure couplant fixture shown in Figure 2-3. In this case the piezoelectric was Z-cut $LiNbO_3$. The waveguide was stainless steel 316 and the foil couplant was Ag. The resulting amplitude is displayed in Figure 2-8. In this case it was observed that the spring yielded and the sintered carbon-carbon backing material had lost considerable mass and or volume. The effect on the backing material is very useful information and as a result in future applications in which longevity at elevated temperatures is needed a metal sponge type backing should be utilized.

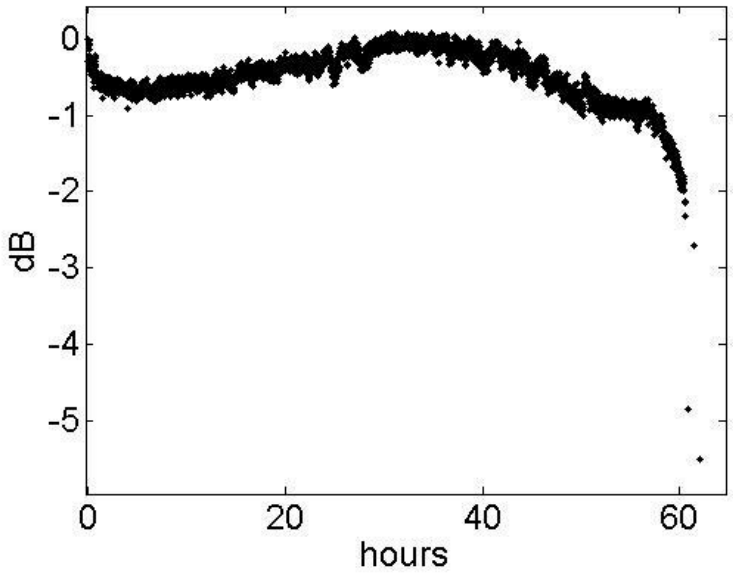

Figure 2-8: Relative echo amplitude of $LiNbO_3$ coupled via UNS S66286 spring loaded pressure and Ag foil to stainless steel 316 at 600^o C.

2.5 Cook and Look Testing

The experiments covered in the previous section have revealed the difficulty in fabricating a transducer for long term operation at high temperature due to many possible failure mechanisms. This problem may be alleviated by more careful selection of passive components. Assuming such passive components are attained the only question that remaining is that of the piezoelectric material longevity. The simplest way to determine this experimentally is to heat the piezoelectric alone and measure its performance before and after heating. The findings of chapter 2.2.2 encourage one to obtain the cook and look data at elevated temperatures as well as room temperature, as is done here and presented in chapter 2.5.2.

2.5.1 Dielectric Properties

The dielectric and piezoelectric properties of YCOB and $LiNbO_3$ where monitored for degradation when subjected to heating to 850^o C for 120 hours in air. After the heat treatment it was observed that the YCOB had gone from slightly opaque white to yellow and the $LiNbO_3$ had developed pitting that was observable with the naked eye similar to the results found in (Svaasand et al., 1974). The piezoelectric strain constant was unchanged. The effect on the dielectric properties of the two materials is displayed in Table 2-4, wherein it is clear that the $LiNbO_3$ has been damaged.

	pristine	pristine	heat treated	heat treated
frequency	capacitance [pF]	loss tangent	capacitance [pF]	loss tangent
LiNbO3	13	0.006	0.31	0.02
YCOB	7.7	0.02	7.6	0.016

Table 2-4: Effect of heat treatment on dielectric properties of the YCOB and $LiNbO_3$ (measured at 10 kHz)

2.5.2 Ultrasonic Response

The cook and look testing of ultrasonic response is conducted at room temperature and 500^o C repeatedly to obtain statistically meaningful data. This was accomplished by way of the fixture in Figure 2-3. The couplant utilized was commercially available Sono 1100 on an Al cylinder. Roughly 150 psi is applied via the spring and the capsule was then placed in the furnace at 500^o C. The couplant cures and the signal reached its optimum in roughly 1 hour and then began to degrade with complete signal loss after 3 hours.

The process was repeated for YCOB, $LiNbO_3$ and AlN after two heat treatments 1) 24 hours at 950^o C and 2) 48 hours at 1000^o C. Each test was repeated 4 times which amounts to 72 experiments. The data are presented in Figure 2-9 and Figure 2-10.

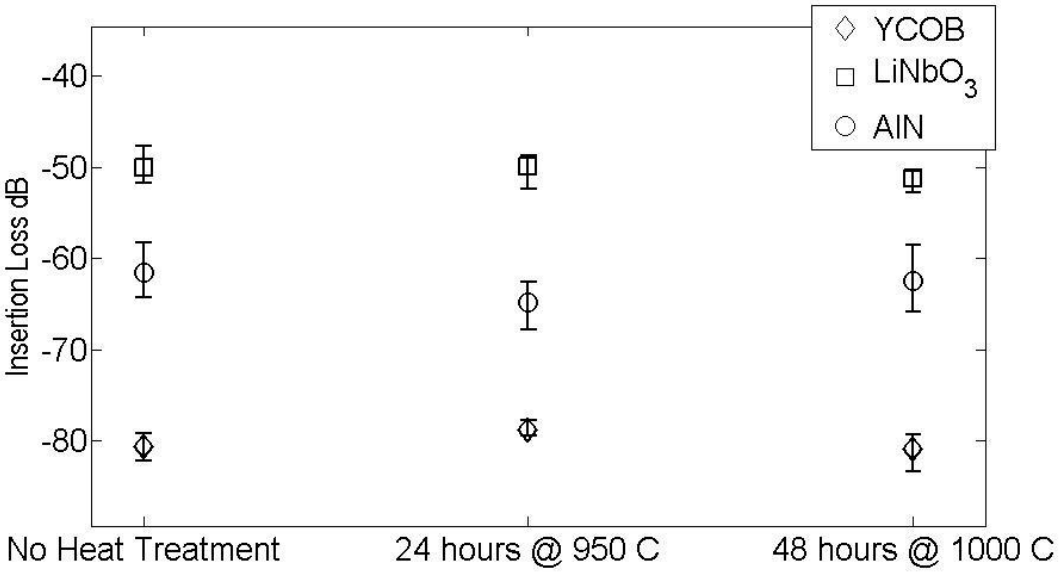

Figure 2-9: Data from the cook and look testing of piezoelectric materials, data obtained at 500^o C

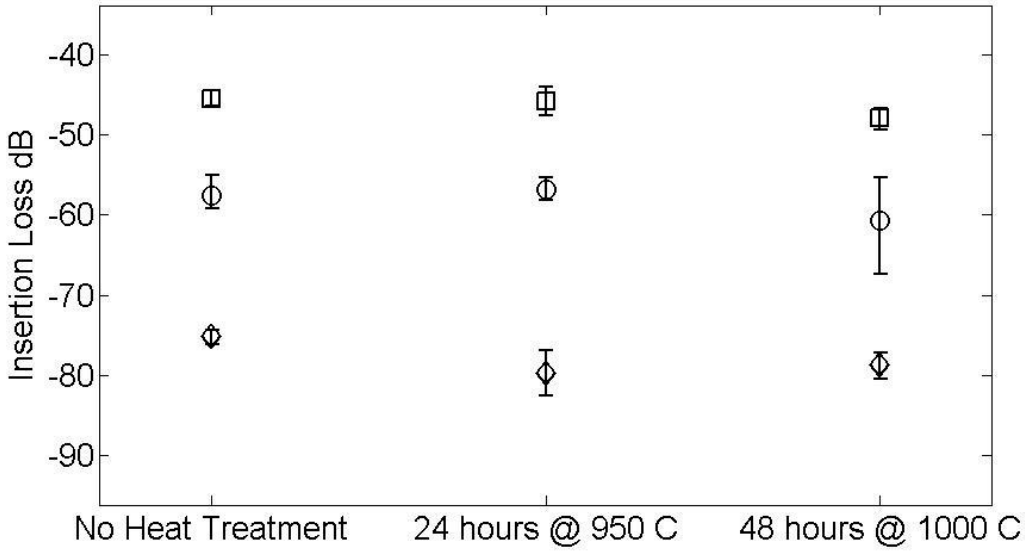

Figure 2-10: Data from the cook and look testing of piezoelectric materials, data obtained room temperature

2.5.3 Conclusion

The cook and look testing has revealed significant changes in the dielectric properties and very little changes in the ultrasonic performance of $LiNbO_3$. The dielectric changes would be expected to have a noticeable effect on the ultrasonic performance when changes of this magnitude occur and so some explanation is required. First of all, the heat treatments where not equivalent as is clear from the above discussion. Moreover the heat treatment after which dielectric properties where measure was carried out in an open tube furnace with the crystals held in a stainless steel cup and immersed in fiber glass insulation. It is quite likely that the longer heat treatment and interaction with the fiberglass caused a more pronounced change in the dielectric properties.

The YCOB on the other hand exhibited a much less pronounced change in dielectric properties after heat treatment. It is expected that YCOB is more stable at high temperatures than $LiNbO_3$ which is known to loose oxygen particularly at low oxygen partial pressure.

All three materials, YCOB, AlN and $LiNbO_3$ exhibit stability in ultrasonic performance through heat treatment. Any variations observed where less than the experimental error. The significant findings are:

- YCOB is stable in terms of ultrasonic transduction for extended periods of time up to 1000^{o} C
- The oxidation of AlN, known to occur at these temperatures, has no significant effect on the ultrasonic transduction
- At atmospheric oxygen partial pressures extend exposure to temperatures of 1000^{o} C has no significant effect on the ultrasonic transduction of $LiNbO_3$

3 Radiation Effects on Piezoelectric Materials

3.1 Introduction

This chapter is dedicated to developing a comprehensive understanding of the processes that relate changes in material properties of piezoelectric materials to the radiation field. It would be ideal to use first principles approaches to somehow reduce each candidate piezoelectric material to a simple ranking showing directly which materials one should expect to be most radiation tolerant. However, the complexity of

the problem makes such a ranking impractical and one must appeal to experimental observations. This should not be of any surprise to one whom is familiar with material science as most material properties are obtained in this manner. For example, the elastic modulus may be calculated with reasonable accuracy for simple materials based on the interatomic potential; however such calculations become more difficult as one begins to consider polyatomic materials and ultimately the values utilized in engineering practice are those obtained by way of standardized experimental procedures. However, sticking with the analogy, a theoretical understanding of the features affecting the elastic modulus facilitates the development of custom tailored materials. Therefore, this dissertation adopts a similar approach and the mechanisms affecting radiation tolerance are discussed and a good engineering sense is used for material qualification.

3.2 Neutron Interaction Channels

Impinging neutrons introduce damage to the crystal structure as a result of the following mechanisms,

- Transmutations
- Scattering (elastic and inelastic)
- Capture and gamma emission

In any given material one of the mechanisms is likely to dominate the damage generation. Each mechanism is now detailed so that a description of these processes, as they will occur in the selected materials may be confidently put forth in chapter 4.

3.2.1 Scattering

When a fast, E>0.1 MeV, neutron collides scatters of a lattice atom a primary knock on atom (PKA) is typically generated. This PKA then goes on to collide with and displace additional lattice atoms, the process is shown schematically in Figure 3-1.

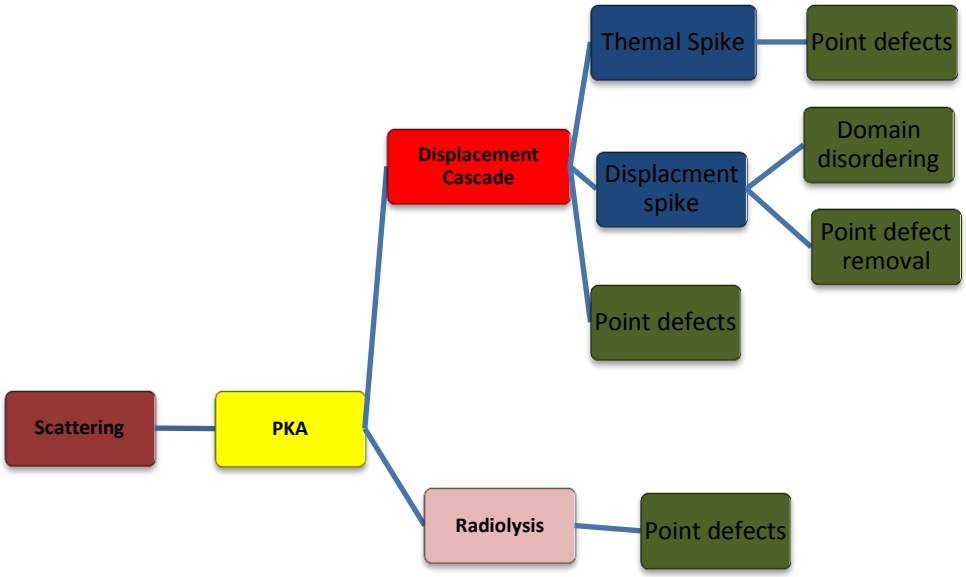

Figure 3-1: Diagram of fast neutron scattering damage generation

Fast neutrons interact with lattice primarily by way of elastic and inelastic collisions. Elastic collisions leave the nucleus in its ground state where as inelastic collisions excite the nucleus and hence some amount of the kinetic energy is lost to this excitation. Considering both possibilities, when a fast neutron with kinetic energy *E*

strikes the nucleus of a lattice atom a transfer of kinetic energy, *E'*, given by (Chilton, Shultis, & Faw, 1984)

$$E'(\omega_s, E) = \frac{1}{(A+1)^2}\left[\omega_s\sqrt{E} \pm \sqrt{E(\omega_s + A^2 - 1) + A(A+1)Q}\right]^2$$

3-1

where ω_s is the cosine of the scattering angle, *A* is the ratio of the lattice atom mass to that of a neutron and *Q* is the energy which is absorbed by the nucleus in the event of an inelastic scatter (Chilton, Shultis, & Faw, 1984). Elastic scattering is accounted for by setting *Q* equal to zero otherwise *Q* is the energy first excited state. As a result the inelastic scattering threshold is given by

$$E_t(\omega_s) = \frac{A(A+1)|Q|}{\omega_s^2 + A^2 - 1}E$$

3-2

and is on the order of 0.1 to 10 MeV. The likelihood of an elastic or inelastic scatter is given by their respective cross sections an example of which is provided in Figure 3-2.

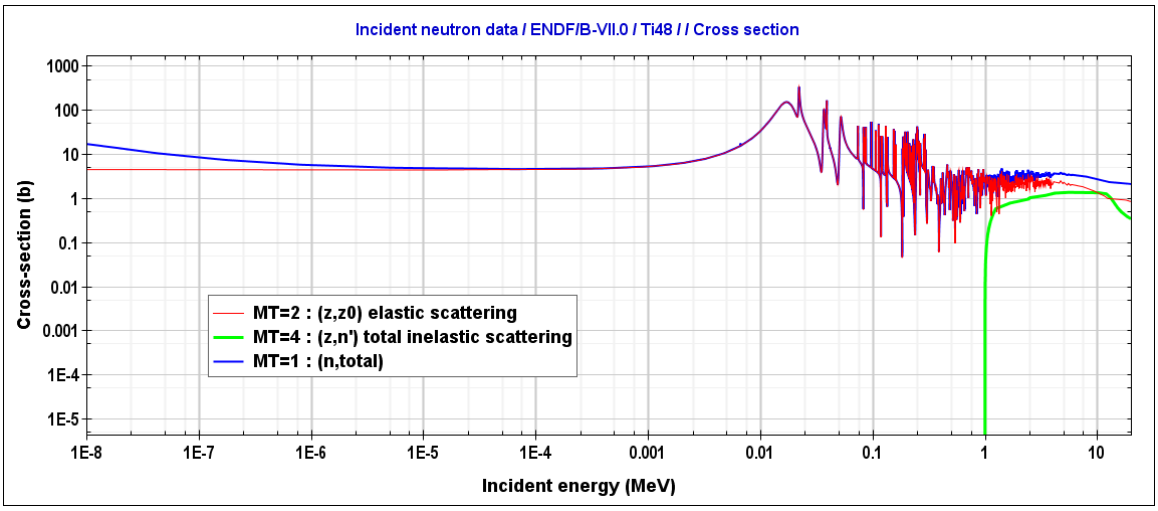

Figure 3-2: Nuclear cross sections for ^{48}Ti; red-elastic, green-inelastic, blue-total (from the JANIS software processing ENDF)

Figure 3-2 also illustrates the fact that inelastic excitation, by in large, does not occur until energies above those present in a ^{235}U thermal fission reactor are reached and when these energies are approached the interaction occur with a low probability. Also shown is the total cross section which includes transmutation and absorption. It is common that the total cross section is largely determined by the elastic scattering at higher energies (Chilton, Shultis, & Faw, 1984). The increase in the total cross section towards lower energies is due to absorption. Therefore in the case of fast neutrons, the simplest and most probable interaction is that of elastic scattering and the energy imparted to the lattice atom is thus given by (Cacuci, 2010)

$$E_{t\ elastic} = \frac{4EA}{(1+A)^2}\omega_s^2$$

3-3

The scattering cosine is somewhat of an annoyance and we m ay deal with it by assuming isotropic scattering. In the case of isotropic scattering all scattering angles are equally probable, thus we the mean value of the transferred energy is a sensible choice of transferred energy. The mean value of transferred energy is (Cacuci, 2010)

$$\bar{E}_{t\ isotropic\ elastic} = \frac{2EA}{(1+A)^2}.$$

3-4

3.2.2 Transmutations

The transmutation reactions listed in Table 3-1, which occur with thermal neutrons, are quite relevant to this work.

Reaction	Material	Reaction Probability at 0.025 eV	Product Energies
$^{6}Li(n,\alpha)^{3}T$	Lithium Niobate:	955 barns	α(2.05 MeV) T(2.75 MeV)
$^{14}N(n,p)^{14}C$	Aluminum Nitride:	1.8 barns	p(0.58 MeV) C(0.04 MeV)
$^{10}B(n,\alpha)^{7}Li$	Rare Earth Oxyborates:	3837 barns	α(1.74 MeV) Li(0.84 MeV)

Table 3-1: relevant transmutation reactions

Although the cross sections given in Table 3-1 are fairly illustrative, the atomic density of the atom of interest should be considered as well. Considering the culprit in

AlN, ^{14}N, comprises some 99.634% of the naturally occurring nitrogen, whereas ^{6}Li is only 7.5% of the natural abundance. The atomic density may be taken into account by means of a calculation of the macroscopic cross section, as given by

$$\Sigma = N\sigma \qquad 3\text{-}5$$

where N is the atomic density and σ is the transmutation cross section. Perhaps more intuitively one may consider the mean the mean free path, which is the inverse of the macroscopic cross section. The mean free path of a thermal neutron within the material represents the distance the neutron can be expected to traverse in the material before being absorbed and producing, in this case a transmutation reaction. This is calculated for AlN and $LiNbO_3$ as shown in Table 3-2.

Material → **Reaction ↓**	**$LiNbO_3$**	**AlN**
(n,α)	0.83 cm	N/A
(n,p)	>100 cm	13.1 cm

Table 3-2: Mean free path for transmutation reactions in relevant materials

3.2.3 Lithium

The reaction of ^{6}Li with thermal neutrons is quite detrimental to lithium niobate and is credited with causing a dramatic decrease in the piezoelectric response when exposed to 8 X 10^{19}n/cm^2 thermal neutrons (Primak & Anderson, 1975). The alpha particles and

tritium by in large result in ionization and thermal spikes but lack the mass to generate displacement cascades. However, the energy in the MeV energy range results in the particles ionizing along a track of rough 1 μm length at a rate of 450 eV/nm thereby generating a large thermal spike volume, see chapter 3.6.1 for a description of thermal spikes and the damage they cause. Additionally, the large cross section for this reactions means that all ^{6}Li will be replaced with helium and tritium at the fluence by the time 10^{21} n/cm^{2} is reached.

3.2.4 Boron

The rare earth oxyborates contain ^{10}B which will be subject to a reaction very similar to that of lithium described above. In fact boron absorbs thermal neutrons so well that it is utilized in control rods to absorb the thermal neutrons that would otherwise go on to cause more fission. A notable difference however occurs due to the generation of energetic lithium which will indeed cause displacement cascades given its mass. Lastly, the natural abundance of ^{10}B is 19.9% all of which will transmute by our target fluence thereby imparting significant chemical changes in the crystal.

3.2.5 Nitrogen

The transmutation, $^{14}N(n,p)^{14}C$, reaction occurring in aluminum nitride is more than a factor of 100 less likely to occur and substantially less energetic than that of the $^{6}Li(n,\alpha)^{3}H$ reaction or the $^{10}B(n,\alpha)^{7}Li$ as can be seen in Table 3-1. Literature has shown that the interaction between ^{14}N and thermal neutrons appears to play a very minor role in the damage evolution of AlN (Yano, Inokuchi , Shikama , & Ukai , 2004). The proton is generated with 580 keV and the Carbon 40 keV. The abundance of ^{14}N is 99.634% and

hence there are 4.76 X $10^{22}/cm^3$ of such species per cubic cm each of which has a cross section of 1.81 barns for this thermal neutron reaction as a result on average 0.9 protons and Carbon atoms are generated per cubic cm per thermal neutron.

SRIM indicates that the proton will cause at most one displacement due to its low mass and hence most of the energy will go towards electronic excitation at a rate of 90 eV/nm, which is insufficient for thermal spike induced phase transitioning. The Carbon on the other hand causes 140 displacements roughly 75% of which are nitrogen lattice atoms due to the closer match in mass. Each reaction generates a nitrogen vacancy and at 10^{21} and 0.18% of the nitrogen atoms have been replaced by carbon and a proton which is much less significant than the chemical changes imparted by way of boron or lithium transmutations. The 140 displacements generated each time this reaction occurs introduce 0.13 dpa at the target fluence of 10^{21} n/cm^2 and should be of little concern.

3.2.6 Neutron Capture

When a neutron, typically with thermal energies, is captured by an atom the emission of a gamma ray typically follows shortly after. The emitted gamma rays have energies in the range of 7-10 MeV (Coltman, Klabunde, & Redman, 1967) and cause the atom to recoil and thereby impart energy to the lattice. The recoil energies are on the order of 100 eV, therefore a rough estimate of the number of initially displaced atoms can be obtained by way of equation the Kinchen-Pease model or a quick SRIM calculation, both of which are described in chapter 3.5. The results show that 1 or 2 atoms are displaced. The important thing to note is that primary knock on atoms and will frequently have energies on the order of 0.01 to 10 MeV per equation 3-4 and hence the

generate damage regions which are larger by at least a 2 orders of magnitude. On the other hand emitted gamma rays may also go on to induce radiolysis and displace atoms by way of Compton scattered electrons.

3.3 Gamma Radiation Damage

In the case of gamma rays damage is primarily the result of ionization (Claeys & Simoen, 2002). Displacement is indeed caused by photons inducing Compton back scattered electrons but plays a much less significant role due to the tremendous energy needed to compensate for the mass disparity. Ionization gives rise to radiolysis due to the need for charge neutrality in ceramics, which is frequently accomplished by way of metastable defect formation.

The majority of gamma rays will be centered around 1 MeV (Dienes & Vineyard, 1957) and in this regime Compton scattering is known to dominate especially in materials containing light atoms. In the Compton regime a 1 MeV gamma ray can potentially produce an electron with comparable energies however it is more likely to produce electrons with lower energies, the probability being independent of atomic species but increasing with the mass density of the material. Additionally, the photoelectric interactions which are the second most probable in this energy regime increases strongly with density and atomic mass. For heavy atomic species with Z>100 the photoelectric effect is most probable in this energy regime.

With this in mind one would suspect materials with low density composed of low atomic number atoms to be most tolerant to gamma irradiation. This notion however,

only accounts for the amount of ionizing energy which is introduced. It is clear however, that certain materials are very susceptible to radiolysis for example, silicates (Hobbs et al., 1994). One may also speculate that the reported decrease in transduction of $GaPO_4$, $Bi_4Ti_3O_{12}$ and PZT in a gamma environment (Kazys et al., 2005) was due to radiolytic processes.

Therefore, the radiation tolerance as dictated by the interatomic bond is the deciding factor and the availability of electrons for retuning the ionized atom to a charge neutral state. For example metals are not subject to damage by way of radiolysis due to the abundance of conduction electrons. To this end the high mobility of electrons in AlN is of benefit and the material has been deemed as immune to ionizing damage by Szenes (Szenes, 2005).

3.4 Gamma Heating

In the surrounding structural components of the reactor core the heating is caused "almost entirely due to the absorption of gamma rays from the fuel" (Kok, 2009). The same will be true of the piezoelectric transducer. The materials absorb the gamma energy by way of three primary mechanisms; photoelectric effect, pair production and Compton scattering. For compounds the absorption coefficient for each of these interactions is well approximated by the weighted sum of the coefficients of the materials therein. That is (Chilton, Shultis, & Faw, 1984)

$$\frac{\mu}{\rho} = \sum_{m=1}^{M} w_m \frac{\mu_m}{\rho_m}$$

3-6

where ρ is the mass density, μ is the absorption coefficient and the index represents a material within the compound. The absorbed energy is then given by

$$q(r) = \int_0^\infty E\mu(E)\varphi(r,E)dE$$

3-7

where *E* is the energy of the gamma ray and $\varphi(r,E)$ is the flux. One may safely assume that the gamma rays are not substantially attenuated within the small piezoelectric wafer and set the flux to a constant value. Additional simplification is introduced since the majority of the gamma rays in a reactor core will be in the range of 1 MeV. The maximum temperature inside a piezoelectric plate is readily found if one assumes that the plate is infinite, that is most of the heat loss occurs on the large surface by way of convection as opposed to the thin edges of the plate (Kok, 2009).

$$T_{max} = T_{surface} + \frac{qt^2}{8k}\rho$$

3-8

where *t* is the plate thickness and *k* is the thermal conductivity. The surface temperature is given by (Kok, 2009)

$$T_{surface} = T_{ambient} + \frac{qt}{h}\rho$$

3-9

where h is the convective heat transfer coefficient, which is approximately 10 WK^{-1} m^{-2} for air.

The absorption coefficients at 1 MeV for several randomly selected atoms are listed below (Chilton, Shultis, & Faw, 1984).

element	C	N	O	Al	Fe	Pb
$\frac{\mu}{\rho}$	0.0279	0.0279	0.028	0.027	0.0264	0.0407

Table 3-3: Gamma absorption coefficients at 1 MeV for several randomly selected atoms

It is clear that there is little variation from one atom to the next until the heavy atoms are considered due to the added contribution of the photoelectric effect. In fact it is said that the heat generation rate is proportional the mass and as such the gamma radiation in a given environment is often specified in terms such as W/g. For example in the Penn State TRIGA reactor the dose rate at 1 MW was roughly 0.26 MGy/hr or 69 W/kg and thus in the steady state assuming a wafer thickness of 0.5 mm the maximum temperature of AlN and $LiNbO_3$ are 12 and 16 C^o respectively above the temperature of the surrounding air. Bismuth titanate is the densest of the materials being considering and hence may heat up a bit more. This of course a bit of a contrived situation since it assumes the wafer is floating; in reality it will be in contact with a surface that is likely to be generating more heat than the wafer itself. However, the material that is in direct contact with the piezoelectric will heat up at a rate dependent on the density and as such

presents a degree of freedom in the design. For example, if high temperatures are found to be beneficial for annealing the radiation damage one could surround the piezoelectric with a dense material. Higher irradiation temperature will reduce the likely hood of the amorphous transition but encourages depoling by way of thermal spikes.

3.5 Primary Knock on Atoms and Transmutation Products

3.5.1 Introduction

Chapter 3.2 has shown that the majority of the displacement damage is either caused by primary knock on atoms or heavy transmutation products. The PKAs from fast neutrons and the transmutation products often possess an electric charge when born. As a result energy losses to electronic excitations account for most of the initial energy loss while the particle is still moving to rapidly compared to the electron orbital velocity. This is most simply accounted for by assigning a threshold energy, $E_{C,}$ as given by equation 3-10, above which electronic excitation dominates the energy loss and atomic displacements may be neglected.

$$E_c = \frac{1}{8}\frac{M_{PKA}}{m_e} I$$

3-10

where I is the lowest excitation energy of the first main band in the optical absorption spectra of the ceramic, M_{PKA} is the PKA mass and m_e is the mass of an electron (Chadderton, 1964). This is referred to as the threshold model and in reality the transition is not a sharp one and various models have been devised to be more accurate.

In fact an even simpler rule of thumb is to assume that electronic excitation will occur if the energetic particles energy E≥ 1 keV/nucleon.

The number of displaced atoms due to a PKA or energetic transmutation product of energy *E*' is

$$N_d = 0.8\frac{E' - E_e}{2E_d}$$

3-11

where E_e represents the energy lost to electrons (Sickafus, Kotomin, & Ub, 2007). Equation 3-11 is only accurate if the displaced atoms are produced in distant regions of the lattice. If on the other hand many atomic displacements occur in a contiguous volume displacement spike effects must be considered (Dienes & Vineyard, 1957). Spikes will drastically reduce the number of metastable point defects, for example at room temperature for PKAs in alumina and magnesium oxide equation 3-11 must be scaled by roughly 0.15. This scaling factor is given the name "damage efficiency" and can vary by as much as two orders of magnitude (Sickafus, Kotomin, & Ub, 2007).

The concentration of point defects may be experimentally measured by way of resistivity (Foster & Wright Jr., 1983), microscopy (Chadderton, 1964) or optical properties (Hodgson & Agullo-Lopez, 1987) and the displacement energy, $E_{d,}$ thereby deduced. Several relevant displacement energies are listed in Table 3-4. However, it has been said that it is good practice to simply assign a constant value for the displacement threshold when comparing radiation damage amongst materials due to uncertainty in the

measured values (Sickafus, Kotomin, & Ub, 2007), an approach adopted in this work with 25 eV being chosen as such. When one wishes to carry out such an experiment electron irradiations are ideal since they only transfer enough energy to displace at one lattice atom and do not generate spikes.

Material	Element	E_d	Reference
$LiNbO_3$	Li	5-25	(S.B. Ubizskii, 2000)
	Nb	25-125	(S.B. Ubizskii, 2000)
	O	53.00	(S.B. Ubizskii, 2000)
ZnO	Zn	50	(Sickafus, Kotomin, & Ub, 2007)
	O	55	(Sickafus, Kotomin, & Ub, 2007)
AlN	Al	50.00	(P.V. Vladimirov, 1998)
	N	50.00	(P.V. Vladimirov, 1998)

Table 3-4: Displacement threshold energies for some ceramic materials

One will find ultimately that the number of displaced atoms due to fast neutrons does not vary largely from on piezoelectric material to the next. Ultimately, the materials resistance to amorphization and depoling becomes the critical factor.

3.5.2 TRIM

Equation 3-11 is useful for illustrative purposes and rough estimates; however it in only directly applies to monoatomic solids. In the case of compound materials one has to deal with the kinetics of every possible lattice atom collision with every possible PKA. The simplest solution therefore is to utilize the Monte Carlo algorithm TRIM for compound materials. TRIM software utilizes the Kinchin-Pease model described above with a more advanced calculation of the losses to electrons than that of equation 3-10 (Ziegler, Biersack, & Ziegler, 2008).

There are two primary issues that arise when utilizing the Kinchin-Pease model or SRIM for the purpose of damage calculations in solids. First, as one may notice no mention of the crystal structure is present. The crystal structure has two notable consequences, the electrons which are responsible for energy loss above the threshold energy E_C may be tied up in a bond and secondly, certain crystallographic directions may be relatively devoid of lattice atoms causing channeling effects.

SRIM deals with the double bond by way of the Core and Bond (CAB) approach which assumes, and provides plenty of supporting evidence that (Ziegler, Biersack, & Ziegler, 2008), the effect of bonding causes significant inaccuracy in Bragg's rule only when double or triple bonds are present. Note Braggs rule is a simply weighting scheme for energy loss that weights according to relative atomic density. This narrows the area

of concern somewhat to bonds between period 2 elements wherein such bonds are common. As far as the channeling effects, practically all works discussing radiation damage ignore any possibility of this. As a result to utilize SRIM with crystalline compounds one must simply be careful to enter the correct mass density and the correct CAB corrections.

With these factors considered and presumably put to rest the SRIM software is utilized as a simple example to calculate the initial damage caused in Al by 10 keV Al ions as shown in Figure 3-3.

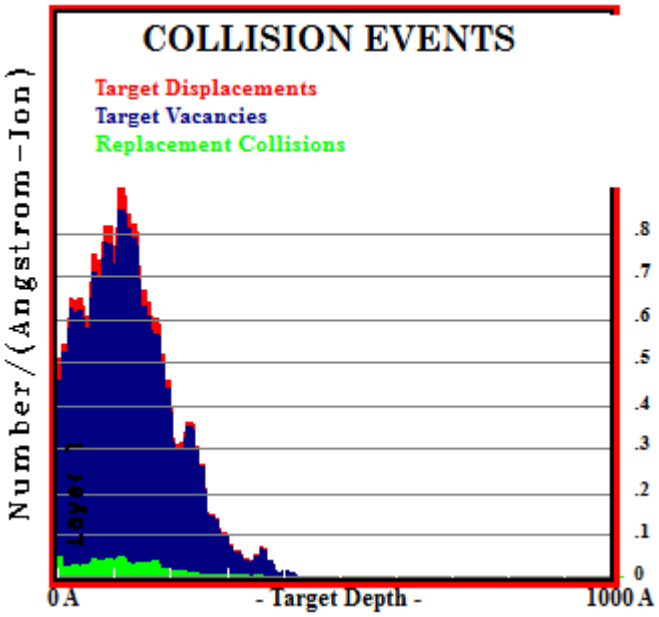

Figure 3-3: Result of a SRIM damage calculation from 10 keV Al ions into Al

Figure 3-3 shows that number of displacements per Angstrom per ion along the track of the ion and shows a peak at roughly 150 Å, which corresponds to the point at which the electronic excitation becomes insignificant. The simulation is averaged over numerous

ions, in this case 1000, and results in 169 displacements per ion. On the other hand assuming utilizing 3-11 one arrives at 160 displacements per ion and differs from the SRIM result by 6%.

3.5.3 Fast Neutron Scattering Damage Calculation Examples

The following assumptions are used herein

- Elastic scattering
    - At high energies the elastic scattering is dominant (Chilton, Shultis, & Faw, 1984), (Dienes & Vineyard, 1957)
- Isotropic scattering
    - This approximation is commonly made in neutron irradiation damage calculations (Dienes & Vineyard, 1957)

In chapter 4 the radiation tolerance of several piezoelectric materials will be considered. The initial damage introduced will be considered for the most significant neutron interaction in the given materials and will be quantified, in some cases, by the number of displacements per atom or dpa. The dpa is a useful metric for indicating the amount of *damaging* energy the lattice has absorbed. Here one assumes that a volume of material is homogeneously subjected to the *damaging* particles and only pertains to the non-ionizing energy loss. The best way to describe a calculation of dpa is to give an example, which is provided for the dpa incurred in AlN and PZT by way of fast neutron elastic scattering.

AlN

The elastic scattering cross section is spectrally averaged with the JANIS software by way of the Maxwellian spectrum centered at 1.3 MeV. The spectral averaged scattering cross sections for all the constituent naturally occurring species; ^{27}Al, ^{14}N and ^{15}N are 3, 1.6 and 2.6 barns respectively each with respective atomic densities of 2.39 X $10^{22}/cm^3$, 2.38 X $10^{22}/cm^3$ and 8.8 X $10^{19}/cm^3$. Therefore the macroscopic cross section is given by the cross section scaled by the atomic density and will give use the PKA generation rates, of which can be seen in Table 3-5. The PKA generation rate is given by the macroscopic cross section scaled by the neutron flux which we assume to be 10^{14} $n/cm^2/s$.

Isotropic scattering of a 1 MeV neutron gives the ^{27}Al, ^{14}N and ^{15}N PKAs mean energies of 74, 142 and 133 keV respectively. The SRIM software then gives 392, 280 and 286 displaced atoms as a result of the ^{27}Al, ^{14}N and ^{15}N PKAs respectively. As a result a total of $3.9X10^{15}$ displacements are produced per cubic centimeter every second, at the assumed neutron flux. If one proceeds to irradiate for 116 days the fluence obtained will arrive at 10^{21} n/cm^2 and $3.9X10^{22}$ atoms will have been displaced. Dividing the number of atoms displaced by the atomic density of the material gives the dpa, which in this case is **0.81**. The parameters and results of this calculation are provided in Table 3-5.

Isotope	Al 27	N 14	N 15
Abundance	100	99.634	0.366
Spectral Averaged C.S. barn	3	1.6	2.6
Macroscopic Cross Section [cm^{-1}]	0.0718	0.0382	0.0002
Displacement Threshold eV	50	50	50
PKA energy keV	74	142	132
PKA cm^3/s (assuming 10^{14} $n/cm^2/s$)	7.2 $x10^{12}$	3.8$x10^{12}$	2.3$x10^{10}$
Displacements caused per PKA	392	280	286

Table 3-5: Parameters and results of a fast neutron scattering damage calculation example in the case of AlN

The number 0.81 should not be taken literally to mean that 81% of the atoms have be removed from their lattice site and now reside as an interstitial as naturally there will be significant recombination due to spikes and diffusion processes. However, once the dpa exceeds unity one can say without a doubt that the material has been subjected to a significant *damaging* dose and if the material does not have an inherent ability to anneal one can be sure that an *effect* will be observed in the material properties. Specifically the material must use the spike to its advantage and not allow spikes to result in amorphization. The dpa may be converted to damaging dose by assuming equation 3-11

is valid, thus if the displacement threshold is 25 eV the dose is given by the dpa scaled by 62.5 eV/atom.

PZT

Lead zirconate titanate ($PbZr_xTi_{1-x}O_3$ $0 \leq x \leq 1$) provides an excellent opportunity to investigate the variation in dpa due to elastic scattering. The primary variable in this calculation are those of the lattice atom mass and scattering cross section. Therefore ALN and PZT are at nearly opposite extremes in terms of atomic mass.

In this example we assume the x=0.65 to correspond with the work of (Glower, 1965) in which the material depoled completely at 10^{18} n/cm^2. The table giving all the relevant parameters is provide in Appendix A and the dpa at 10^{21} n/cm^2 (1 MeV) due to fast neutron elastic scattering comes out to **0.59**. This is 27% lower than the dpa calculated for AlN. However, materials tested in the literature all lose more that 50% of the single pass efficiency at 10^{20} n/cm^{2}or lower, for example 10^{18} n/cm^2 in the case of PZT. So one sees that a factor of 27% is not the answer and in fact just focusing on dpa is misleading as this example has shown. It is then reasonable to conclude, given two extremes have been investigated, that the dpa due to 1 MeV neutron elastic scatter does not vary by the needed order of magnitude and is not of substantial interest.

3.6 Spikes, Tracks and Isolated Displacements

3.6.1 Thermal spikes

Thermal spikes are generated when an energetic charged particle imparts energy to electrons in highly localized manner. Specifically when the energy loss to electrons

reaches on the order of 10 keV/nm thermal spikes dominate and cause localized melting as the primary damage mechanism (Szenes, 2005), (Szenes, 2011). However, in the reactor core environment it is highly unlikely to find electronic energy losses reaching this level. The PKAs and transmutation products generate energy losses of several 100 eV/nm as indicated in TRIM simulations. This observation is confirmed in Friedland's article (Friedland, 2007). However, in ferroelectric materials it is reasonable to suspect that the localized heating may induce localized depoling

The heat generated in a thermal spike has been quantified (Dienes & Vineyard, 1957) and a simplified expression that assumes Dulong–Petit rule for expressing the specific heat capacity was put forth in (Szenes, 2005) and is given by

$$\Delta T(r, t=0) = \frac{0.4S}{3\pi NKa_o^2} e^{-\frac{r^2}{a_o^2}}$$

3-12

where r is the radial distance from the spike center N is the atomic density, K is Boltzmann's constant, S is the electronic energy deposition per unit length and a_o is the initial spike width that is taken as 4.5 nm for insulators and increases slightly with decreasing band gap in semiconductors. If one considers PZT SRIM reveals that the most significant spike is caused by oxygen PKAs which deposits 500 eV/nm to the lattice electrons over a range of 200 nm. The PKAs of the heavier atomic species deposit comparable energy per unit track length but travel much shorter distance thus effecting comparably insignificant volumes. The heat distribution in the spike, or more appropriately the track of an oxygen PKA in PZT is provided in Figure 3-4.

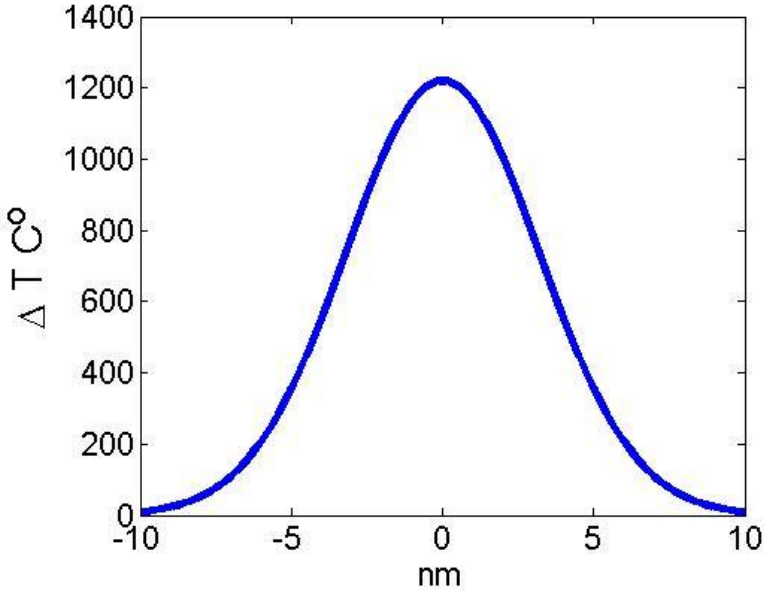

Figure 3-4: Thermal spike caused by oxygen PKA in PZT

This temperature profile corresponds to the time at which peak temperature has been reached and as time goes by the peak temperature will decrease and the width of the spike exceeding the Curie temperature will increase. If one assumes that the Curie temperature may simply replace the melting temperature for our purposes then the track radius the exceeds the Curie temperature is given by (Szenes, 2005)

$$R_e^2 = a_o^2 ln\left(\frac{S_e}{S_{et}}\right) \quad S_e < 2.7S_{et}$$

$$R_e^2 = a_o^2 \left(\frac{S_e}{2.7S_{et}}\right) \quad S_e > 2.7S_{et}$$

3-13

where S_e is the threshold energy for which the spike will exceed the Curie temperature. For PZT the threshold is found, from equation 3-12, to be 100 eV/nm. Assuming a cylindrical track, the volume which exceeds the Curie temperature of 350^o C for an irradiation temperature of 30^o C is $1.9X10^{-17}$ cm^3.

The number of PKAs per unit volume per unit fluence is given by the macroscopic cross section

$$\Sigma = N\sigma$$

3-14

where N is the atomic density and σ is the scattering cross section. For oxygen in PZT is equation 3-14 yields 0.019 [PKA/cm^3] per unit fluence in n/cm^2. Therefore each PKA depoles a region of $3.4\ X10^{-17}$ cm^3 out of a volume of $1/\Sigma$ for every unit of fast neutron fluence hence, in this case the fraction depoled is $6.5X\ 10^{-19}$ cm^2/n. Therefore at a fluence of $1.5\ X\ 10^{18}$ n/cm^2 we would expect the piezoelectric to be depoled. This is in very good agreement with the results present in Glower's article in which more than 50% of the single pass conversion efficiency is lost by 10^{18} n/cm^2.

Even more indication that we have discovered an appropriate damage mechanism is provided by the fact that Glower found that the damage rate double when the temperature was increased from room temperature by 100^o C. Referring to Figure 3-4 and equation 3-12 which represent the temperature increase beyond the irradiation temperature, the radius which exceeds 350^o, for an irradiation temperature of 130^o C is increased and the threshold is decreased to 75 ev/nm giving a depoled volume increase of 1.72, which is consistent with the observed increase in damage rate.

This model assumes complete depoling in the volume which exceeds the Curie temperature, and this is one possible source of error. The volume that exceeds the Curie temperature is likely be prevented from complete depolarization by pinning from the surrounding volume. This model seems to underestimate the radiation tolerance of the higher Curie temperature materials to some extent, which may be attributed to pinning. Alternatively, the semiconducting properties which are a present in high Curie temperature materials reduce the temperature in the thermal spike significantly as Szenes discusses. The increased threshold is introduced to the mathematical treatment by way of an increase in a_o and the reader is referred to (Szenes, 2011) for the detailed discussion.

A similar treatment for Bi_3TiNbO_9 assumes a Curie temperature of 909^o C (Shujun Zhang & Yu, 2011) and a band gap of 3.3 eV. SRIM reveals that the energy deposited to the lattice electrons, S_e, is 450 ev/nm. For the spike to exceed 909 ^{o}C the energy deposited must be 440 eV/nm. Thus the volume of spike is decreased dramatically, by both the semiconducting nature and the high Curie temperature and ends up being 2 X 10^{-20} cm^3. The macroscopic cross section for oxygen in this material is 0.0071 [PKA/cm^3] per unit fluence in n/cm^2. As a result we would expect complete depoling at 7 X 10^{21} n/cm^2 which compares to the 60% loss incurred in the single pass conversion at 8 X 10^{19} n/cm^2 as reported by (Meleshko et al., 1986). It must be mentioned that this treatment is very sensitive to the band gap of choice and if one where to assume an insulating material as opposed to a band gap of 3.3 eV the depolarization fluence would be 1 X 10^{19} n/cm^2.

In summary narrow band gap semiconductors with Curie temperatures in the range of 1000^{o} C will be completely immune to this depoling process. Moreover, the elevated irradiation temperature will cause thermal spikes to be a much greater factor. Additionally a material with a higher atomic density is resistant to this process, e.g. AlN with an atomic density of 4.78 X 10^{22} cm^{-3} as compared to Bi_3TiNbO_9. at 4.78 X 10^{21} cm^{-3}.

3.6.2 Displacement Spikes

A *displacement* spike may be assumed to occur if the mean free path for elastic collisions is small compared to the interatomic spacing. The mean free path ultimately depends on the choice of interatomic potential and the bombarding particles energy to mass ratio. At bombarding particle energies of less than 1 keV/nucleon the mean free path becomes small compared to the interatomic spacing. It has been said that Brinkman, who is credited with developing the displacement spike model, was motivated by an overestimation the repulsive force between atoms and hence a shorter mean free path (Dienes & Vineyard, 1957). In this dissertation a lengthy discussion is eschewed and the universal interatomic potential, developed by Ziegler et al., which should not be biased in any way, is utilized. The so called universal interatomic potential was developed in analogy to the many existing theoretical interatomic potentials and guided by empirical data from measured interatomic potentials of 522 randomly selected pairs of atomic species (Ziegler, Biersack, & Ziegler, 2008).

To illustrate displacement spikes and isolated displacements TRIM has been used to calculate damage generated by a PKA in Al, the PKA is assumed to have been

generated by an isotropic elastic scatter of a 1 MeV neutron. The damage is illustrated in Figure 3-5.

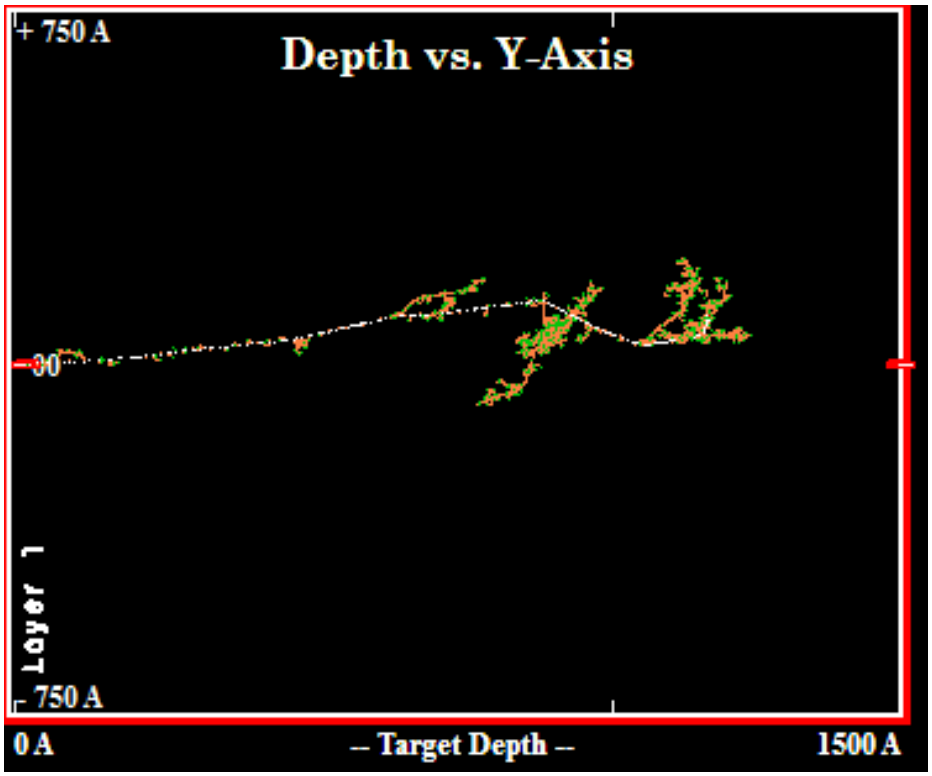

Figure 3-5: Initial damage from an Al PKA in Al illustrating the regimes of energy loss, beginning at the right with isolated point defect generation and small spikes followed by larger displacement spikes towards the end of the PKA path. Note the red atoms are still moving when the PKA comes to rest and the simulation terminates.

One can see that the Al PKA indeed does produce tight clusters of displaced atoms towards the end of its track after the PKA energy has dropped well below the ionization threshold and one may consider this region to consist of *displacement* spikes.

In the displacement spike regions it assumed that melting occurs and upon solidification the original lattice provides an "ideal nucleus for crystallization" and hence

for the most part order is maintained however small disoriented domains will occur in some fraction of the solidified spike volume (Brinkman, 1954).

The likelihood that the "highly disordered mixed soup of the constituent elements of the material" (Trachenko, 2004) will return to it desired form may be deduced from crystal topology (Hobbs et al., 1994) . The topological freedom, *f*, has been shown to relate to the amorphization dose, *D*, as (Hobbs et al., 1999)

$$f = 3 - 2.51D^{0.187}.$$

3-15

Many high temperature piezoelectric materials crystalize in the Perovskite structure for which, *f=-1* and the dose is thus 12 eV/atom. The Wurtzite structure yields *f=-3* and hence the amorphization dose is 106 eV/atom. To put this into perspective one should return the chapter 3.5.3 where it was mentioned that the dpa will be just shy of 1 dpa at our target fluence which corresponds to a displacing dose of just under 62.5 eV/atom assuming a displacement threshold of 25 eV.

3.7 Conclusion

For a material to be considered radiation hard a stable depolarizing defect generation rate that is orders of magnitude lower than previously study piezoelectric materials is needed. The most readily quantified measure of radiation effects is a calculation of the fraction of depoled volume as caused by thermal spikes. This treatment was developed by the author by way of adopting the Spike models discussed in (Szenes, 2005), (Szenes,

2011). This damage mechanism results in the right order of magnitude for the depoling of PZT and accounts for the doubling of the rate of polarization decrease when PZT is irradiated at a 130^{o} C as opposed to 30^{o} C. Additionally the model agrees with the findings of the Aerojet report (Anon, 1971) in which it was found that the radiation tolerance scaled with Curie temperature. This model assumes complete depoling in the volume which exceeds the Curie temperature, and this is one possible source of error. The volume that exceeds the Curie temperature is likely prevented from complete depolarization by pinning from the surrounding volume.

Provided depoling due the thermal spikes does not occur the next criteria would appear to be the materials resistances to amorphization in displacement spike processes. There have been many models put forth to predict the resistance of ceramic materials to amorphization as discussed in chapter 3.6.2. Currently it is known the Wurtzite structure is substantially more resistant to amorphization than the perovskite, with Wurtzite being able to withstand 106 eV/atom and Perovskite 12 eV/atom. It is clear, as demonstrated in chapter 3.5.3 that 62.5 eV/atom will be approached at the target fluence of 10^{21} n/cm^{2}. This would imply the amorphization of the Perovskite if it were not for the elevated irradiation temperature. At 500^{o} C the amorphization dose increases according to equation 4-1.

One must also consider the transmutation reactions, such as those occurring with ^{6}Li and ^{10}B, which have outstandingly large cross sections and result in the generation of energetic nuclei of the sort that produce either large thermal spikes or displacement cascades. Likely the most significant impact these reactions have is the elimination of

native species and the introduction of foreign species at concentrations of several atomic percent at the target fluence of 10^{21} n/cm^2. The transmutation reaction occurring with ^{14}N generates displacement cascades, however the cross section is only 1.8 barn and thus the effects are minimal at the target fluence.

4 Selecting a Radiation Tolerant Piezoelectric Material

The first criterion to be considered is the materials Curie temperature. Obviously it must exceed the ambient temperature during irradiation. This step has already been taken by only investigating high Curie temperature materials. Less obviously, the material must not fall victim to depoling by way of thermal spikes as described in chapter 3.6.1.

Provided thermal spikes are not causing depoling the next most likely cause of decreased polarization will be displacement spike processes described in chapter 3.6.2. In this case one is primarily concerned with the resistance to amorphization and Wurtzite materials show an excellent resistance being able to absorb 106 eV/atom (Hobbs et al., 1999) which is a factor of 10 higher than the perovskite materials. Further, AlN in particular has proven to be impossible to render amorphous by experimental means (Zingle, Snead, Eartherly, Jones, & Hensley, 1991), (Kucheyev et al., 2002). In the example calculations of chapter 3.5.3 it was shown that the target fluence of 10^{21} n/cm^2 will generate nearly 1 dpa in all potential piezoelectric materials and so a Wurtzite structure is required in the absence of significant annealing. It is clear that annealing will occur as indicated by equation 4-1, however one would prefer not to rely on this alone.

One must also consider the transmutation reactions, such as those occurring with ^{6}Li and ^{10}B, which have outstandingly large cross sections. Therefore one may rule out the rare earth oxyborates and lithium niobate. Isotope tailoring these materials may be an option worth considering.

With that said, the results of past research pertaining to the radiation effect on piezoelectric materials appear somewhat disheartening as all materials appear to lose at least 50% of the single pass efficiency before 10^{21} n/cm^2. Even strontium tatalate with a Curie temperature of 1342^{o}C and lack of transmuting species. However, all these works pertain to irradiation at low temperatures where damage recover is much less efficient. In fact at higher temperatures, materials which are readily amorphized at lower temperatures become nearly impossible to render amorphous at higher temperatures. A very simply model for the amorphization dose in dpa is given by the following equation (Meldrum et al., 2002)

$$D = \frac{D_o}{1 - Ae^{-\frac{E_A}{KT}}}$$

4-1

where A is a constant and E_A may be thought of as and activation energy.

In general the constants of equation 4-1 are experimentally determined and at high temperatures it is impractical to render materials amorphous. As a result a critical temperature is assigned to materials at which point the amorphous volume generation rate becomes less than the recrystallization rate and Table 1-3 provides this temperature for several piezoelectric materials.

The elevated temperature anticipated should therefore greatly increase the chance of successfully developing an ultrasonic sensor that is radiation hard up to 10^{21} n/cm^2 provided thermal spikes are not problematic. It must be noted however that in a few unfortunate materials the increased mobility of defects induces aggregation and renders the material less radiation tolerant.

In summary the material we select will:

- Not depole due to thermal spikes due to an exceptionally high transition temperature
- Be subjected to additional damage and stoichiometric alteration due to large transmutation species
- Not be rendered amorphous by displacement spikes due to the choice of a Wurtzite structure with low topological freedom
- Have a potentially dramatic increase in radiation tolerance when compared to previous literature due to the elevated irradiation temperature

There are only two materials which meet the first three criteria, AlN and ZnO. The resistance to thermal spikes is due to both a transition temperature in excess of 2000^o C and semiconducting characteristics. The resistance to amorphization is due to the crystal structure as calculated form the topological freedom. The following two sections provide a bit more background on the two materials.

4.1 Aluminum Nitride (AlN)

Aluminum nitride is a relatively new material, as far as bulk single crystals are concerned. In fact the work presented here and by the author elsewhere on bulk single crystal AlN is the first of its sort (Parks & Tittmann 2011). In the past thin film AlN has been shown to be unaffected by gamma irradiation up to 18.7 MGy (Kazys, 2005) and temperatures of 1000^{o} C (Patel, 1990), (Stubbs,1996). Moreover, this material has been explicitly cited in numerous independent studies as a highly radiation tolerant ceramic (Trachenko, 2004), (Zingle, Snead, Eartherly, Jones, & Hensley, 1991), (Kucheyev et al., 2002). Aluminum nitride was first brought to the author's attention by Ray Blasi of Bechtel-Bettis.

The only potential thorn in the side is the $^{14}N(n,p)^{14}C$ reaction, but a quick examination puts this concern to rest. The transmutation reaction of $^{14}N(n,p)^{14}C$ occurs by way of the low energy absorption of neutrons, the cross section is provided in Figure 4-1. As discussed in chapter 3.2.5 the effects of this reaction are minimal

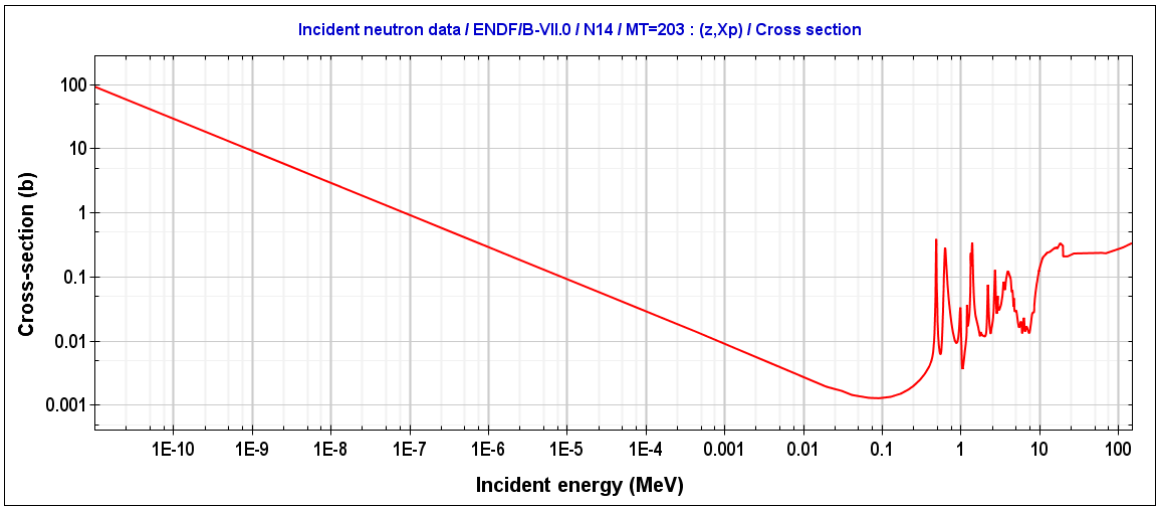

Figure 4-1: The cross section for the production of a proton and Carbon from thermal neutrons and Nitrogen 14

In summary the dpa due to fast and thermal neutrons and the atomic percentage of foreign atoms, or "radiation doping", is presented in Table 4-1, the flux is assumed to be 10^{21} fast and 10^{21} thermal neutrons. Note that this amount of carbon was found in pristine samples and the additionally 0.13 dpa should be of little concern.

dpa fast	dpa thermal	doping at %
0.81	0.13	0.18

Table 4-1: damage summary for AlN exposed to 10^{21} fast and thermal neutrons

4.2 Zinc Oxide (ZnO)

The story for ZnO is similar to AlN however this material has a higher coupling coefficient and does not have any transmutation vulnerable atomic species. Obtaining bulk ZnO appears to be more difficult than bulk AlN. However, ZnO films are in fact used in ultrasonic microscope lenses.

5 Transducer Radiation Hardness Test

The procedure and results of an experiment that involved operating a transducer composed of monolithic bulk single crystal AlN in pulse echo mode in a reactor core are now described. During irradiation four primary effects are anticipated;

- reduction in piezoelectric effect due to the tending towards an isotropic state of the piezoelectric material
- increased dielectric loss due to defect generation (Frenkel pairs, etc.) and ionization
- mechanical failure of transducer test fixture

The pulse echo data, impedance data, and data from prior high temperature experiments will be utilized to interpret the overall performance of the transducer and to identify which of the three anticipated effects is likely dominant. The possibility, of depoling or not applicable for non-ferroelectric AlN, and the amorphous transition should require a very high fluence and this transition has not been achieved despite attempts by other researchers.

5.1 Experimental Methodology

A single crystal AlN element (4.8 mm in diameter and 0.45 mm thick) resonant at 13.4 MHz, was coupled to an aluminum cylinder via mechanical pressure. Aluminum foil was used as a gasket between the aluminum cylinder and the AlN element, allowing for strong, clear A-scan data to be obtained. The AlN element was loaded, on the side

opposite the aluminum cylinder, with a sintered carbon/carbon composite to reduce ringing and improve the signal clarity. The test fixture is illustrated in Figure 5-1.

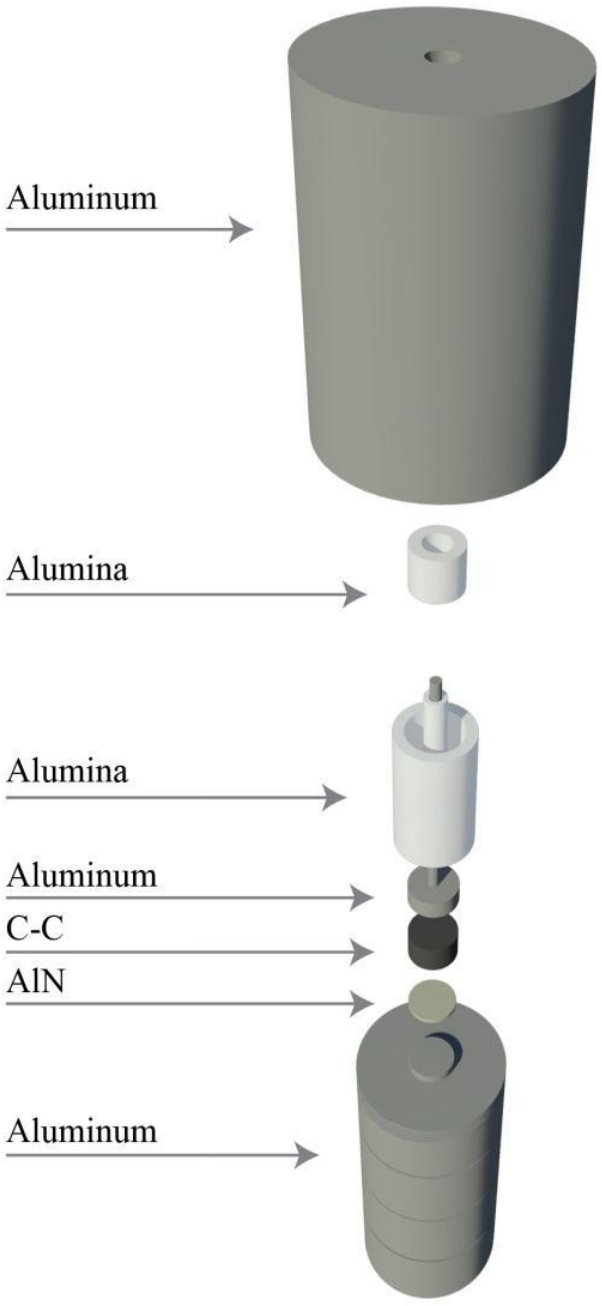

Figure 5-1: Experimental setup for preliminary irradiation of piezoelectric AlN.

The aluminum cylinder acted as the lower electrical contact and the plunger provided the upper electrical contact. The setup was connected to a radiation hard 50 ohm coaxial cable. This radiation hard cable consisted of an aluminum conduit sleeve over fused quartz dielectric tubing with an aluminum inner conductor. The cylinder/piezo setup was placed in the core of the Penn State TRIGA reactor and irradiated to a fast and thermal neutron fluence of 1.85X1018 n/cm2 and 5.8X1018 n/cm2 respectively and a gamma dose of 26.8 MGy. Throughout the irradiation the A-scan data was recorded with impedance measurements interspersed.

5.2 Experimental Results

5.2.1 High Temperature Experiments and the Lesson Learned

In past works, varied crystalline quality resulted in numerous samples which were capable of operation up to 1000^{o} C (Parks, Tittmann, & Kropf, 2009), (Patel & Nicholson, 1990), (Stubbs & Dutton , 1996) and in some cases dramatic increases in the loss tangent at elevated temperature with an associated loss of transduction. This dielectric loss effect is shown in Figure 5-2.

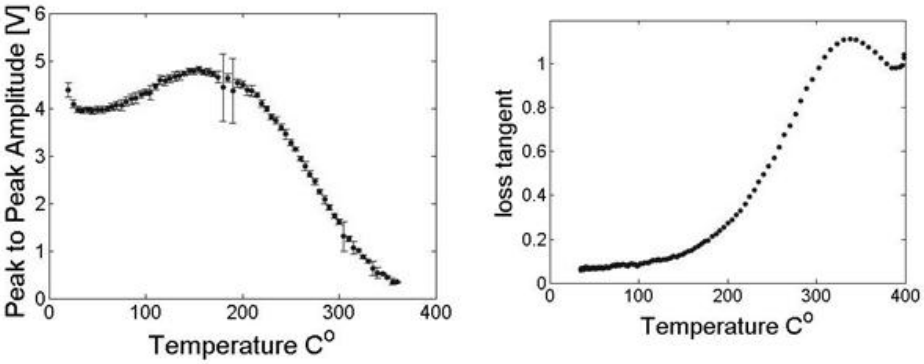

Figure 5-2: Data from high temperature experiment on low quality AlN: Peak to peak amplitude of the A-scan signal and the loss tangent

This can be explained by hypothesizing that the electrical energy is lost to conduction through the crystal and as a result little to no mechanical energy is generated. The sample utilized during irradiation was tested to high temperatures and found not to exhibit signal loss or an increase in tanδ. Dielectric loss may also be of concern in the presence of ionizing radiation (C. Claeys, 2002), (Glower, Hester, & Warnke, 1965).

5.2.2 Long Term Irradiation Effects

Pulse Echo Response

The A-scan data, illustrated in Figure 5-3, was recorded and analyzed in terms of the echo amplitude, which is presented in Figure 5-4.

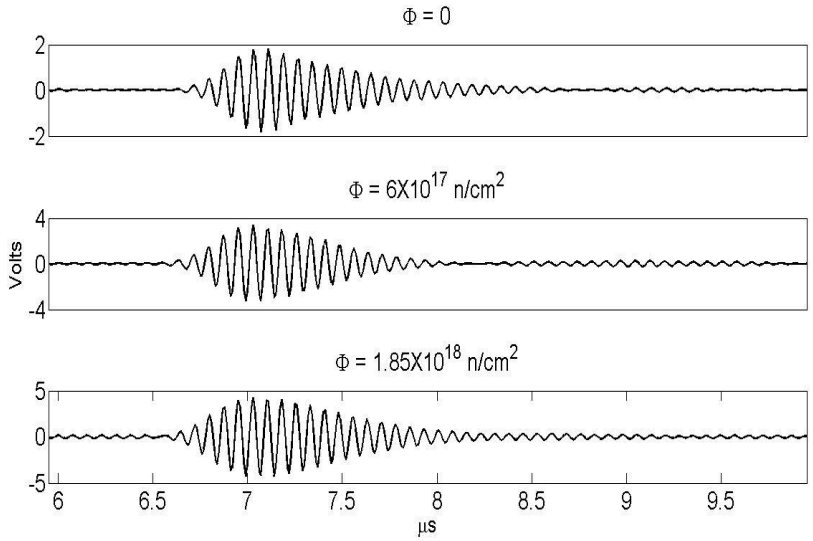

Figure 5-3: A-scans obtained from AlN in the TRIGA reactor core, Φ is the fast neutron fluence

The data shown in Figure 5-3 and Figure 5-4 correspond to times when the temperature was below 40^{o} C to eliminate the confounding effect of thermal expansion in the test fixture. The amplitude over the course of irradiation remains nearly constant and indicates the radiation hardness of the AlN and the test fixture.

The first data point was increased by a factor of 1.82 due a change of cable that was necessitated by a faulty terminal after the first day in the core. The factor of 1.82 was obtained by observing the amplitude of the setup with the defective cable compared to its replacement. It would have been reasonable to proceed with the defective cable and the slightly lower amplitude if it were not for the intermittent nature of the signal that would vanish entirely if the cable was contorted. The increase in the first data point, if unfounded, would imply that the performance improved with irradiation.

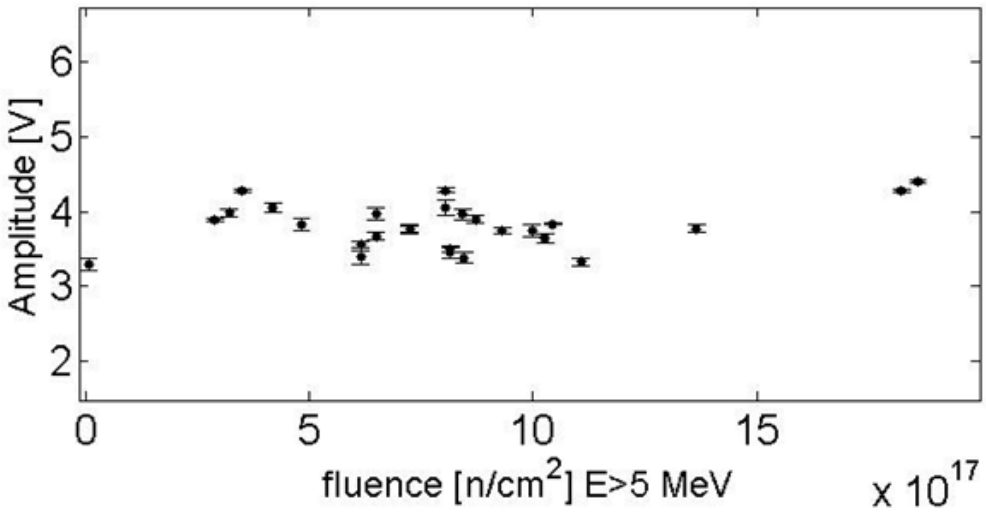

Figure 5-4: Amplitude of the A-scan signal throughout irradiation

Close inspection of Figure 5-3 reveals some change in the ringing of the transducer. The ringing, which can be represented well by the Q value, in fact increased linearly with fluence as can be seen in Figure 5-5. The Q value was measured by way of the frequency spectrum of the pulse response, e.g. the fft of the pulses shown in Figure 5-3.; note the pre-irradiation point affected by the cable terminal mentioned above.

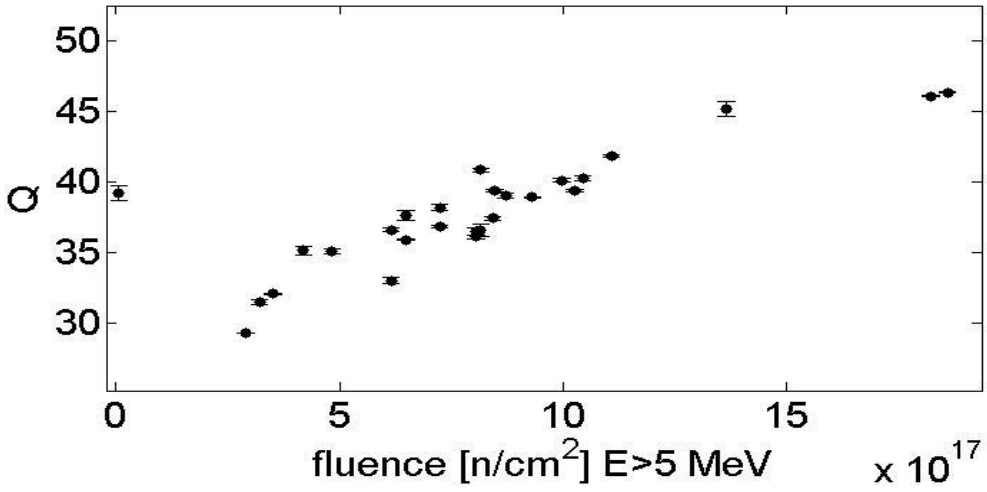

Figure 5-5: Q value throughout irradiation

To be sure that the increase in the Q value was not due to a reduction in the attenuation within the Al acoustic propagation path the main bang ringing was analyzed and found to increase linearly with fluence.

In the case of single crystal piezoelectric materials such as AlN a high intrinsic Q value, of several thousand, is to be expected. As a result the Q value measured primarily depends on the transfer of mechanical energy to the aluminum cylinder and the backing. Therefore, a degradation of mechanical contact is likely the cause of the increased Q

value. The contact degradation is attributable to a reduction in the contact pressure at the AlN to Al, and AlN to backing surfaces, or possibly an increase in the porosity of the carbon backing. The literature seems to indicate that the dimensional changes in the Al test fixture should be on the order of 0.07 ppm at the maximum obtained fluence, therefore it is not believed this effect contributed significantly to the increase in Q. The negligible dimensional changes are confirmed by the time of flight as measured prior to and after the total fluence, which showed no statistically meaningful change. However, the temperature of the test fixture was brought from room temperature to 120^{o} C more than 200 times over the course of irradiation with a typical rate of 7 degrees per minute. This is likely to have caused degradation of the mechanical contact by means of thread deformation and or a loosening of the cylinder cap.

Electrical Impedance

The change in impedance as measured was inevitably affected by the more than 50 feet of cabling needed to place the transducer in the reactor core. Low loss RG 213 U cable was used to combat this effect and to avoid energy loss during pulse echo operation. Nonetheless, the real and imaginary portions of the impedance at 50 kHz displayed a monotonic evolution during irradiation as shown in Figure 5-6.

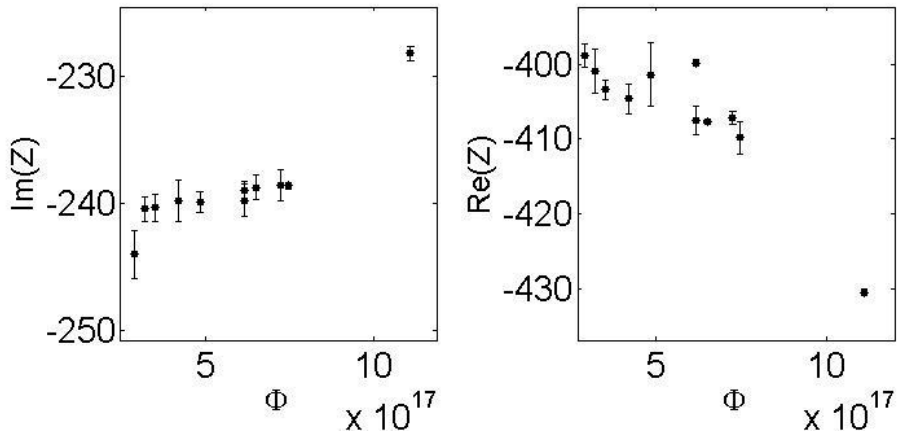

Figure 5-6: Changes in 50 kHz reactance and resistance throughout irradiation Φ is the fast neutron fluence

The changes in impedance may be attributed either to the AlN or any portion of the test fixture and cabling. However, the low frequency capacitance has been utilized as a means of sensor self-diagnostics (Zheng, Martinez, Easton, Park, & Farinholt, 2011) and the trend displayed in the imaginary portion of the impedance is consistent with degradation in the contact conditions. Specifically in (Zheng, Martinez, Easton, Park, & Farinholt, 2011) it was shown that the bonded and un-bonded capacitance at low frequency for a PZT disk excited in the thickness mode are related as

$$C_{bonded} = C_{un-bonded}[1 - (d_{31})^2 Y^E_{piezo}] \quad 5\text{-}1$$

where Y^E_{piezo} is the Young's modulus of the piezoelectric material and d_{31} is the lateral piezoelectric constant. Fortunately, z-cut single crystal AlN has the same symmetry as PZT and this equation is applicable. Unfortunately, for the observed decrease in capacitance to occur one must have either degradation in the contact condition or a

decrease in the transverse piezoelectric constant. Therefore one cannot conclude the piezoelectric effect has not diminished.

Alternatively, if one considers the KLM model at mechanical resonance then the impedance is given by

$$Z_{\omega o} = \frac{1}{j\omega C_0} + \frac{4h^2}{\omega_o^2}\left(\frac{1}{Z_{load} + Z_{backing}}\right) \qquad 5\text{-}2$$

which shows that the real portion increases if the contact conditions degrade or if the piezoelectric constant *h* increases. Figure 5-7 shows the real portion of the impedance at mechanical resonance with fluence on the abscissa and confirms that the contact conditions are degrading with fluence.

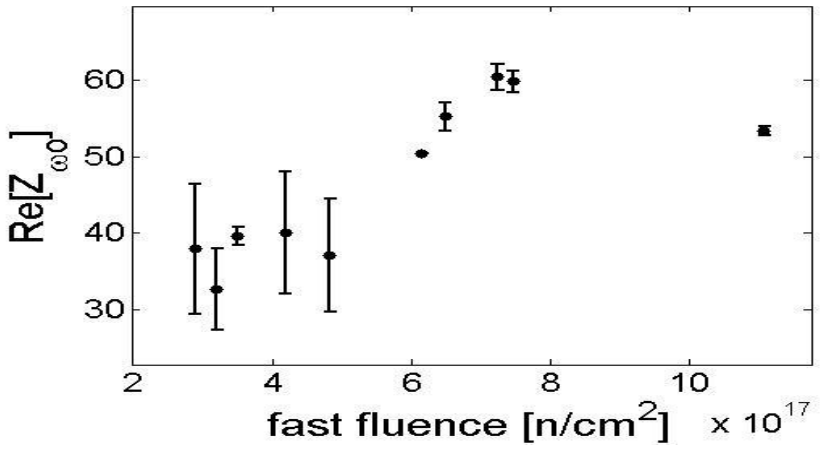

Figure 5-7: Real impedance at mechanical resonance.

5.2.3 Transient Radiation Effects

In addition to the long term effects a consistent repeatable A-scan amplitude decrease during, and rapid recovery prior to, irradiation was observed as is demonstrated in Figure 5-8.

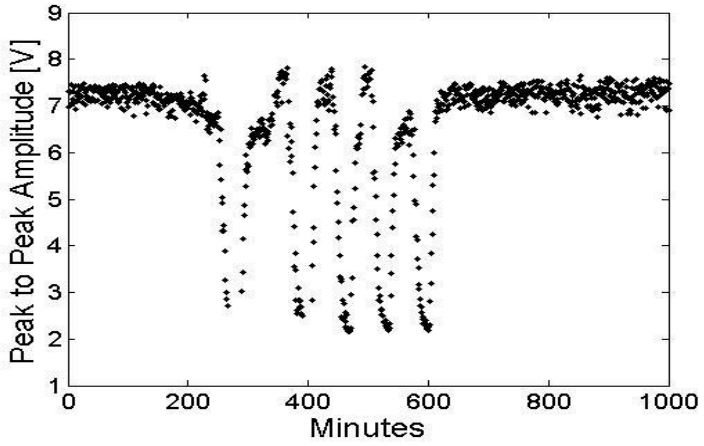

Figure 5-8: Pulse echo amplitude during irradiation five distinct troughs correspond to five 29.5 minute irradiations.

The impedance data was utilized to interpret transient effects, namely the reduction of pulse echo amplitude during irradiation followed by the rapid complete recovery. The recovery typically took 20-30 minutes and was not accompanied by a dramatic increase in the measured loss tangent as is shown in Figure 5-9.

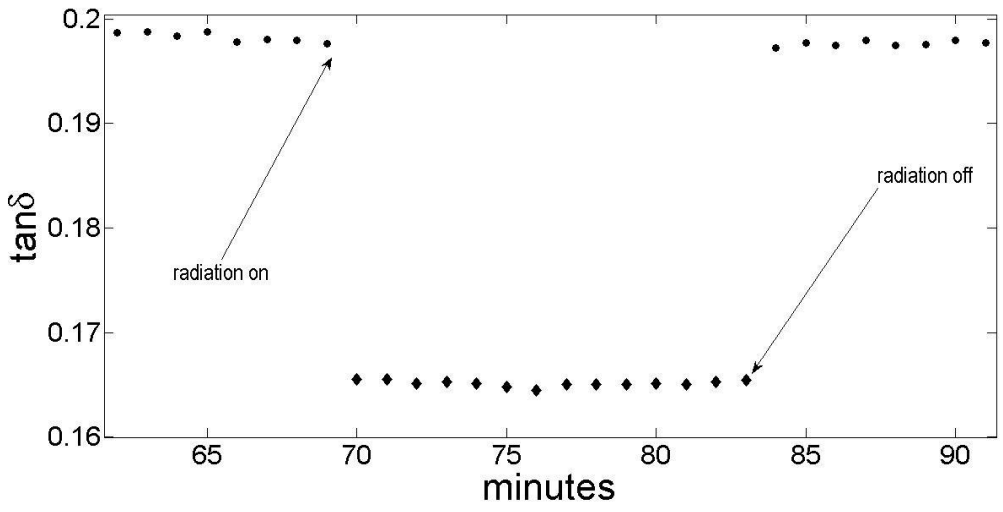

Figure 5-9: Transient effects on the loss tangent, arrows indicate times when the reactor is turned on and off (the left arrow corresponds to the reactor being turned on and on the right it is turned off)

The loss tangent data are inconsistent with an increase in dielectric loss in the AlN additionally; a short or open circuit would be reflected as a dramatic change in loss tangent data. As far as amorphization is concerned the time scale is not commensurate with such an effect. Therefore, it is hypothesized that a transient reduction in contact pressure due to thermal expansion is the cause. This is not particularly surprising given a spring had not been incorporated to compensate for thermal expansion mismatches and the temperature increase from room temperature to roughly 120^{o} C during irradiation. Considering the thermal expansion coefficient and dimensions of the materials utilized in the test fixture result in a calculated a lift-off displacement on the order of 10 μm. This lift-off due to dissimilar thermal expansions coefficients is partially compensated by the relatively soft carbon backing. The backing was deformed when the initial contact

pressure was applied and hence played the role of a spring, albeit with very minimal travel.

5.2.4 Transducer Application

Temperature Measurement

The temperature of an aluminum cylinder was measured with the AlN transducer by means of time of flight (TOF). The TOF was measured by detecting the threshold crossings of two successive echoes. The threshold crossing was applied to the magnitude of the Hilbert transform as shown in Figure 5-10. The threshold crossing method was found to be most precise in this case due to the small protrusion on the Al cylinder which was utilized to keep the crystal from sliding on the surface, see Figure 5-1. This small protrusion caused two reflections in the second transit as can be seen in Figure 5-10.

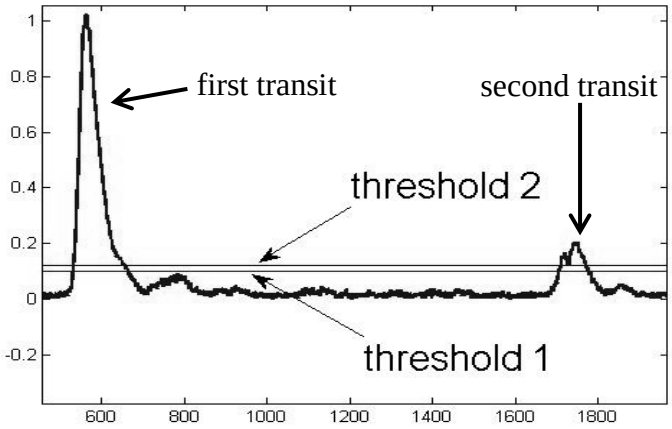

Figure 5-10: Threshold crossing method, note the abscissa represents samples in time and the vertical is the pulse amplitude.

In order to use the TOF data to obtain temperature a control experiment was conducted on a similar Al cylinder heated within a tube furnace. The resulting relative change TOF was found to be linear with temperature as shown in Figure 5-11. The relative percentage change in TOF, $100*\Delta t/t_o$, was utilized to make the technique independent of the room temperature acoustic path length.

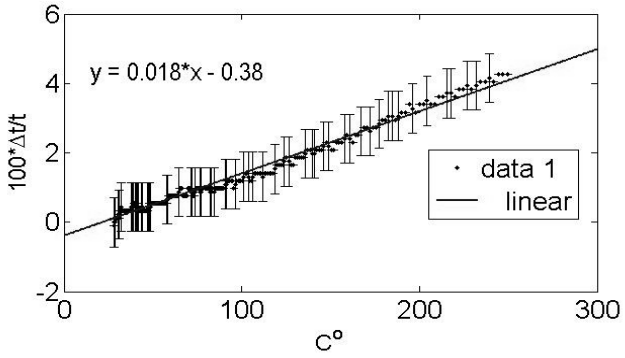

Figure 5-11: baseline TOF versus temperature curve for Al 6061

The Hilbert transform was utilized to prevent slight rise time changes from causing shifts in the TOF due a jump in threshold crossing to the next period in the pulse.

As an alternative method and a consistency check the waveforms may be deconvolved to produce sharp spikes corresponding the arrival times. Due to the significant noise a Wiener filter, as discussed in (Schmerr & Song, 2007) must be used during the deconvolution. The Wiener filter output *O(f)* when applied to discrete time varying signal *i(t)* transformed to the frequency domain to yield *I*(*f)* is

$$O(f) = \frac{I(f)M^*(f)}{|M^*(f)^2| + \varepsilon \max(|M^*(f)^2|)}$$

where $M^*(f)$ is the complex conjugate of the matched filter, e.g. a zero padded window of the first pulse in this case, shown in Figure 5-3.

In addition the first peak in the second transit must be selected to obtain the time of flight. Calculated form each method is displayed in the two methods disagrees by less than 18^o in the worst case.

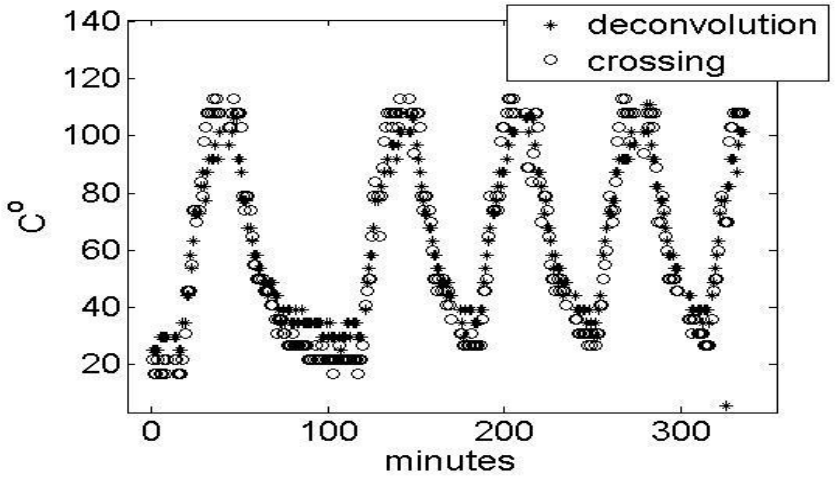

Figure 5-12: Temperature variation of Al cylinder during a typical day in the reactor core with five 29.5 minute irradiations

In Figure 5-12 the reactor is turned on and off 5 times, which is apparent in the temperature fluctuations. Additionally, the lack of coolant on the Al cylinder and short lived isotopes caused an upward drift in temperature throughout the day. The effect of short lived isotopes is more apparent on a day when the reactor was operated continuously for 300 minutes as is shown in Figure 5-13.

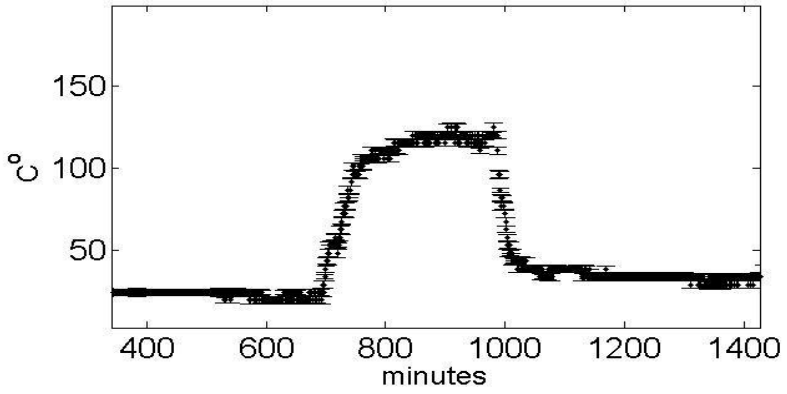

Figure 5-13: Temperature of Al cylinder during a 300 minute irradiation

The development of isotopes is apparent in the continued heating caused by their decay after the reactor is turned off.

The temperature in the cylinder is readily calculated if one assumes that the heat is lost to the surrounding air in the dry tube by way of convection and that the majority of the convection occurs radially as opposed to form the end of the aluminum cylinder. The temperature is given by (Kok, 2009)

$$T = T_o + q\rho\left[\frac{R}{2h} + (R^2 - r^2)\frac{1}{4k}\right]$$

5-4

where R is the radius of the cylinder, k is the thermal conductivity, ρ the density of the cylinder, h the convective heat transfer coefficient and q the energy per gram being deposited as heat. In the TRIGA reactor at 900 kW q is roughly 69 W/g and scales with reactor operating power. As a result one would expect a temperature of 84^o C. The additional heating may be attributed to the development of several isotopes which are

listed below as calculated by way of the activity predictor provided by Dağıstan Şahin. This activity predictor software is described in (Şahin & Kenan , 2009).

Compound Name : Al6061
Compound Weight (g) : 340.0
Irradiation Time (min) : 20.0

Isotope	Target Mass (g)	Isotope Activity(mCi)	Gamma Exposure Rate(mrem/hr)
Al-28	3.26E2	6.41E5	1.86E11
Mg-27	3.26E2	2.30E3	5.77E8
Na-24	3.26E2	8.04E0	2.27E6
Al-29	1.27E-1	7.00E-1	1.41E5
Si-31	8.43E-2	6.52E0	1.22E6
Mn-54	1.38E-1	3.68E-4	1.72E0
Cr-51	1.38E-1	1.22E0	7.55E2
Mn-56	2.18E0	8.37E2	6.16E6
Fe-59	6.66E-3	8.05E-3	4.36E1
Cu-64	4.70E-1	1.37E2	1.67E5
Co-60	4.70E-1	1.11E-6	1.25E-2
Cu-66	2.10E-1	1.83E3	8.01E5
Ni-65	2.10E-1	8.12E-3	1.97E1
V-52	1.70E-1	1.21E0	7.63E3
Zn-65	4.13E-1	4.52E-2	2.14E2
Zn-69m	1.60E-1	7.52E-1	1.65E3
Cu-67	3.40E-2	1.13E-4	9.55E-2
Zn-71m	5.10E-3	1.12E-2	8.46E1
Sc-46	4.08E-2	7.16E-5	6.76E-1
Sc-47	3.72E-2	2.61E-3	1.22E0
Sc-48	3.76E-1	7.64E-4	1.18E1
Ti-51	2.75E-2	2.10E1	3.78E4
Sb-122	9.74E-2	1.11E1	2.36E4
Sb-122m	9.74E-2	2.58E1	1.41E4
Sb-124	7.26E-2	2.20E-1	1.78E3
Sb-124m	7.26E-2	1.12E1	2.45E4
TOTAL	6.46E5	1.87E11	

Table 5-1: Isotopes developed in the Al 6061 cylinder after 20 minutes of irradiation at 900 kW

A calculation of additional heating due to isotope development would be nice however this is a bit complicated and perhaps best left to the expert in nuclear physics. Alternatively one may look at a simplified scenario wherein the irradiation has not continued long enough to develop a substantial activity due to ^{28}Al and the convection

has not become significant, that is the adiabatic condition which one can expect to be most accurate before the cylinder temperature climbs much beyond that of the surrounding air and the irradiation has not proceeded long enough to generate significant activity. In this case the rate of change in the temperature is given by

$$\frac{\partial T}{\partial t} = \frac{q}{C_p}$$

5-5

where C_p is the specific heat capacity 0.9 J g^{-1} K^{-1} and therefore one would expect a rate of change of 4.14^o C/min. The cooling cycle on the other hand may be expected to follow Newton's law of cooling

$$T = T_{ambient} + T_0 e^{-rt}$$

5-6

where $r = hA/C_p$. This theoretical approximation is superimposed on the temperature data from the first irradiation cycle of Figure 5-12 in the Figure 5-14 below.

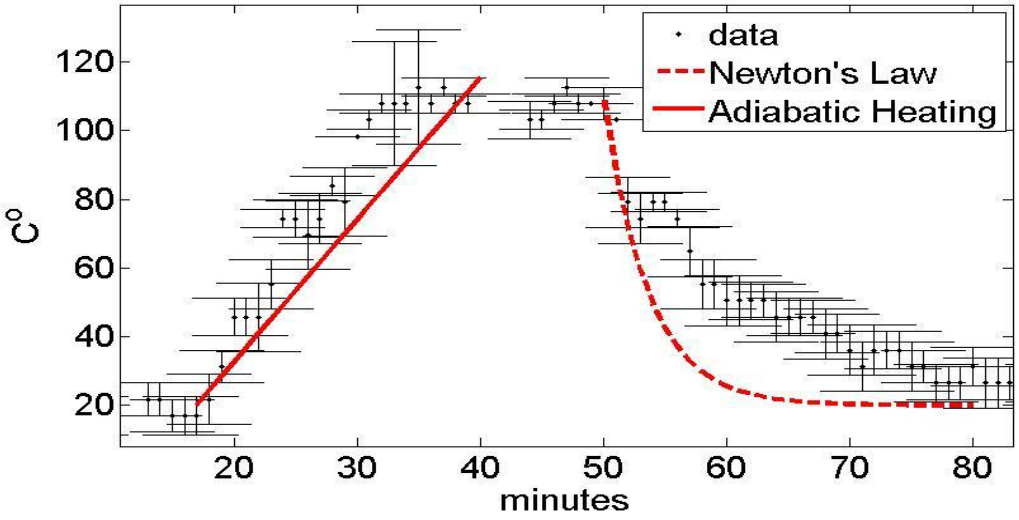

Figure 5-14: Temperature data compared to adiabatic heating approximation and Newton's law of cooling.

One can see that the theoretical curves are not dramatically incorrect and are in fact within the error up to roughly 80^{o} during the heating. The difference between the theory and the curves is due to the invalidity of the adiabatic condition and the generation of radioactive isotopes which contribute to the generation of thermal energy.

Time of Flight versus Exposure

The time of flight measurements have potential for monitoring the porosity of a material as it is subjected to damaging radiation. Again one has the issue with two echoes in the second transit. As a result the threshold method was used on the Hilbert transform and the RF waveforms. Additionally the peak in the analytical envelope was utilized and in this way three measurements were obtained for a statistical basis. The time of flight was measured when the reactor was off and the Al was at room temperature. As is to be expected there is little change in the time of flight over the exposure time, which is shown in .

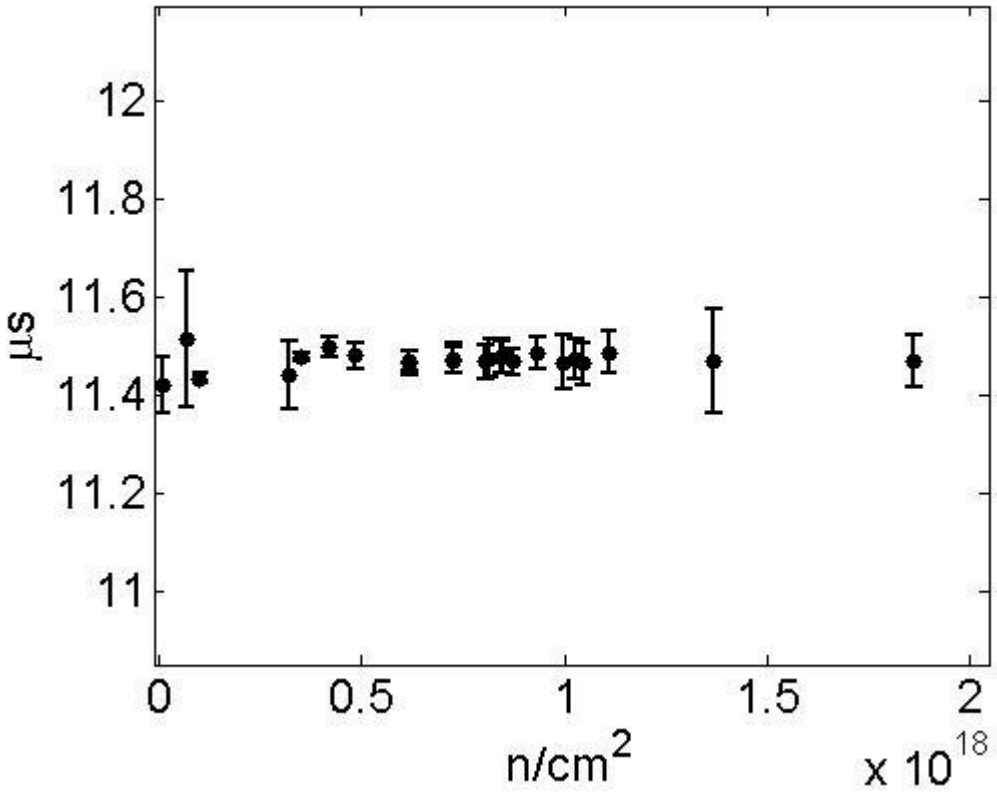

Figure 5-15: Time of flight in the Al cylinder throughout the irradiation period of more than 3 months

5.2.5 Post Irradiation Testing

Prior high temperature experiments with AlN have led us to believe that crystalline defects can degrade the high temperature transduction of AlN. Considering that radiation causes displacement damage and transmutation doping, one may wonder how the irradiated AlN would fare at high temperatures. To answer this, the irradiated crystal having negligible activity after cooling for a few weeks, was tested up to 500^{o} C, the resulting waveforms are provided in Figure 5-16. Additionally d_{33} was measured after irradiation and found to be 5.5 pC/N.

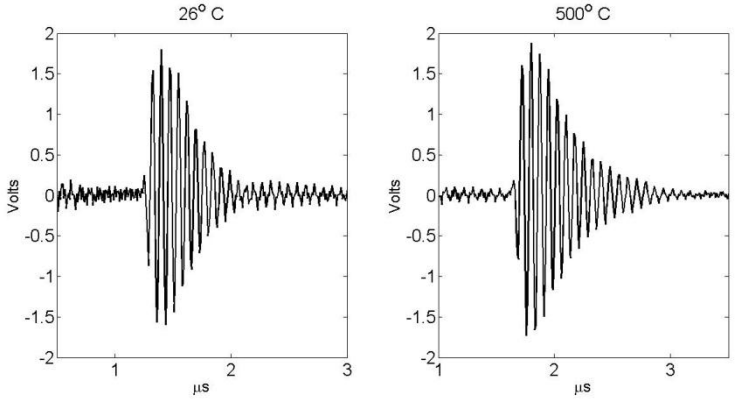

Figure 5-16: Waveforms form post irradiation testing of AlN

5.3 Conclusion

AlN appears to be a radiation hard piezoelectric material. The hardness is most evident from the unaltered piezoelectric coefficient d_{33}, which measure 5.5 pC/N after a fast and thermal neutron fluence of $1.85X10^{18}$ n/cm^2 and $5.8X10^{18}$ n/cm^2 respectively and a gamma dose of 26.8 MGy.

A transducer, composed of monolithic bulk single crystal z-cut AlN, has been shown to operate in a reactor core with no degradation in signal amplitude up to the fluence and dose stated above. Under the experimental conditions the Q value increased, which is attributable to degradation of the test fixture.

Transient reductions in signal amplitude and increases in the Q value were observed. These effects where reversible in all cases in a matter of 30 minutes. The transient effect is attributed to thermal expansion of the test fixture reducing the contact pressure between the AlN and the acoustic propagation medium and backing.

6 Ultrasonic Arrays

6.1 Introduction

An ultrasonic array is simply a collection of individual ultrasonic transducers, and hence, modeling typically involves a calculation of the superposition of multiple transducers often each with a given phase shift. The phase shift is more precisely a time delay in conventional ultrasonic methods, as broad band or at least temporally finite ultrasonic pulses are utilized. An illustration of important geometric al parameters of a phased array is proved in Figure 6-1.

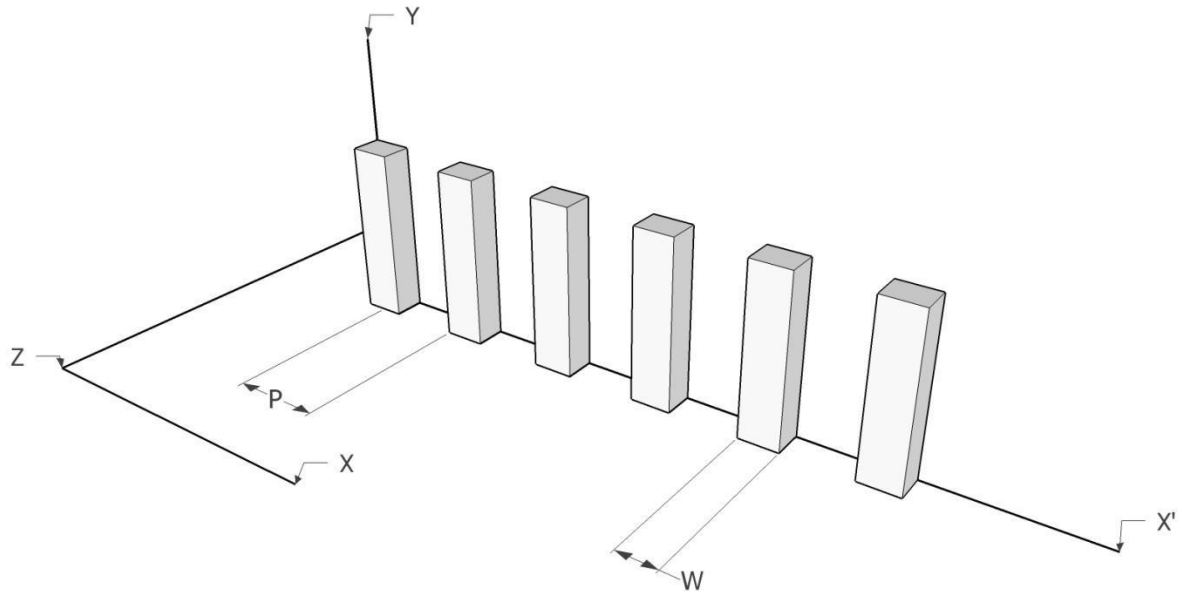

Figure 6-1: An array of six elements of width W and pitch P.

6.2 Phased Arrays

Phased arrays come in many forms, and are utilized in many contexts to focus radiation in the general sense. The earliest documented physical realization of phased arrays appears to be the have emerged form works of Karl Ferdinand Braun in 1902 (Braun, 1909). Braun demonstrated an increase in electromagnetic transmitter directivity by applying phase delays to a three element array. From 1909 on development was spurred on by World War I and World War II where arrays where sought for both sonar and radar. Additionally, arrays have found a niche in astronomy as well as ultrasonics and microwave imaging.

In this context one of course is interested in the ultrasonic array; however, one may borrow, as many have, concepts from any one of the many array niches. However, when borrowing concepts from the vast collection of array niches, care must be taken to assure effective translation to ultrasonic NDE applications. In particular; mode conversion, nearfield, element directivity, and broadband pulses must be considered.

The most basic array assumes a collection of isotropic continuous wave apertures radiating each with an assigned phase shift. The beam pattern of such an array is described by equation 6-1

$$u = \sum_{n=1}^{N} e^{ikdnu}$$

6-1

where θ is the angle from the arrays central axis, *N* represents the number of elements in the array, P is the pitch and $u = \sin(\theta) - \sin(\theta_{steereing})$. The steering angle is

introduced by a phase shift in the excitation between neighboring elements given by $kdsin(\theta_{steering})$ (Hansen, 1997). An example of the directivity pattern of equation 6-1 is provided in Figure 6-2. In ultrasonic imaging one can expect pulse echo operation in which case the overall or two way beam pattern is given by the convolution of the transmit and the receive beam patterns, hence the vertical scale in Figure 6-2 should be increased by a factor of two and the two way beam pattern is given by

$$u = \left[\sum_{n=1}^{N} e^{ikdnu}\right]^2$$

6-2

Equation 6-1 and 6-2 and the associated phase shift applied to the elements assume the Fraunhofer approximation and hence the phase delays only depend on the angular coordinate θ. However, if one assumes pulse operation and does not apply the Fraunhofer approximation the time delay between the pulsing of the elements is

$$\tau_n = \frac{\sqrt{\left(x_f - x_n\right)^2 + \left(y_f - y_n\right)^2 + z_f^2}}{c} - \tau_o$$

6-3

where the subscript *f* indicates coordinates of the focal point, subscript *n* indicates coordinates of the n_{th} element, *c* is the wave velocity and t_0 arranges for the first element to fire without delay. This time delay is also utilized to select the correct time to sample the returning signal during pulse echo imaging. This is sometimes referred to as dynamic depth focusing and requires that each pixel in an image be obtained by a pulse echo operation and as such may be relatively time intensive. As a result dynamic focusing is

frequently only be applied during receive, particularly if the imaging volume is moving as in medical ultrasonics (Szabo, 2004).

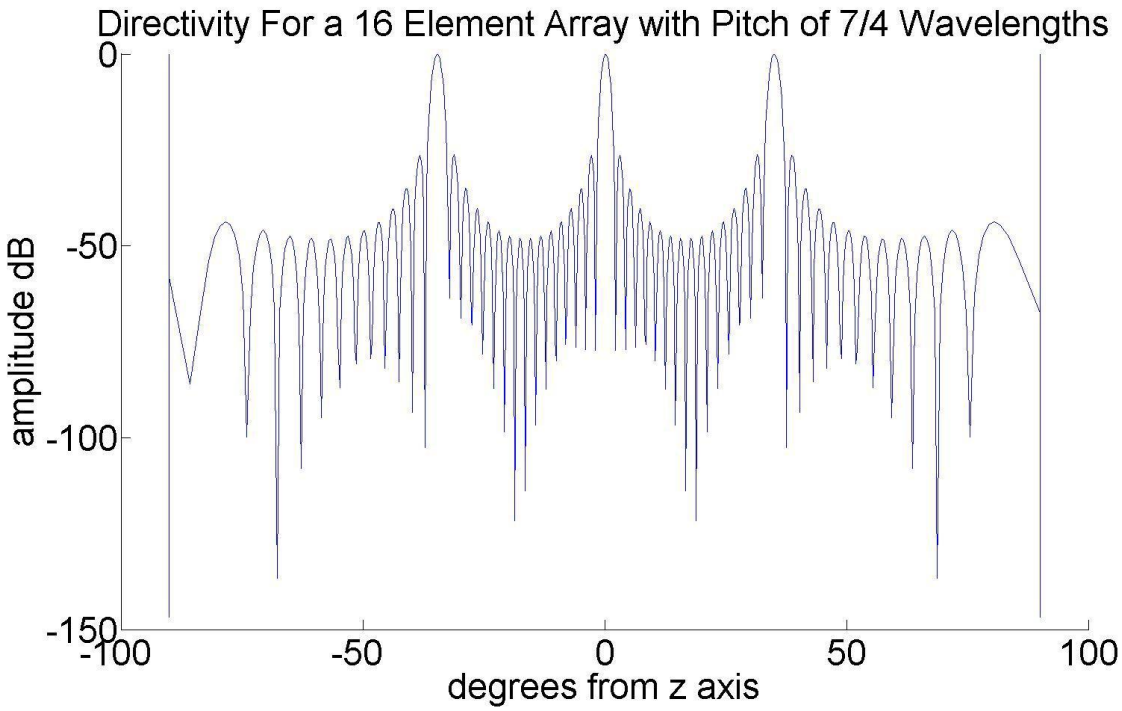

Figure 6-2: Directivity pattern for a 16 element array P=7/4λ assuming isotropic elements

All the above expressions apply to the plane bisecting the array depicted in Figure 6-1 vertically and assume that the directivity in the vertical direction may be dealt with separately as will be discussed later in this chapter. Such an array is referred to as a 1-D array.

Additionally all the above expressions assume the individual elements of the array behave as isotropic sources, i.e. the amplitude and phase are assumed to be constant for a given radial distance from the point source. This assumption becomes questionable when the array element's radiating surface dimensions become equal, or larger than, the

wavelength of the radiation. In the other extreme, the array element's radiating surface dimensions are many wavelengths in scale and the wave front produced radiates primarily normal to the radiation surface beam steering is not possible.

Additional consideration must be made to account for the matching layer and baffle of the element. Calculations of the beam pattern of an ultrasonic transducer commonly utilize the Rayleigh formula while assuming a rigid baffle. However, agreement between experimental results and calculations have not been found when assuming rigid or soft baffles which are idealizations of the true baffle conditions (Presque & Fink, 1984). The matching layer presents a surface at which reflection and refraction is bound to occur, thereby altering the beam pattern.

6.3 Phased Array Conventional Methodology

6.3.1 Pitch

Phased arrays typically utilize a pitch of roughly half a wavelength so as to avoid grating lobes. Unfortunately, in general the beam width and hence, the spatial resolution perpendicular to it, is inversely proportional to the length of a linear array as can be seen in equation 6-4 (Hansen, 1997)

$$\theta_{3dB} = \frac{0.8858}{NPcos(\theta_{steereing})}$$

6-4

where *N* represents the number of elements in the array and *P* the pitch. Therefore in this case it seems desirable to increase the pitch, thereby improving resolution. However, grating lobes make this option less viable. Specifically, once the pitch just exceeds a half

wavelength a grating lobe will develop at -90^o when the beam is steered to +90^o and in general the grating lobe location is given by,

$$\frac{P}{\lambda} = \frac{m}{\sin(\theta_{steering}) - \sin(\theta_{grating})}$$

6-5

which, when defined, gives a grating lobe location and otherwise indicates that the m_{th} grating lobe is not in visible space. A common method for maximizing the element pitch but yet keeping the grating lobe out of visible space is to place the directivity pattern null just inside the grating lobe at the edge of visible space. This is accomplished by (Hansen, 1997)

$$P = \lambda \frac{N-1}{N\left[1 + \sin(\theta_{\max\_steering})\right]}.$$

6-6

The maximum pitch therefore depends on the number of elements and the maximum steering angle as can be seen in Figure 6-3.

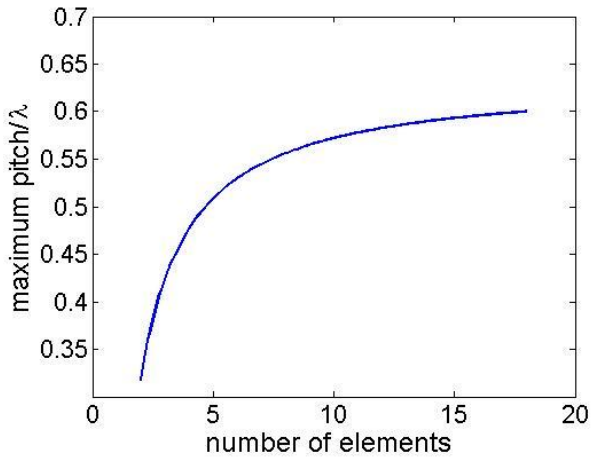

Figure 6-3: Maximum pitch allowed while keeping grating lobes out of visible space assuming 45^{o}steered beam.

As grating lobes appear they not only have the potential to introduce imaging artifacts but they also draw energy from the main beam which is detrimental. The gain of the array is the power transmitted in the intended direction divided by the total radiated power and can be written as

$$G = \frac{N^2}{N + 2\sum_{n=1}^{N-1}(N-n)sinc(nkP)\cos\left[nkPsin(nkPsin(\theta_{steering})\right]}$$

6-7

A plot of the gain versus element spacing is provided below showing the detrimental effect of grating lobes for a 16 element array.

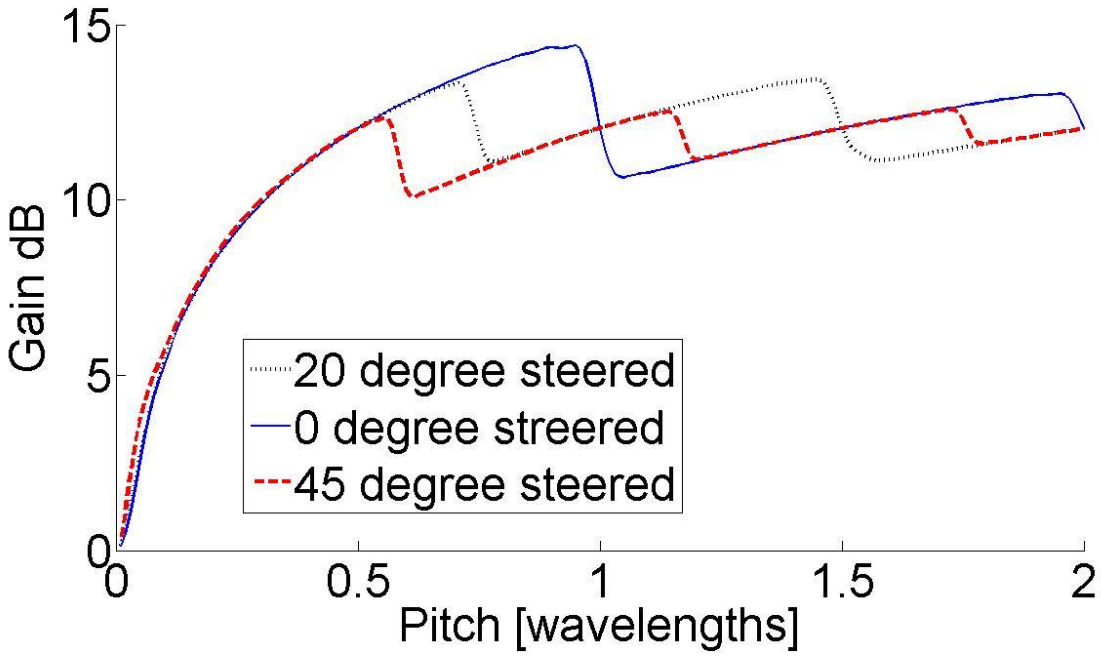

Figure 6-4: Gain of a 16 element array as a function of pitch for steering angles of 0, 20 and 45 degrees

From Figure 6-4 one can see that the gain is a maximum for a spacing of 0.55λ when the array is steered to 45 degrees as one would expect based on equation 6-6.

6.3.2 Element Width

Conventional phased arrays utilize elements which are less than a wavelength wide for two reasons; first of all it is impossible for the element width to exceed the pitch, secondly wide elements produced narrow beams and reduce the array sensitivity when steered away from the central axis.

Scaling the array beam pattern with the element beam pattern is often utilized to account for element directivity when modeling phased arrays. However, in the optimization procedure the angle from any given element to the field point may be

significantly different from the central axis angle since conventional pitch restriction is abandoned. For example, denote the array by first assuming a baseline pitch of one half wavelength, and the allow a 1 to represent an element where it would be found in a filled array, and a 0 to represent and empty slot Yang et al. have come up with the following 16 element array (Yang, Chen, & Shi, 2006)

1101011101111111100000000000010001.

For this array configuration, at an axial distance of 30 wavelengths and a steering angle of 40^o the angle from the element at the left is 48^o and hence the loss in sensitivity at the left element is more than 1 dB below what the convolution method predicts for a half wavelength wide element. With this in mind one should either, restrict the maximum array length during optimization procedures or utilize a directivity function for each array element. The later choice is more computationally demanding. Further, considering that any elements, which are located outside the would-be maximum array length will increase resolution only at the expensive of sensitivity it seems that the former choice is most prudent.

Additional consideration to the element width in terms of the width to thickness ratio, or aspect ratio, is required. The aspect ratio must be selected to avoid coupling between lateral and thickness modes. Coupling between these two modes will result in significant signal degradation. The signal degradation is the result of energy being allowed into lateral vibrations which do not contribute to the acoustic field in a constructive manner if at all. Additionally, this energy has the potential to remain in the

element for inordinately long times. In many ceramics and aspect ratio of less than or equal to 0.6 provides sufficient separation between the two modes (Ritter, 2000).

In this case elements which are at most roughly one wavelength, in water, wide are anticipated. The thickness of the element will be equal half the wavelength in the element so one has

$$t = \frac{c_{ceramic}}{2f}$$

$$W = \frac{c_{water}}{f}.$$

Therefore, an upper bound on the aspect ratio is

$$R = \frac{W}{t} = \frac{2c_{water}}{c_{ceramic}}.$$

6-8

Numerical examples are provided for three relevant piezoelectric materials in Table 6-1 in which one sees that the aspect ratio is sufficiently small by default for all materials with the exception of PZT 5A. This is a consequence of the higher wave velocity in AlN and $LiNbO_3$ and simplifies the array design given and one need not dice the array elements into sub-elements to avoid lateral modes.

Material	AlN	$LiNbO_3$	PZT 5A
Aspect ratio	0.27	0.41	0.82

Table 6-1: critical aspect ratio for lateral mode coupling

The ratio of height to thickness must also avoid mode coupling. However, in this case one will likely opt to make the element height much larger than the thickness thereby avoiding strong coupling. This choice results in a stronger focusing in the vertical plane, increased capacitance and hence better electrical impedance matching, and more acoustic energy.

6.3.3 Matching Layers

Matching layers are inevitable in most practical cases as they provide structural rigidity and protect the piezoelectric elements. The existence of shear waves in the solid matching layer has the potential to cause complications. The complications may potentially arise in general because one must consider multiple modes and diffraction, even if the solid is merely a $\lambda/4$ matching layer. Further, the shear velocity in a solid, such as aluminum or stainless steel is closer to that of water. This results in a closer match in acoustic impedance for the shear wave and thereby increased transmission of acoustic energy from shear waves in comparison to the longitudinal mode. Specifically, the echo transmittance function describes a plane wave impinging at an angle on a fluid-solid interface being transmitted, perfectly reflected and the returning to its place of origin. The echo transmittance may be found in (Schmerr & Song, 2007) and (Krautkramer & Krautkramer, 1977) and an example is provided for aluminum in Figure 6-5.

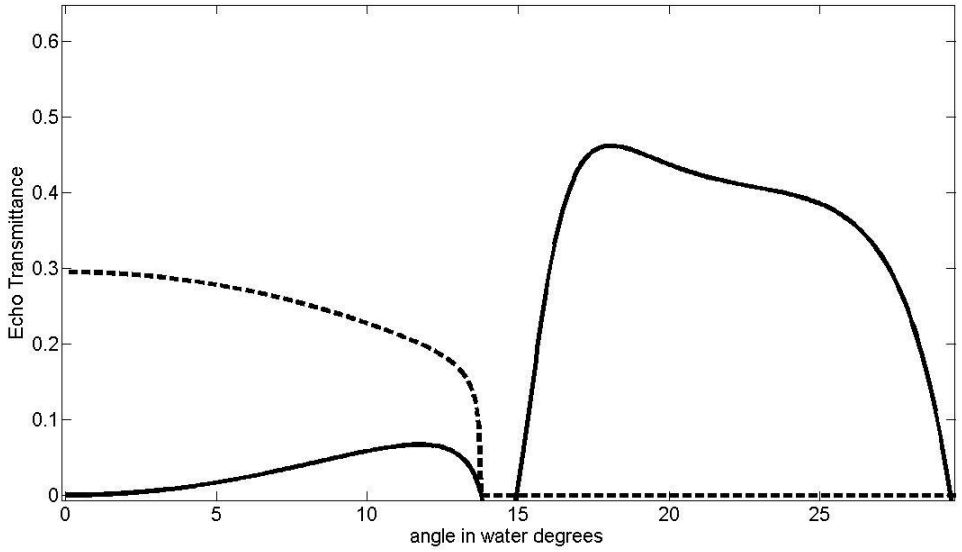

Figure 6-5 echo transmittance, dashed line-shear wave, solid line-longitudinal wave

This complicated angular dependence of the echo transmittance will reduce the performance of a phased array. This was confirmed by the experimentally when a phased array consisting of four Lithium Niobate elements was constructed utilizing a quarter wavelength Al matching layer front plate. The array was used in a sectorial scan mode while a thin rod was translated parallel to the array. The echo amplitude from the rod was recorded as a function of the angle of the rod location and is presented in Figure 6-6.

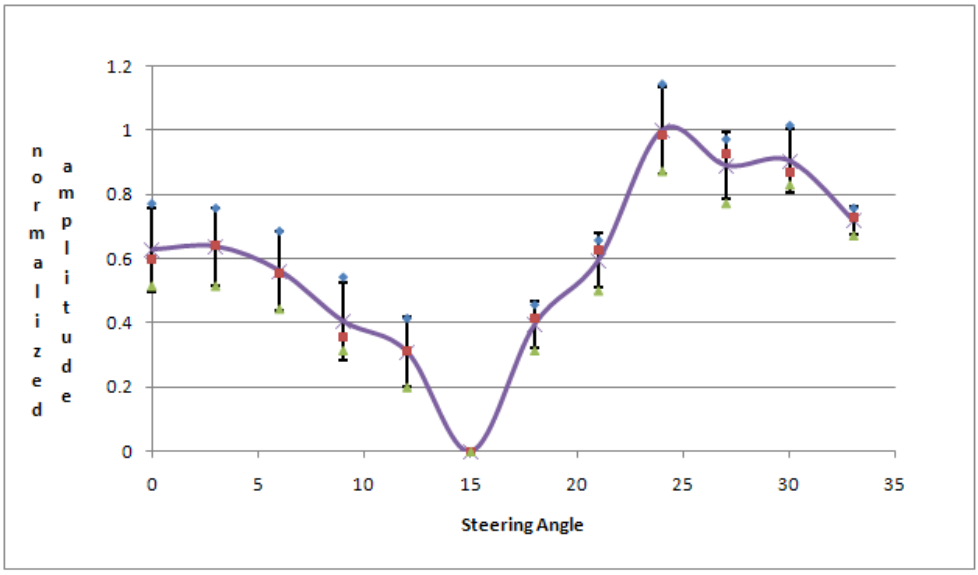

Figure 6-6: Experimentally obtained echo amplitude from a phased array versus beam angle

In general this effect is mitigated by utilizing matching layers which possess an acoustic velocity similar to that of the propagation medium and/or partially dicing the matching layer. In a high temperature radiation environment low velocity materials must be specially engineered as the typical polymer based materials will not suffice.

6.3.4 Mutual Impedance

When two piezoelectric elements operate in close proximity to one another their interaction has the potential to drastically alter their performance. For example, the presence of another element on the *z=0* plane immediately implies one has neither a pressure release nor a rigid baffle. Additionally, mutual impedance occurs when element *a* is excited by the pulser and generates a pressure or stress wave that encounters element *b* as element *b* is excited by the pulser to generate its own wave. This phenomenon may be understood in terms of acoustic impedance. In the case of a single element the

acoustic impedance of the medium simply relates the particle displacement in the medium to the pressure and depends only on the material and the element geometry. With an array however the acoustic impedance depends on the entire array and in the case of an array of circular elements of radius *a* and pitch *d*

$$p = z_{11}U_1 + Z_{12}U_2 + \cdots Z_{1N}U_N$$

where

$$z_{MN} = \frac{\rho c}{\pi a^2}\frac{(ka)^2}{2}\left[\frac{\sin(kd_{MN})}{kd_{MN}} + j\frac{cos(kd_{MN})}{kd_{MN}}\right].$$

6-9

This expression of course is exact only for continuous wave operation but will be approximate for elements that are only a few wavelengths from one another in a broadband array. The expressions above for mutual impedance are taken form the Elecro-Acoustic Transducers course taught at Penn State by Dr. Gabrielson.

6.4 Full Matrix Capture

Ultrasonic arrays are not always phased and a popular method, sometimes referred to as the full matrix capture method (FMC). The full matrix capture method involves exciting a single element, for example element 1, receiving with all the elements for example 1 through 3, including the excited element. This first transmit and receive sequence results in 3 A-scans which will comprise the first row in a matrix. This procedure is then repeated for all transmit receive pair to obtain a matrix of the sort

$$M = \begin{matrix} A_{11}(t) & A_{12}(t) & A_{13}(t) \\ A_{21}(t) & A_{22}(t) & A_{23}(t). \\ A_{31}(t) & A_{32}(t) & A_{33}(t) \end{matrix}$$

6-10

The focusing is then accomplished by means of post processing. The post processing involves first selecting a focal point in the acoustic field and identifying the corresponding coordinates (x_f, y_f).

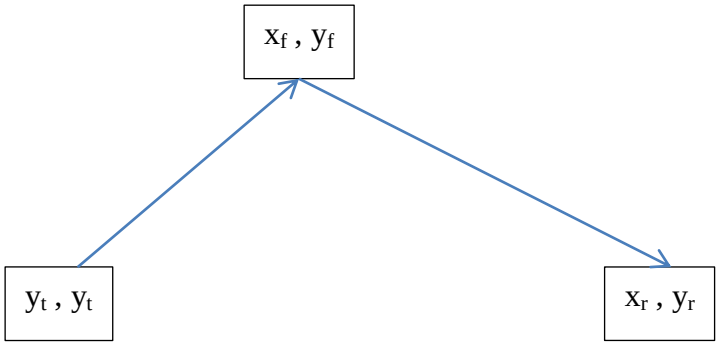

Figure 6-7: Diagram illustrating time of flight calculation for full matrix capture post processing

As one can see from Figure 6-7 the time it takes a wave generated at the transmitter, with coordinates (x_t, y_t), to travel to the focus and then be reflected or scattered to the receiver with coordinates (x_r, y_r) is

$$t_{tr} = \frac{\sqrt{(x_f - x_t)^2 + (y_f - y_t)^2 + z^2} + \sqrt{(x_f - x_r)^2 + (y_f - y_r)^2 + z^2}}{c}$$

6-11

where c is the speed of sound and the linear array lies in the $z=0$ plane. Once t_{tr} is calculated the A-scan $A_{tr}(t)$ is sampled at this location. This process is repeated for all transmit receive pairs and the sampled A-scans are summed to arrive a numerical value which will be assigned to a pixel in a B-scan. The B-scan is developed by sweeping (x_f, y_f) and assingning the pixel values as described above. The matrix 6-10 is often reduced based on the assumption of reciprocity which state that $A_{nm}(t) = A_{mn}(t)$.

The FMC method is subject to the same requirements presented in chapter 6.3 with the exception of mutual impedance effects provided the delay between excitations is sufficient. The ability to reduce mutual impedance effects may be an overlooked attribute of the FMC method. Ultimately the two way beam pattern ends up being identical to that of the phased array. However, the FMC method has the advantage of requiring simpler hardware than the phased array method. In fact the first experiment conducted by the author utilized the same equipment used for A-scans and nothing more, aside from some manual labor. Although application of the FMC is typically facilitated greatly by utilizing additional hardware to do the switching.

On the other hand the SNR is reduced in contrast to the phased array method due to the lack of focus during transmission. The reduction can be understood by considering the time it takes to carry out the FMC process, which is longer than that of the phased array. However, once the A-scans are obtained in the FMC one may digitally process them to their hearts content, which cannot be done economically with phased array methods.

Coded excitation is an excellent and highly effective technique which is readily implemented with the framework of the FMC method. For an excellent discussion of coded excitation in methods the reader is referred to (Mahafza, 2009).

6.5 Synthetic Arrays

The synthetic array focusing technique, SAFT, may be thought of as a simplified version of the FMC method where only the A-scans on the diagonal of 6-10 are utilized. As such, it is possible to utilize the SAFT with only one transducer and a mechanical scanner. Early manifestations of synthetic focusing involved a moving airplane, where the airplane becomes the mechanical scanning device.

The two way beam pattern of the synthetic array differs from that of the phased array and the FMC array since it is given by the sum of the contribution from each element after the transmit and receive beam of each element is convolved. The beam pattern is thus written as

$$u = \sum_{n=1}^{N} e^{ikdnu} \cdot e^{ikdnu} = \sum_{n=1}^{N} e^{2ikdnu}$$

6-12

which show that the grating lobes move in towards the main lobe by a factor of 2. A two way beam pattern from a synthetic array is compared an equivalent pitch and length phased array or a FMC array Figure 6-8. In Figure 6-8 the beam has been steered to 25^{o} degrees and the elements are modeled as dipoles. The directivity of the dipole causes the grating lobe to be reduced in amplitude compared to the mainlobe. This element

directivity may be used to nearly eliminate the grating lobes if highly directive elements are used and the steering range is minimal.

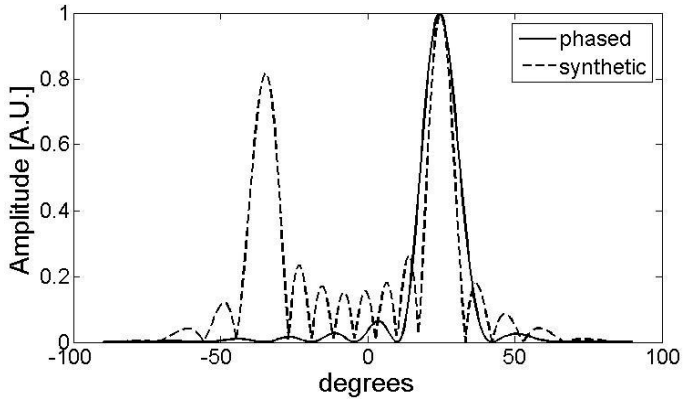

Figure 6-8: Comparison of a synthetic array to a phased array of equal length, elements are modeled as dipoles

provides the axial focal point and raster scanning provides volume coverage.

6.6 Apodization

Apodization is the use of variable gain applied to the array elements, i.e. element two is driven by a voltage which is different form element one etc. Naturally one has the option of applying the variable gain during transmit, receive or both. It seems to make more sense form a signal to noise ratio standpoint to apply only during reception, however typical discussions describe the one way radiation pattern. All common apodization schemes are symmetric about the center of the array and decrease toward the array ends. This sort of distribution will give lower side lobes and for large angles the side lobes will fall off as $1/\sin^2(\theta)$ (Hansen, 1997). A list of common apodization schemes is provided below.

- Dolph-Chebyshev
- Taylor-One Parameter
- Gaussian
- Hamming
- Blickmore-Spellmire Two-Parameter
- Taylor N-Bar

Of course many other distributions exist. An example of the Dolph-Chebyshev pattern compared to the pattern of a uniformly excited array is provided in Figure 6-9 for a 16 element filled array.

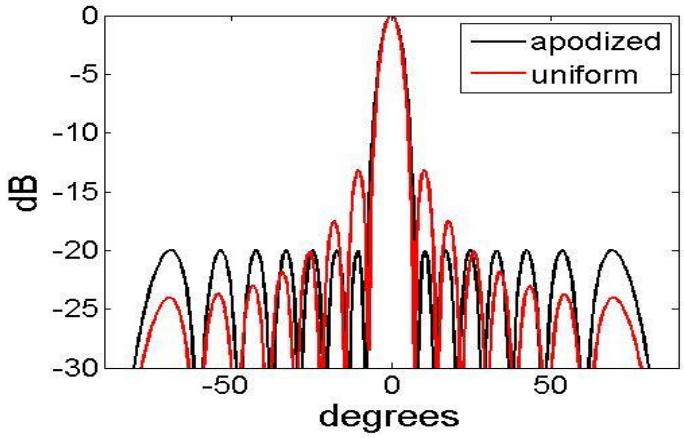

Figure 6-9: Beam pattern for a uniform and a Dolph-Chebyshev apodized 16 element filled array.

It can be seen from the picture the side lobes of the apodized array are indeed below that of that uniform array and they all have the same amplitude. The apodization in fact allows one to lower the side lobes in a controlled manner, however, the main beam will spread as the side lobes are reduced. It is worth noting that apodization does not reduce grating lobes.

7 Multilayered Media

7.1 Calculation of Delays

When focusing in multilayered media refraction causes the complications when calculating the time delays. The difficulty is demonstrated by equation and figure 7-1. Basic trigonometry and geometry yields the expression for the ultrasonic time of flight for a wave originating at element *i* to the intended focus and back to element *j*. The arguments within the *arcsin* function are the result of Snell's law.

$$t_{ij} = \frac{d}{c_{steel}}\left[\frac{1}{cos(\theta_i)} + \frac{1}{cos(\theta_j)}\right] + \frac{y}{c_{water}}\left\{\frac{1}{cos\left[asin\left(\frac{c_2}{c_1}\sin(\theta_i)\right)\right]} + \frac{1}{cos\left[asin\left(\frac{c_2}{c_1}\sin(\theta_j)\right)\right]}\right\}$$

7-1

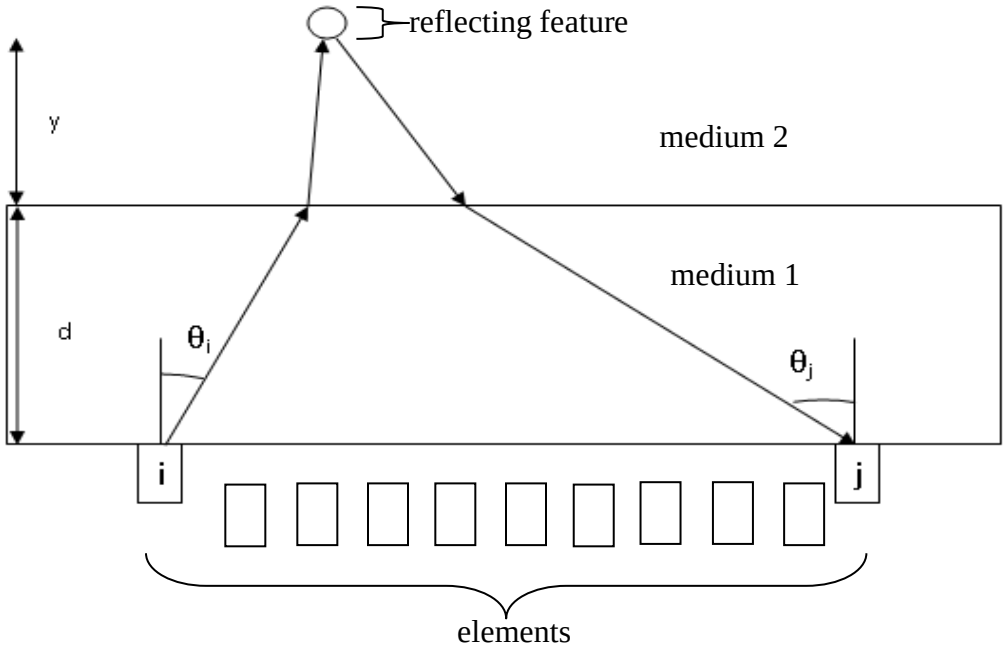

Figure 7-1: Ray tracing diagram for a reflector outside the pressure boundary

The case $i \neq j$ is only needed for the FMC approach. For now the synthetic array approach is considered, and hence an A-scan from the *i*th virtual element is sampled at

$$t_i = \frac{2d}{c_{steel}}\left(\frac{1}{\cos(\theta_i)}\right) + \frac{2y}{c_{water}}\left\{\frac{1}{cos\left[asin\left(\frac{c_2}{c_1}\sin(\theta_i)\right)\right]}\right\}$$

7-2

However, to apply the synthetic array algorithm one needs x_f and y_f thus begin by writing

$$x = a + b$$

where a corresponds to intersection of the ray with the second medium. The basic trigonometry gives

$$x = dtan(\theta_i) + ytan\left\{asin\left(\frac{c_2}{c_1}\theta_i\right)\right\}$$

which may be solved numerically for θ_i. So the procedure is as follows

- Compile A-scan data in accessible digital format
- Choose a focal point x,y
- Determine θ_i
- Calculate the time delay for the all virtual elements
- Sample the A-scans to obtain the pixel value of x,y
- Repeat for the desired field of view

The procedure described above has been applied to considering an element immersed in a fluid medium located 5 mm from a stainless steel medium to generate the time of flight versus position plot provided in Figure 7-2.

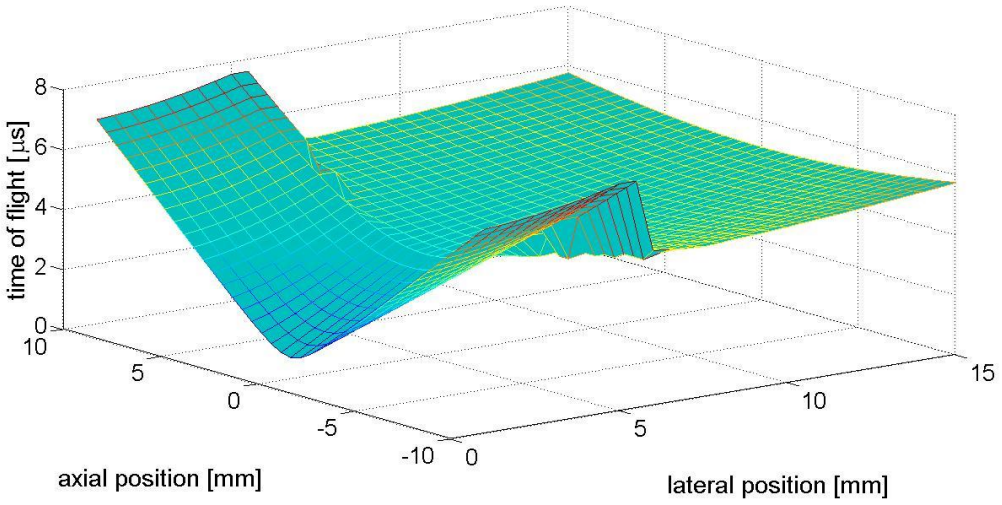

Figure 7-2: Time of flight surface for multilayered focusing

7.2 Transmission and Reflection

When acoustic energy moves form one medium to another a portion of the energy is reflected as given by the reflection coefficient. The situation is illustrated in Figure 7-3.

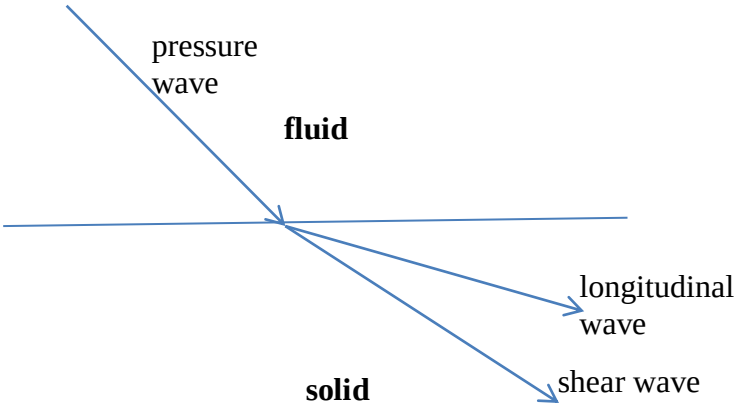

Figure 7-3: Wave transmission between a fluid and a solid at oblique incidence

Respectively, the transmission coefficient, in terms of particle velocity, for pressure wave to longitudinal wave and pressure wave to shear wave are (Schmerr & Song, 2007)

$$T_{F:S}{}^{P:L} = \frac{2\cos(\theta_P)[1 - 2\sin^2(\theta_T)]}{\cos(\theta_L) + \frac{\rho_s c_L}{\rho_f c_P}\cos(\theta_P)\Delta}$$

$$T_{F:S}{}^{P:T} = \frac{-4\cos(\theta_P)\cos(\theta_L)\sin(\theta_T)}{\cos(\theta_L) + \frac{\rho_s c_L}{\rho_f c_P}\cos(\theta_P)\Delta}$$

where

$$\Delta = 4\left(\frac{c_T}{c_L}\right)^2 \sin(\theta_T)\cos(\theta_T)\sin(\theta_L)\cos(\theta_L) + 1 - 4[\sin(\theta_T)\cos(\theta_T)]^2. \quad \text{7-3}$$

In equation 7-3 the subscripts and superscripts *P*, *T*, *L*, *F* and *S* denote pressure wave, transverse wave, longitudinal wave, fluid and solid respectively. Equation 7-3 only depends on the material properties and a single angle, as the remaining angles are

determined via Snell's law. In the other direction that is from solid to fluid the transmission coefficients are given by

$$T_{S:F}{}^{L:P} = \frac{\rho_F c_P \cos(\theta_L)}{\rho_S c_L cos(\theta_P)} T_{F:S}{}^{P:L}$$

$$T_{S:F}{}^{T:P} = \frac{\rho_F c_P \cos(\theta_T)}{\rho_S c_T cos(\theta_P)} T_{F:S}{}^{P:T}.$$

7-4

Thus the echo transmittance is the product of equations 7-3 and 7-4.

7.3 Matching Layers

In addition to the fluid solid interface at the surface of the object being inspected, the front plate or matching layer is also subject to reflection and refraction as described above. The reflection is minimized and the transmission maximized in the case of a single λ/4 if the layer impedance is chosen according to (Vives, 2008)

$$Z_m = \sqrt{Z_p Z_f}$$

7-5

where Z is the acoustic impedance of the medium which is specified by the index m for mathching layer, p for the piezoelectric and f for the fluid. Technically the acoustic impedance of the piezoelectric is frequency dependent but more often than not the bulk impedance is assumed. Therefore, in the case of AlN and water one has Z_m=7.3 MRayls. Frequently ceramic loaded epoxy or parylene is utilized (Zhu, 2008). For example in the realm of medical ultrasonics researchers have sought a matching layer for human flesh, with an acoustic impedance of 1.5 MRayls, and they concluded that polymethylpenetane

is an ideal candidate (Sinha & Buckley, 2007). With an acoustic impedance of 1.7 MRayls and an absorption coefficient of 6 dB/cm along with structural toughness, polymethylpenetane is not ideal but is an excellent a compromise. The longitudinal and shear velocity of polymethylpenetane is 2.18 and 1.08 mm/μs respectively, which implies that shear waves will not transmit energy to the flesh. These shear waves originate from the edges of the piezoelectric where it contacts the matching layer. In the context of a harsh environment, such as a nuclear reactor core, polymer based matching are not applicable. However Aluminum with an impedance of 17 MRayls is fairly close as far as practical materials are concerned as is Titanium at 27 MRayls. These two materials have the added not developing and inordinate amount of fission gas and withstanding radiation and temperatures up to 500^{o} C quite well.

Aluminum is a particularly attractive choice as the author has found experimentally that a strong bond between AlN and Al is readily established by way of hot isotactic pressing at 500^{o} C and 150 psi. The resolution desired dictates 5 MHz and thereby dictates an Al matching lay 0.32 mm thick and may lead us to concerns of the fragile nature of this matching layer. In response to this concern one may simply add an additional matching layer. One may calculate the ideal impedance as (Vives, 2008)

$$Z_{m1} = Z_p^{\frac{3}{4}} Z_f^{\frac{1}{4}}$$

$$Z_{m2} = Z_p^{\frac{1}{4}} Z_f^{\frac{3}{4}}$$

7-6

Where Z_{m1} is the layer closest to the piezoelectric. For this application one has Z_{m1}=16.2 and Z_{m2}=3.3. Aluminum is an excellent choice for Z_{m1} and one can only wish that they were able to use an acrylic with $Z_{acrylic} \approx 3$ for Z_{m2}. However, tailored composites which are radiation hard will answer this call. Excellent work has been done (Zhu, 2008) in regards to nano-structured TiO_2 particles to careful controlled density to create superior matching layers.

8 Sparse Arrays

A sparse array is an array which does not meet the Nyquist criteria of λ/2 spacing between the elements. As mention in the chapter 1.2.3 sparse arrays enable a narrower beam than their filled counter parts due to the fact that the beam width is inversely dependent on the array length and weakly dependent on the number of array elements. However, the absolute gain of the array, that is the main lobe power divided by the power over the full angular range of visible space, cannot exceed that of a filled array. As a result a sparse array with a main lobe which is narrower than that of a filled array with the same number of elements experiences an increase in the side lobe level (SLL) (Schwartz, et al., 1998). The average SLL, normalized to the main lobe, of a "highly thinned" or very sparse array approaches $1/N_{removed}$ (Collin & Zucker, 1969) and randomly distributed elements allow for interesting and potentially useful predictions based on probability.

Additional benefits of sparse arrays include the reduction in mutual coupling and the ability to operate over a larger bandwidth without the development of grating lobes

(Collin, et al., 1969). Sparse arrays generally fall into three classes; periodic, deterministic aperiodic, and random (Schwartz, et al., 1998). The use of an algorithm to design an array by way of varying the phase, amplitude or location of the elements is often referred to as arrays synthesis.

The optimization of the array element locations is a nonlinear optimization problem since the variable is found in the argument of a complex exponential (Haupt & Werner, 2007). Additionally, a complete enumeration, where all possibilities are considered is generally impractical due to the number of possibilities. This of course depends on the size of the array and any imposed restriction on the total array length or maximum/minimum pitch. As an example, consider a 16 element array with the restriction of total array length being 30 wavelengths and the minimum spacing between any two elements being a half wavelength. This example is not chosen arbitrarily, as it has been shown (Agrawal & Lo, 1972) that the probability of generating a sparse array with improved performance increases as the number of elements increases; hence a 4 element array has little chance of being improved by randomly placing elements. The minimum spacing restriction is based on the desire to optimize an array that can actually exist physically, as one cannot place elements infinitesimally close in reality. The total length of the array will ensure that the beam is narrowed. The number of possible configurations can be determined by first creating the filled array of the same length and determine the number of elements therein, in this case 59 (based on $\lambda/2$ pitch). Then place the first of the 16 elements in one of the 59 locations, followed by the placement element 2 in one of 58 locations. At this point there are 59*58 configurations one could have chosen. This pattern continues until all 16 elements are distributed and hence

writing the pattern out and extrapolating one finds the total number of possible configurations to be $N_{filled}!/(N_{filled}-N_{sparse})!$ where N_{sparse} is 16 and N_{filled} is 59 in this case so one has 2.2955×10^{27} possibilities. Additionally there are many local minima so gradient searches fail to find the global minimum (Haupt & Werner, 2007). Only the random aperiodic array considers this number of possibilities all other methods impose additional constraints.

8.1 Periodic Sparse Arrays

Periodic sparse arrays have a constant pitch which is increased beyond $\lambda/2$. As a result, in the case of continuous wave arrays of isotropic elements, grating lobes develop which are of equal amplitude to the main lobe. The grating lobes are located at angles where the phase shift between successive elements is divisible by 2π. If one does not assume the far field condition the relative phase shift between elements cannot perfectly meet the requirement of divisibility by 2π for all element pairs and hence the grating lobes are reduced an smeared out but remain a significant problem. Additionally when a pulse is utilized as opposed to CW operation the grating lobes (GLs) are reduced by a factor of to M^2/N where M is the number of cycles in the pulse and N is the number of elements (Bae, Sohn, & Park, 1991). This of course applies only for $M^2<N$. This GL dependence on pulse duration only applies directly to uniformly spaced filled or periodic sparse arrays. There have been several methods devised to reduce the grating lobes in periodic sparse arrays, one such method, U.S. patent 7207942 B2, takes the cross correlation of the signals received by two neighboring elements and deems the signal the

result of a grating lobe if the cross correlation peaks at a delay equal to one period of the operating frequency.

Alternatively, some applications require, or are limited to a narrow steering range and as such allow the use of directive elements which are blind to grating lobes (Bae, Sohn, & Park, 1991). This situation is in fact very common in ultrasonic arrays, given that the energy transmitted by piezoelectric element is dependent on the volume of the element and therefore an element width of one half up to a few wavelengths is utilized.

8.2 Aperiodic Determinist Sparse Arrays

Aperiodic determinist arrays rely on expressing the desired beam pattern as analytical function, often a series, e.g. Fourier, Bessel or Delta function series. The array pattern is the forced to match the desired function. However, these methods suffer due to the fact that the function utilized does not represent actual beam patterns (Hansen, 1997). Additionally, the pitch is required to not deviate far from $\lambda/2$ for the method to prove effective and as such implies that control over side lobes, as opposed to narrowing of the main lobe is the primary benefit of this method. This is significant due to the fact that "a uniform excitation allows all the amplifiers of the active antenna to be operated under the same optimal condition" and hence amplitude distribution is more cumbersome to apply than array thinning, (Bucci, 2010).

Another common method deemed aperiodic sparse, involves using a non-uniform pitch to emulate the beam pattern produced by a uniform array with an amplitude distribution (apodization), that is

$$f_{sparse}(u) = 1 + 2\sum_{n=1}^{N} \cos(2\pi x_n u) = f_{filled}(u) = 1 + 2\sum_{n=1}^{N} A_m \, cos(2\pi dnu)$$

8-1

where the array is assumed to be symmetric about its center, hence the complex exponential is reduced to a cosine and the total number of elements is 2N+1. Also note $u = \sin(\theta)$, x_n is the location of the nth element in the sparse array, A_n is the amplitude of the excitation of the nth element in the filled array and d is the uniform pitch in the filled array. In this case the equality may be meet if and only if the minimum spacing in the sparse array is allowed to vary continuously (Collin & Zucker, 1969). In essence the result requires the density of the array elements per unit length along the array follow the same distribution as the amplitude distribution in the filled array. In general this results in a higher density of array elements towards the center of the array. The result may be quantify by dividing a plot of the amplitude distribution into equal areas and locating an element at the center of each equal area as illustrated in Figure 8-1.

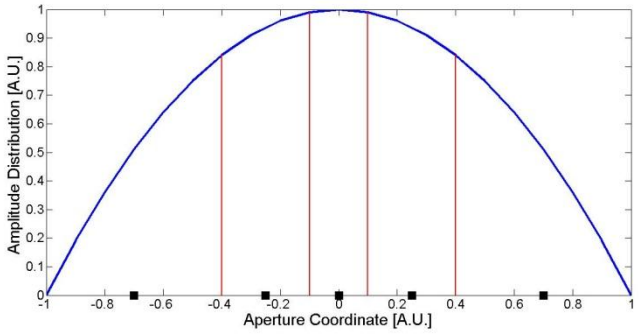

Figure 8-1: Illustration of rule of equal area for element density dased on aopdized continuous aperture

The following table shows the resulting 3dB beamwidth and SLL of thinned arrays based on the Taylor one-parameter distribution and the thinning methodology described above (Hansen, 1997).

SLL [dB]	N/N_o	$\theta_{3dB}/\theta_{3dB0}$
-13.26	1	1
-15	0.9133	1.042
-20	0.7562	1.156
-25	0.6647	1.26
-30	0.603	1.355
-35	0.5577	1.443
-40	0.5223	1.524

Table 8-1: Resulting SLL and 3 dB beam width for thinned arrays based on the Taylor one-parameter distribution

More recently, (Bucci, 2010) has utilized a similar approach with a slight modification by applying a cost function based on 8-1 in a segmented manner. This enables the equality of 8-1 to be very nearly meet provided the angular range is small and the maximum pitch remains relatively small.

Moffet, 1968 discusses the use of a minimum redundancy algorithm for optimum array performance. Minimum redundancy can be explained readily with the assistance of Figure 8-2. In Figure 8-2 an array is presented on the left with the blue representing elements and the yellow represented empty slots. The corresponding spatial frequency graph is shown on the right of each array. The upper two arrays are minimum redundancy arrays since each spacing occurs just one time. For example in the upper most array the spacing between the element at 0 and that at 1 is 1, the spacing between the element at 1 and that at 3 is 2 and the last two element combination spacing is between the element at 0 and that at 3 which is a spacing of 3.

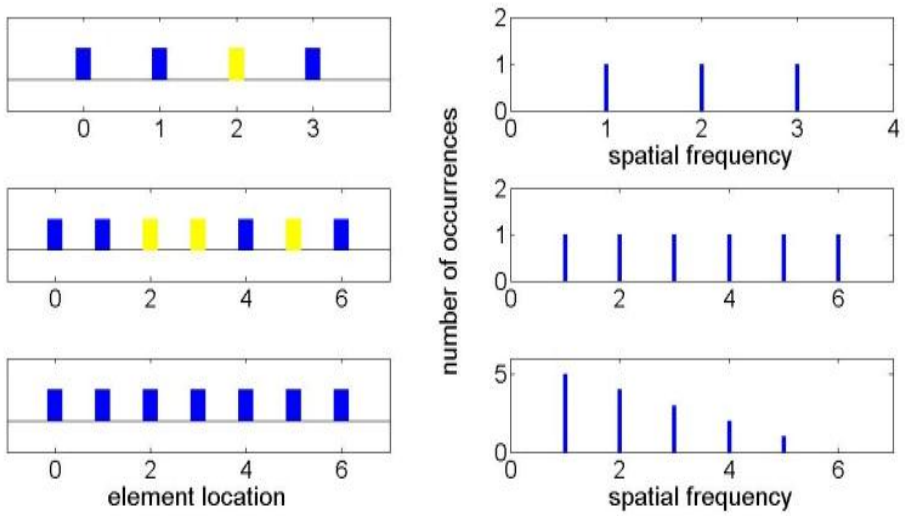

Figure 8-2: Depiction of a two minimum redundancy arrays and one filled array and their corresponding spatial frequency graphs. The yellow bars indicate the absence of an element.

Figure 8-2 may lead one to believe that designing a minimum redundancy array is easy to achieve, however if one tries to design an array with more than four elements it is quickly seen that this is not the case and in general it is difficult to go from the graph on the right of Figure 8-2 to that on the left. Minimum redundancy is in fact a thoroughly studied topic in the field of number theory. It is stated that the minimum redundancy array gives the *best* resolution for a given number of elements (Moffet, 1968). However, modeling these arrays in MatLab with a nonzero steering angle reveals that the minimum redundancy arrays result in significant side lobes and hence low gain. Moffet's work was aimed at creating an array of earth based receivers for pinpointing the location of galactic radio sources. As such Moffet did not consider steering the arrays of his published analysis. This method however, enables one to say with some confidence that they have arrived at a global optimum even for a large number of elements as it has been

determined that the minimum redundancy for a large number of elements is between 1.217 and 1.332. Again however, this is not the optimum one seeks given no mention is made of contrast resolution.

8.3 Random Sparse Arrays

Random sparse arrays are generated by an iterative algorithm that seeks to minimize a given cost function. The equality of the radiation pattern and an analytical expression is not sought after in a controlled manner as was done with deterministic sparse array synthesis methods. For example, one could utilize what shall be referred to as a Guess and Check algorithm wherein a random number generator is used to assign the pitch between elements in an array which is simulated by means of a diffraction model. One may then define the cost function as the beam width scaled by the maximum SLL. This process is then repeated many times and the arrays which result in a cost function output less than a specified value are saved to memory for further scrutiny.

Non-deterministic algorithms result in arrays with a more or less random distribution and as such probability theory plays a role in predicting the arrays performance, specifically in terms of SLL. It was shown that a maximum side lobe level below a specified value for a sparse array is more likely to be achieved if the sparse array contains many elements (Agrawal & Lo, 1972). Specifically, the probability is written in terms of the array length, the side lobe level in dB, and the number of elements. The probability is then given by

$$P = [1 - e^{-\alpha}]e^{\left[-\frac{2L}{\lambda}\sqrt{\frac{\pi\alpha}{3}e^{-\alpha}}\right]}$$

where $\alpha = \frac{N}{SLL}$ (Hansen, 1997), (Agrawal & Lo, 1972). This probability is illustrated for an 8 element array in

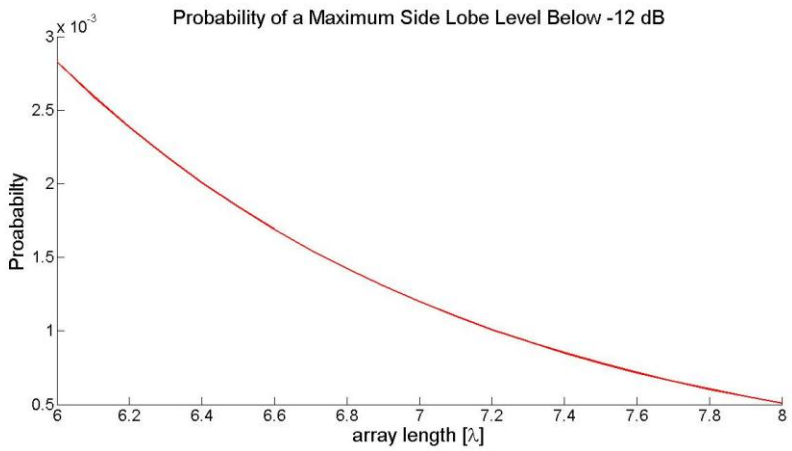

Figure 8-3: Probability of a maxim SLL below -12 dB for an 8 element array

Note that in Figure 8-3 a filled array would correspond to and array of 4 λ length. This figure indicates that doubling the array length by randomly distributing the elements will require on average 2 thousand attempts to achieve a side lobe level below -12 dB. Since this dissertation will ultimately be utilizing nonlinear optimization algorithms, which typically include a subsequence that involves the introduction of a randomly chosen variable, the result of 8-2 is of substantial importance. The fact that a typical sparse array will not be allowed a pitch of less than λ/2 makes 8-2 a bit unrealistic, and the repercussions of this are discussed in chapter 10.

Genetic algorithms are effective and quite popular in non-linear optimization problems and sparse arrays optimization presents no exception to this popularity. A

genetic algorithm takes the a population of arrays generated from a random sweep or a-priori knowledge and combines the "fit" arrays with some mutation to produce a second generations from which the fit candidates are again selected and allowed to reproduce for the third generation and so on. The fitness is determined by a cost function applied to the simulated array performance.

The genetic array is capable of manipulating the beam, at least from an array of many elements, in some quite remarkable ways as can be seen in (Haupt & Werner, 2007). The lowering of side lobes by an optimization of element position with the genetic algorithms appears to be limited to arrays with a large number, i.e. 100s, of elements. As Haupt and Warner have pointed out, the genetic optimization is resistant to getting stuck in a local optimum by virtue of the mutations that are invoked each generation.

The statistical density taper array is an additional array synthesis technique which most likely falls under the heading of random sparse. This approach is similar to the deterministic density taper. However, in this case the elements are distributed by utilizing a uniform array amplitude distribution to assign a probability for an element to be located within a section of the array.

The final method to discuss under the heading of random sparse arrays is that of simulated annealing. This algorithm utilizes an initial guess for the variables which are placed in the cost function and modifies the initial guess in a random manner. The extent of the modification on each iteration increases with "temperature". The modified

configuration is then accepted not only of the cost function returns a lower value than the previous iteration, but also if the following equation is satisfied

$$r \leq e^{[f_{i-1}-f_i]\frac{1}{T}}$$

8-3

where f_i is the resulting cost function of iteration i and T is the temperature and r is a uniform random variable (Haupt & Werner, 2007). One can see that this procedure is resistant to getting trapped in a local minimum since it may move to a new configuration of variables even if the new configuration results in a higher cost function.

9 Beam Diffraction Modeling

9.1 Introduction

The optimization of a sparse ultrasonic array is one of the primary aims of this dissertation. The optimization scheme will consist of a fitness function based on the side lobe level and main lobe width of a beam pattern produced by a sparse array. The beam is modeled by solving diffraction integrals with various assumed boundary conditions. The sparse array pitch configuration is allowed to vary and configurations which meet criteria placed on the fitness function will be saved for further analysis. The beam must be modeled with little computational effort but yet be realistic. If the model used in optimization does not represent the reality one has a practice in futility. To model a phased array accurately one should consider:

A. Pulse spectrum

- Most basic model assumes stationary fields

B. Matching layers
   - Thin solid material supports longitudinal, shear and guided waves all of which may be transmitted to the fluid

C. Element width
   - The simplest model assumes isotropic elements

D. Baffle conditions
   - Modifies the directivity of narrow elements

Even an ambitious plan such as this is short sited in that it does not account for cross talk or mutual impedance and as a result is more applicable to the consideration of synthetic of FMC arrays. If nothing else the discussion in this chapter provides assurance that one is not optimizing and overly simplified model. To develop such a model one begins by modeling the acoustic beam of an individual element. The linearity of the wave equation then allows us to simply sum the contributions from many elements to obtain the beam produced by the array.

9.2 Beam Pattern for a Baffled Source in a Fluid

To begin consider the directivity of a single radiator, the simplest array model was described in chapter 6 and results in equation 6-1 for the beam pattern, this chapter will develop an understanding of how accurate this model is for the context of this dissertation context. The directivity of an arbitrary aperture can be analyzed by use of the Huygens-Fresnel principle. To begin consider the wave equation

$$\nabla^2 p - \frac{1}{c^2}\frac{\partial^2 p}{\partial t^2} = 0$$

9-1

where p is the pressure and c is the wave speed. Fundamental solutions to 9-1 are spherical wave type, plane wave type. A choice of solution is then required to satisfy the relevant boundary conditions, in this case there is a prescribed pressure on the plane at z=0 as can be seen in Figure 9-1. One may proceed by assuming a spherical wave solution and applying Huygens' principle namely that each infinitesimal point on the aperture produces a spherical wave described by

$$p(r,t) = p_o e^{-i\omega t}\frac{e^{ikr}}{r}$$

9-2

where the wavenumber $k = \frac{w}{c}$.

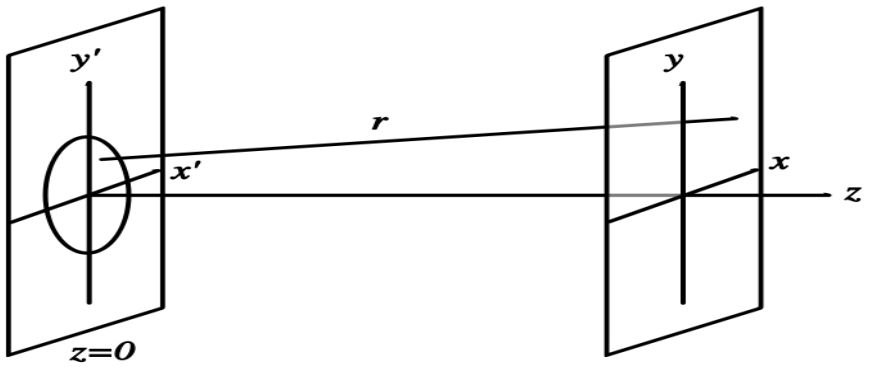

Figure 9-1:Coordinates utilized in directivity analysis

Next the superposition principle is utilized to sum all the contributions from each point on the aperture resulting in the Rayleigh-Somerfield version of a diffraction integral which is

$$p(r) = -\frac{i\omega\rho}{2\pi}\iint_A \frac{v(x',y')}{r} e^{ikr} dA$$

9-3

where $v(x',y')$ is the velocity distribution across the aperture, A is the area of the aperture, k is the wave number and ω the angular frequency (Schmerr & Song, 2007). The velocity on the aperture is utilized as opposed to pressure as is conventionally done. The current assumption is that on the plane z=0 at all points other than those on the aperture are completely rigid hence the velocity is zero but the pressure is not required to be and this is why the velocity is utilized in equation 9-3. All the expressions for pressure and velocity distributions in this section hereafter are scaled by $e^{-i\omega t}$ but this term is omitted without consequence aside from increased lucidity.

The rigorous solution does not rely on a rigid baffle assumption and expresses the velocity distribution in the form of the Helmholtz-Kirchhoff diffraction integral. To do so the first step is to notice that, if one assumes a spherical wave disturbance ψ such as pressure or particle velocity and place this in 9-1 one obtains the Helmholtz equation

$$(\nabla^2 + k^2)\psi = 0.$$

Green's theorem and a bit of manipulation (Goodman, 1968) then allows us to solve for the particle velocity field as

$$\psi(r) = \iint_S \psi(x', y') \frac{\partial G(\boldsymbol{r})}{\partial \hat{n}_A} + \frac{\partial \psi(x', y')}{\partial \hat{n}_A} G(\boldsymbol{r}) dA$$

9-4

Where $G(\boldsymbol{x}, \sigma)$ is the greens function and $\hat{n}_A$ is the outward unit normal vector equal to $\hat{z}$ in this case. In the case of a flat transducer surface radiation in the z direction the expression is (Szabo, 2004), (Presque & Fink, 1984),

$$G = \frac{1}{4\pi} \frac{e^{-ikr}}{r} . + R \frac{1}{4\pi} \frac{e^{-ikr\prime}}{r'}$$

9-5

where $r'$is a the mirror image of r and R is "to be determined" (Szabo, 2004). Specifically, if R is +1 then the normal derivative of Green's function vanishes along the plane z=0, if R =-1 then the Green's function itself vanishes along the plane z=0. The field ψ may be particle velocity or pressure or for that matter any disturbance which is described by the Helmholtz equation. As required by Green's theorem the surface of integration S in 9-4 is one that entirely encloses the acoustic field and hence one must know the disturbance or its normal derivative at all locations on this surface. A cross section of such a surface is illustrated in Figure 9-2.

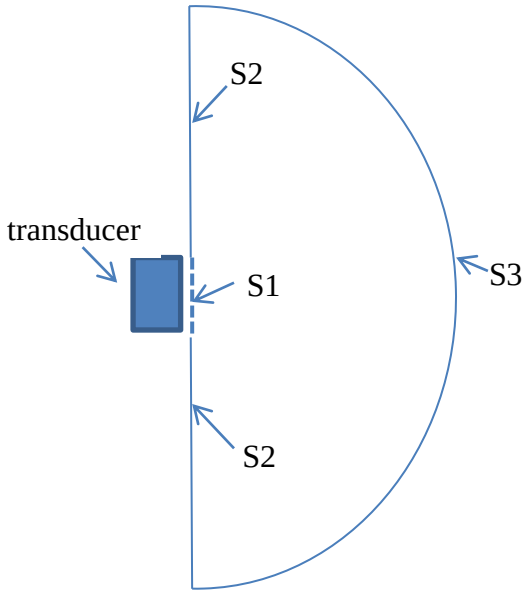

Figure 9-2: Surface of specified boundary conditions

In Figure 9-2 the surface is broken into three subsections and different reasoning is utilized on each surface to make the calculation of equation 9-4 possible. There is a substantial amount of formalism required to reduce 9-4 to tractable form, much of which may be found in (Goodman, 1968). Here a brief explanation is provided without the mathematical formalities. First off, S2 is neglected by means of the Summerfield radiation condition. It is important to notice that S1 is not in contact with the transducer r=0 because the chosen Green's function 9-5 fails to meet the requirements of continuity and differentiability imposed by Green's theorem. The most important surfaces *S1* and *S2* are dealt with by assuming the acoustic impedance is known at these locations. For example, if a rigid baffle is assumed the aperture displaces at will then one may choose ψ

to represent particle velocity at set the disturbance to zero along these surfaces alternatively if a soft boundary is assumed, which does not support pressure, one would instead choose ψ to represent pressure. In reality, the baffle will neither be perfectly soft nor rigid and the source will be affected by the field itself to some extent. To prescribe the field on the aperture amounts to a weak coupling condition. If one is not satisfied with the weak coupling condition then there are few options aside from finite element analysis. However, the weak coupling condition is widely accepted in this context. Fortunately, it has been shown (Presque & Fink, 1984) that all cases may be reduced to

$$v(r) = \iint_A \frac{X(\theta)v(x',y')}{2\pi r} e^{ikr} dA$$

$$X(\theta) = \frac{Z_{baffle}cos(\theta)}{Z_{baffle}cos(\theta) + Z}.$$

9-6

It can be seen that for the rigid baffle $Z_{baffle} = \infty$ and 9-6 reduces to 9-3 and hence Huygens' Principle gives the correct result for this limiting case.

9.3 Beam Pattern in a Isotropic Solid

A piezoelectric element placed in contact with a solid is frequently treated as having a pressure release baffle. This treatment is quite realistic provided the solid is a metal and the surface not contacting the transducer is in contact with air. Therefore, the particle displacement field is

$$\bar{u}_l(r) = \frac{p_0}{2\pi\rho c_l}\iint_S \hat{r}K_l(\theta)\frac{e^{ik_l r}}{r}dA$$

9-7

where p_o is the pressure, assumed uniform, on the radiation face of the piezoelectric, c is the elastic longitudinal wave velocity, θ is the angle between r and z (Schmerr & Song, 2007). The bar and carrot accents represent a vector and a unit normal vector respectively. Additionally, the subscript l indicates a longitudinal wave and the particle velocity is parallel to the radial vector. The term

$$K_l(\theta) = \frac{\cos(\theta)\,\kappa^2\left[\frac{\kappa^2}{2} - \sin^2(\theta)\right]}{2G[sin(\theta)]}$$

9-8

is essentially the only difference between equation 9-3, provided the velocity distribution is uniform, and simply narrows the beam a bit. Here θ is the angle between the z axis and a vector from the point on the radiating surface to the field point, κ is ratio of the longitudinal wave velocity to the shear wave velocity c_l/c_s and

$$G(x) = \left(x^2 - \frac{\kappa^2}{2}\right) + x^2\sqrt{1-x^2}\,\sqrt{\kappa^2 - x^2}$$

9-9

However, in addition to the longitudinal wave, shear waves are induced at the edges of the radiating surface and are distributed in the following way

$$\bar{u}_s(r) = \frac{p_0}{2\pi\rho c_s}\iint_S \hat{q}K_s(\theta)\frac{e^{ik_s r}}{r}dA$$

9-10

$$K_s(\theta) = \frac{\kappa^3 \cos(\theta)\sin(\theta)\sqrt{1-\kappa^2 \sin^2(\theta)}}{2G[\kappa sin(\theta)]}.$$

9-11

In 9-10 the particle velocity is along the vector $\hat{q}$, which is perpendicular $\hat{r}$. The shear waves exhibit polarization such that the projection $\hat{q}$ on the surface *z=0* is perpendicular to the nearest edge of the aperture. A comparison of the longitudinal particle displacement field from an evaluation of equation 9-7 and the pressure field of equation 9-6 with various baffle conditions is provided in Figure 9-3. Note that the axial distance is 20 wavelengths only when the angle is zero, as the radial propagation distance has been kept constant. Maintaining a constant radial distance, from the aperture center, allows us to see that the wavefronts are not truly spherical due to the variation in amplitude with angle, the phase (not shown) also varies but by less than π.

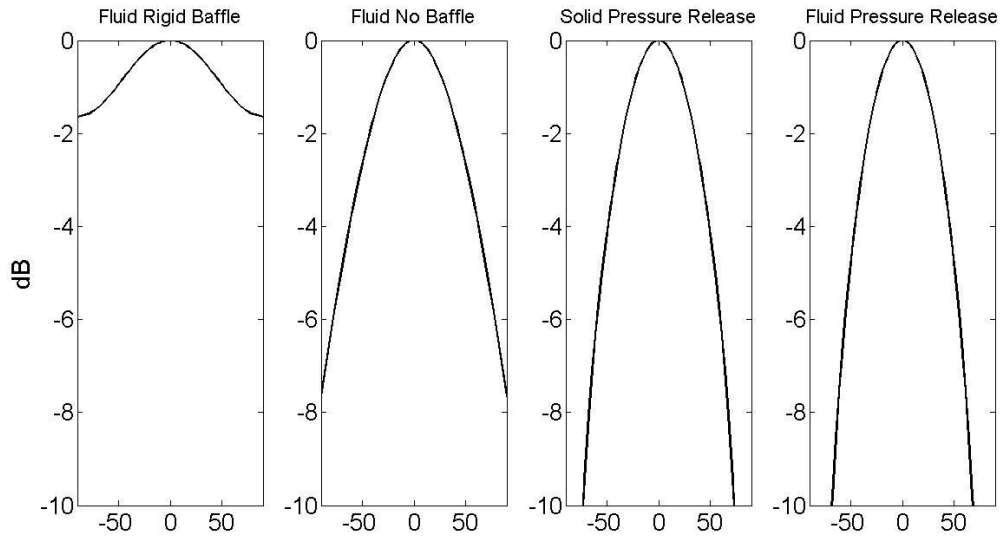

Figure 9-3: Beam patterns from a λ/3 element with various baffle conditions in a fluid and a solid

Figure 9-3 shows that the directivity pattern from a flat radiating surface with a pressure release type baffle depends greatly on the baffle conditions and the nature of the propagation medium. The difference is of greater importance when considering individual array elements which are typically on the order of λ wide so as to produce a wide beam and to allow for pitch which at least approaches the Nyquist criteria. As a result when considering array elements the discrepancies at large angles contain a significant portion of the acoustic energy, whereas your run of the mill contact ultrasonic transducer produces a narrow beam and hence little energy is present at the angles where the baffle effects make a difference. The effect will be even more dramatic in practice as the pulse echo beam pattern is the convolution of the transmit beam with the receive beam and therefore the 3 dB down angle becomes a 6 dB down angle.

In the construction of an array for use in the reactor core further complications will arise due to the existence of shear waves in the array front plate and as mentioned earlier the array front plate is a design necessity. The shear waves will emanate at relatively large angles as illustrated in Figure 9-4 , which was created by numerically solving equations 9-8 and 9-10, and be transmitted to the fluid where they will be superimposed on the pressure field generated by the longitudinal waves.

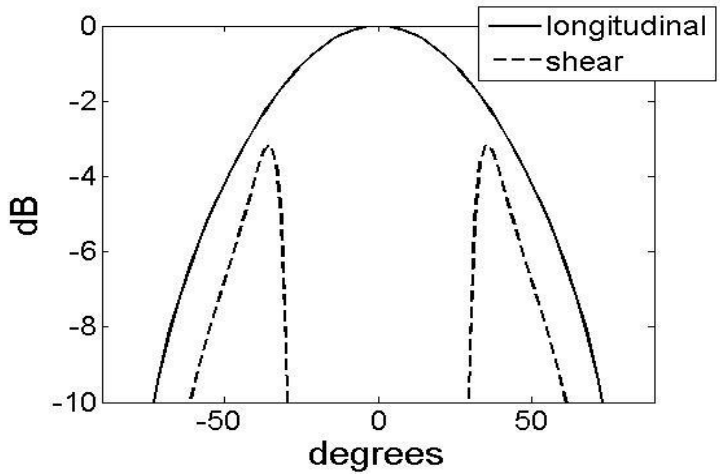

Figure 9-4: Acoustic field in aluminum from a λ/3 wide array element

As mentioned in chapter 6.3.3 the use of low acoustic velocity matching layers results in the shear wave propagating beyond the second critical angle will prevent this from occurring. Specifically, the obliquity factor, $K_s(\theta)$, has lobes on either side of the longitudinal lobe with 6 dB down angles at 20 and 70^o (for the positive angular range) and hence the second critical angle is reached and the shear wave will not contribute to the field in the fluid if the shear velocity in the solid is nearly equal to the wave velocity in the fluid. One may alleviate this situation by partially dicing the matching layer.

9.4 Finite Pulse Acoustic Field

All analysis up to this point has assumed continuous wave sources, which is illustrative, but is not the mode of operation utilized in typical ultrasonic NDE. However, substituting the frequency corresponding to the majority of energy in the operating bandwidth is typical and fairly accurate and hence is utilized to introduce the more fundamental principles and is common place in the literature. One may proceed to

develop a broadband model either by taking advantage of the linearity of the wave equation and obtaining the pulsed field by way of a linear superposition of the complex fields produced by each frequency contained in the pulse, or by way of a direct expression. The direct expression is given by (Goodman, 1968)

$$v(r) = \iint_A \frac{X(\theta)}{2\pi r} \frac{d}{dt} v\left(x', y', t - \frac{r}{c}\right) dA$$

9-12

where the obliquity factor is taken as cosine to account for the baffle. When calculating 9-12 one must select a differentiable pulse for $v\left(x', y', t - \frac{r}{c}\right)$ and to this end a Gaussian windowed sinusoid is chosen.

$$v\left(x', y', t - \frac{r}{c}\right) = e^{\frac{-\left(t - \frac{r}{c}\right)^2}{a}} \sin\left[\omega\left(t - \frac{r}{c}\right)\right]$$

9-13

This represents the velocity at the transducer surface delayed by the propagation time. In this example the constant a is set to one period to represent a well damped oscillation as illustrated in Figure 9-5 with the resulting field is shown in Figure 9 6..

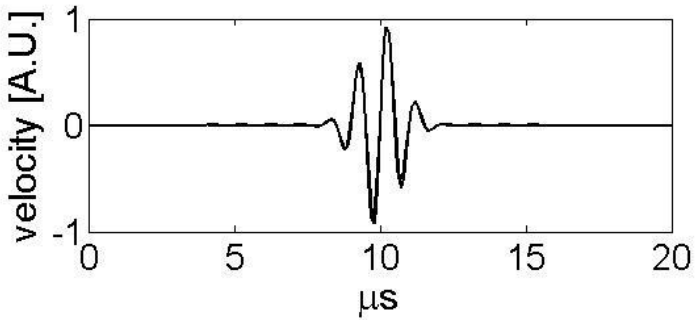

Figure 9-5: Pulse utilized for transient field calculation

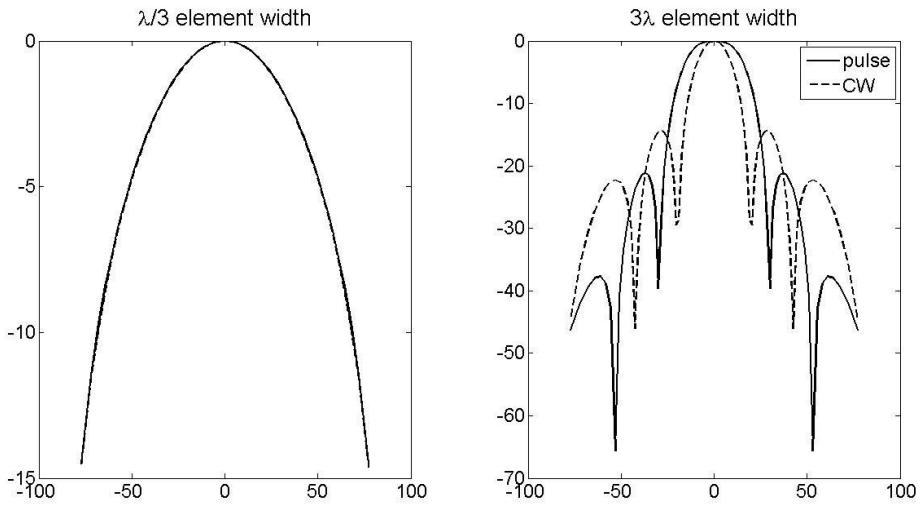

Figure 9-6: Comparison between pulsed and continuous wave fields

It can be seen from Figure 9-6 that the field of the pulsed transducer is very similar for a thin element (there are two beams in the left of the figure) but varies substantially for a wide element. A computationally less burdensome method which produces an equivalent result in the far field involves convolving the impulse response of the aperture with the excitation pulse in the time domain (Begaud, 2011), (Macovski, 1979). This amounts to

$$\psi(\theta,t,z) = \int_{-\infty}^{\infty} \frac{X(\theta)}{2\pi z}\delta\left(t-\frac{r}{c}-\varepsilon\right)\psi_{aperture}(\varepsilon)d\varepsilon$$

$$\psi(\theta,t,z) = \frac{X(\theta)}{2\pi z}\psi_{aperture}(t-r/c)$$

9-14

where the propagation length is manifested only as a time delay and the inverse amplitude dependence of on the axial distance, hence this is the Fraunhofer

approximation. This expression may be utilized to model an array by assuming θ is constant for across the individual elements but varies for one element to the next.

9.5 Matching Layers

It has been stated that 9-6 is capable of predicting the field produced by an element with a matching layer provided the correct obliquity factor is used (Presque, et al., 1984). FEM analysis has revealed that the matching layer must be very thin, thinner than λ/4, and partially diced for this to hold true. One may be tempted to assume that a λ/4 matching layer is too thin for diffraction to occur and hence the layer may be neglected. However, the aperture is on the order of $\lambda_{water}/2$ and the nearfeild is then $N = \frac{\lambda_{water}^2}{16\lambda_{layer}}$ with $\lambda_{water}<\lambda_{layer}$ and hence the farfield begins inside the matching layer.

9.6 Separability

Our model may be further simplified by assuming the directivity is separable and hence one may set *y* and *y'* to zero in the evaluation of the beam pattern. This procedure is justified provide that the Frensnel approximation is valid. The Fresnel approximation amounts to approximating the radius in the phase argument as

$$r = \sqrt{(x-x')^2 + (y-y')^2 + z^2} \cong z\left[1 + \frac{1}{2}\left(\frac{x-x'}{z}\right)^2 + \frac{1}{2}\left(\frac{y-y'}{z}\right)^2\right]$$

9-15

and replacing the radius in the denominator with *z*. The result is then

$$p(x,y,z) = -\frac{i\omega\rho}{2\pi}\frac{e^{-ikz}}{z}e^{-ik\left(\frac{x^2+y^2}{2z}\right)}\iint_A v(x',y')e^{-\frac{ik}{2z}(x'^2+y'^2)}e^{\frac{ik}{z}(xx'+yy')}dx'dy'$$

$$p(x, y, z) = p(y, z) \cdot p(x, z)$$

9-16

The Fresnel approximation is valid when $a \equiv \left(\frac{x-x'}{z}\right)^2$ and $b \equiv \left(\frac{y-y'}{z}\right)^2$ are small. To get a feel for the amount of error involved in utilizing the Fresnel approximation the pressure field, at a radial distance of 40 wavelengths for an aperture 1 wavelength wide and 4 wavelengths tall, is plotted in Figure 9-7.

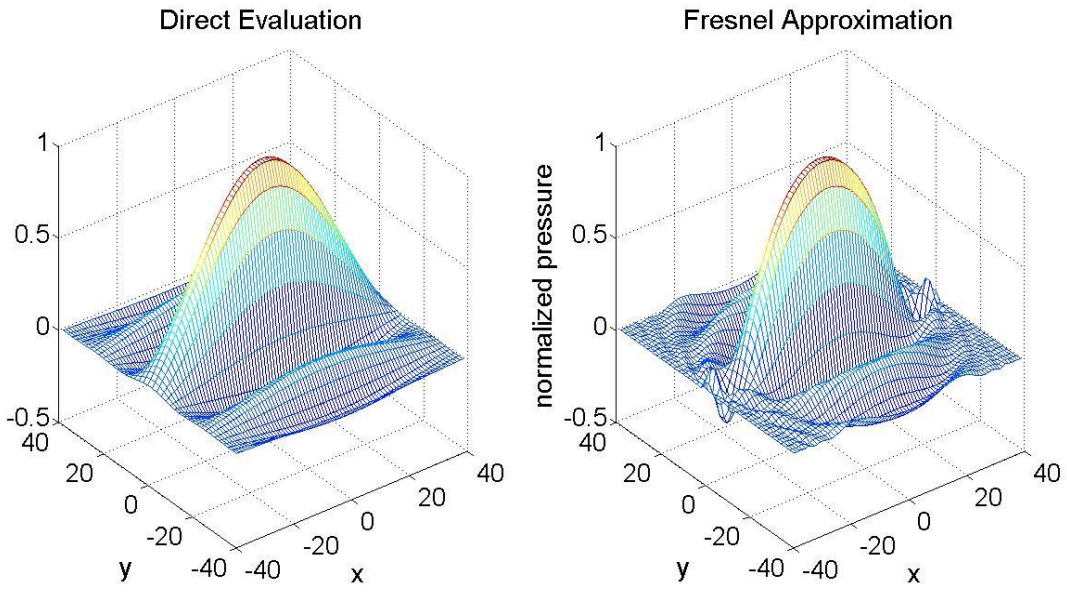

Figure 9-7: Pressure field from a 4 λ tall and 1 λ wide element at 40 λ axial distance.

The error in the Fresnel approximation is also plotted for the same scenario in Figure 9-8.

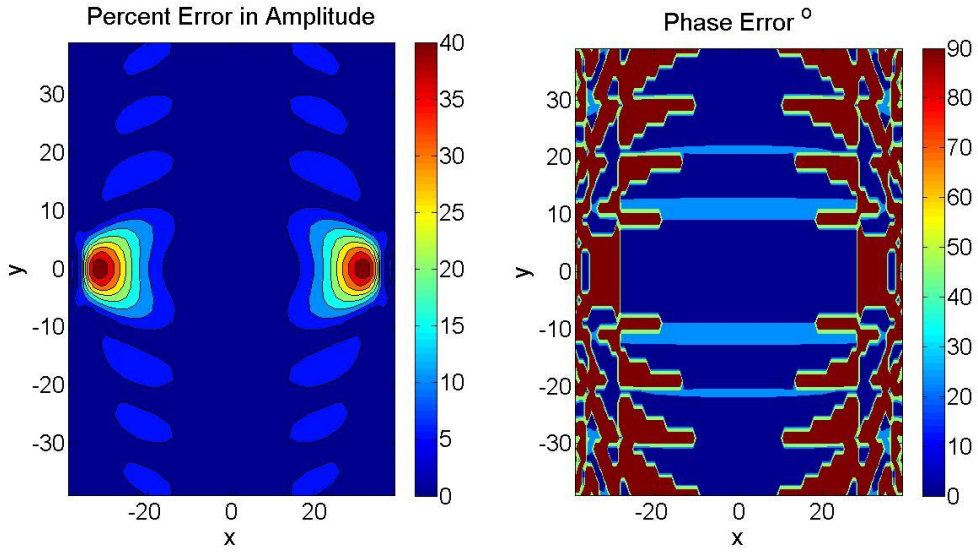

Figure 9-8: error in the Fresnel approximation for a 4 λ tall and 1 λ wide element at 40 λ axial distance

The combination of Figure 9-7 and Figure 9-8 show that the areas which are subject to the most error are also areas where little acoustic energy is present, all areas of 5% amplitude and 20^{o} phase error are also 10 dB below the main beam level in amplitude. Hence, one may utilize the Fresnel approximation in this analysis for the sake of computational efficiency.

It is common in fact, when modeling 1-D arrays, to utilize a closed form solution to the Fresnel approximation for the element directivity. This solution is

$$P(\theta) = sinc\left[\frac{kW}{2\pi}\sin(\theta)\right].$$

9-17

The error in this approximation is presented as the sum of the squared residuals for apertures of different widths in Figure 9-9.

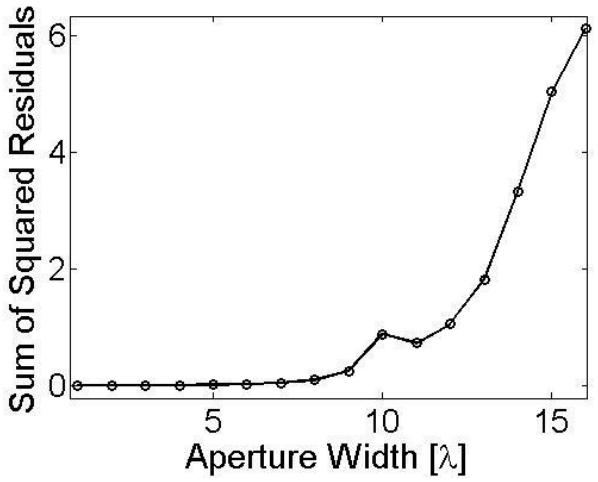

Figure 9-9: Accuracy indication for the closed form Fresnel approximation

9.7 Model of an Ultrasonic Array in the Time Domain

The tools needed to model an ultrasonic phased array either in the time of frequency domains are now available. The largest fallacy in this model is in the treatment of matching layers and the non-uniform displacement on the surface of the piezoelectric, for which there is no robust and accurate numerical or closed form model. However, the effect of the matching layer has been shown here to be negligible if the proper material and or dicing is utilized. Therefore, the time domain model may be obtained by summing the field of the array elements by means of

$$v(r) = \sum_{1}^{N} \iint_{A} \frac{X(\theta)}{2\pi r} \frac{d}{dt} v\left(x', y', t - t_n - \frac{r}{c}\right) \Pi\left(\frac{x - x_n}{W}\right) dA$$

where t_n is the time delay applied to the *n*th array element, x_n is the center location of the nth array element and *W* is the element width. An example of the resulting acoustic field for a 4 element array of λ/3 elements with a 1.5λ pitch focus at 20λ axially and 5λ laterally.

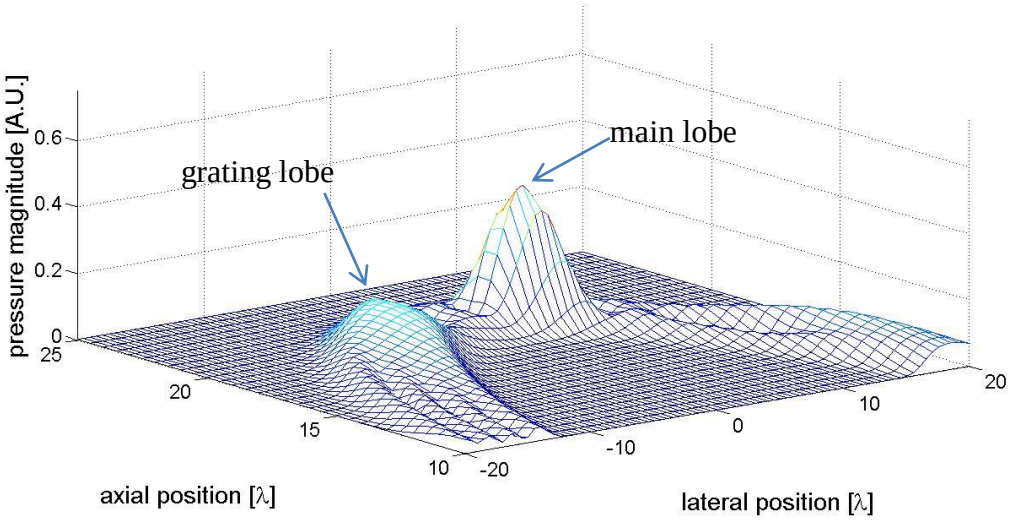

Figure 9-10: Time domain model of the acoustic filed generated by a 4 element array of λ/3 elements with a 1.5λ pitch focus at 20λ axially and 5λ laterally

The pitch was deliberately selected so as to produce grating lobes for illustration. It is observed that only one grating lobe is visible and the second grating lobe is outside visible space in accordance with equation 6-5. Additionally the grating lobe is roughly 7 dB below the main lobe as is to be expected with pulsed excitation. Alternatively one may utilize 9-14 and write the field produced by the array as

$$v(r,t) = \sum_{n=1}^{N} \frac{X(\theta_n)}{2\pi z} v_{element}\left(t - t_n - \frac{r}{c}\right)$$

which gives an identical result.

9.8 Chapter Summary

Much effort has been made here to determine the required complexity of an ultrasonic array model. The arguments are inevitably semi-quantitative due to the number of variables which include the baffle conditions, the element dimensions and the pulse spectral content. However, it has been shown here that provided one restricts the element to a reasonable geometry, namely on the order of a wavelength, and utilizes the proper matching layer, the ubiquitous directivity function given by 9-17 is reasonable regardless of whether the aperture is surrounded by a rigid baffle or by a pressure release surface. It must be stated that accounting for the matching layer and mutual coupling is best done by way of finite element analysis.

10 Optimization of a 1-D Phased Array

10.1 Introduction

In chapter 8 sparse arrays and the motivation for their consideration where explained. One may construct a logical argument that concludes a sparse array can, at least in theory, outperform the filled array in terms of spatial and contrast resolution. Typically, only one improvement is sought while the other is compromised by what is deemed an acceptable amount. The author asserts that this is not necessary and both resolutions can be improved by way of a sparse array, however not in a grand way particularly with a limited number of elements.

Linear methods are not applicable to the optimization of the element locations since the variables being optimizing against are contained in the argument of the exponent (Haupt, et al., 2007). Additionally, dynamic programming or optimizing subsets of the array in sequence is considered inapplicable because the "principle of optimality" had not been proven to apply in 1969 (Collin, et al., 1969) and presumably has not been proven to date. No attempt is made to prove it here.

On the other hand the beam pattern is linearly dependent on the complex amplitude of the array excitation and hence linear optimization may be utilized. As a result optimum excitation, or receive amplification, distributions are well established and common examples include the Chebyshev and Hamming apodization.

The tradeoff between main lobe width and side lobe level is not direct, but rather is manifested as a probability as was shown by (Agrawal & Lo, 1972). The trade of is best illustrated by the following table where a constant number of elements is assumed, which is a crucial distinction.

Fill Fraction	Beam Width	$P(SLL<SLL_0)$
↓	↓	↓
↑	↑	↑

In this table the fill fraction represents the percentage of positions occupied in a filled array of equal length to the sparse array and the SLL is the side lobe level in dB down from the main lobe. SLL_0 is the side lobe level of a filled uniform array of isotropic

continuous wave elements, which is -13.26 in the far field independent of nearly independent of array length beyond 10 elements. $P(SLL<SLL_0)$ represents the probability of generating an array with a maximum side lobe below SLL_0 by randomly placing the elements. The fact that this relation is given as a probability implies that it should in theory be possible to create a sparse array with a maximum side lobe as low as the filled array, but yet with a narrower beam. This will be made possible if the side lobe energy is uniformly distributed since absolute gain implies any energy taken from the main lobe by narrowing must show up in the side lobes. A quick inspection of the beam pattern of a filled array shows not only a nonuniform distribution of side lobes, but also many nulls. The uniformity could be improved and the nulls could be filled by energy taken from the main lobe as it is narrowed. The Dolph-Chebyshey apodization does an excellent job of the former and in fact can be used to narrow the main lobe while producing a maximum side lobe equal to the uniform array. This may not be obvious given that the Dolph-Chebyshev apodization is typically used to lower and redistribute the side lobes with moderate main lobe increase. However, if one accepts a uniform side lobe distribution limited to the level of the highest side lobe in the uniform array the main lobe is narrowed as shown in Figure 10-1.

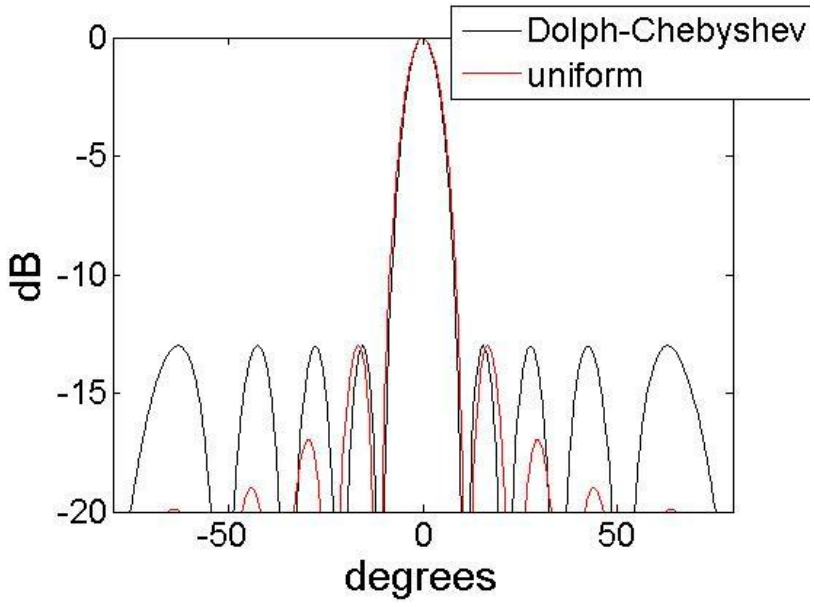

Figure 10-1: Dolph-Chebyshev apodization utilized to lower the maximum side lobe level

The narrowing is slight at only 0.6^{o} however the side maximum side lobe level has not increased. In conclusion it is physically possible to narrow the beam of an array without increasing the *maximum* side lobe level.

10.2 Preliminary Investigation of the Randomly Generated Arrays

The conclusion above, extended to random sparse arrays, is however, hindered by the fact that that a not every random array is physically realizable due to fabrication restrictions, such as finite element width which prevents two elements from by spaced by less than their own width. One may begin to get an idea of how the discrete restriction of element spacing effects the statistical predictions by running a random algorithm which generates many arrays with a fixed number of elements and a fixed width. Here a 16 element array that is 16 λ long and therefore twice as long as the filled counterpart is

simulated 50,000 times and the resulting probability for a given SLL obtained from a statistical analysis of the resulting beams is shown in Figure 10-2.

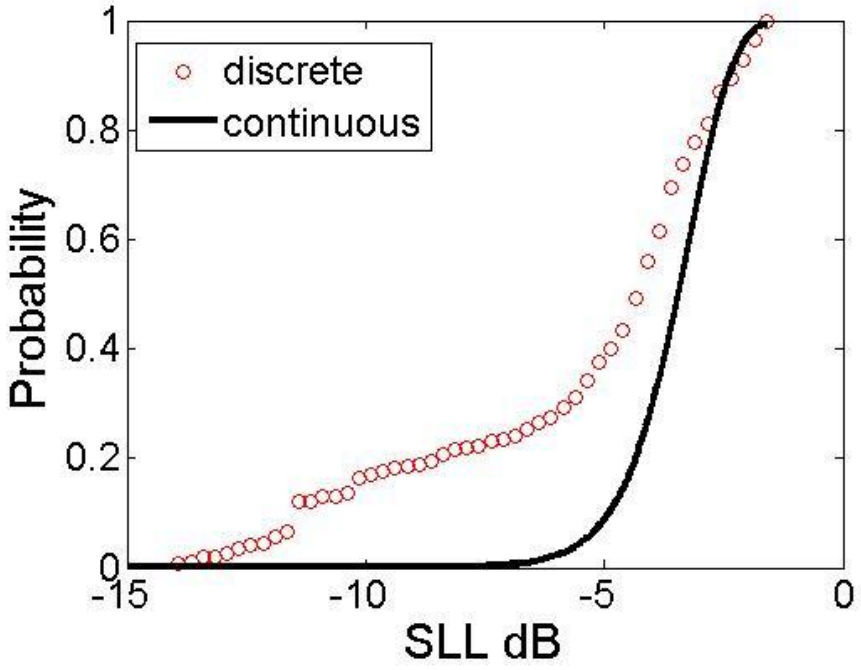

Figure 10-2: Theoretical probability and statically generated probability of a maximum SLL below the level indicated on the abscissa

It is now seen that there is a distinct difference on the statistics of the resulting SLL when the random discrete pitch algorithm is iterated 50,000 times. It appears that the discrete nature has increased the probability of a low SLL. However, running the model for many more iterations does not result in an extension of the curve above and it appears one may have reached the limit, although it is impossible to say one has checked the $3.9301 \text{ X } 10^{20}$ configurations required for an exhaustive search. Additionally this consistence check has revealed the range of beamwidths generated which should be "strongly dependent on the

array length but weakly dependent on the number of elements" (Bucci, D'Urso, Isernia, Angeletti, & Toso, 2010). The histogram of beam widths is shown in Figure 10-3 where one sees that the corresponding filled array beam width of 3.17^{o} (equation 6-4) is not generated even once.

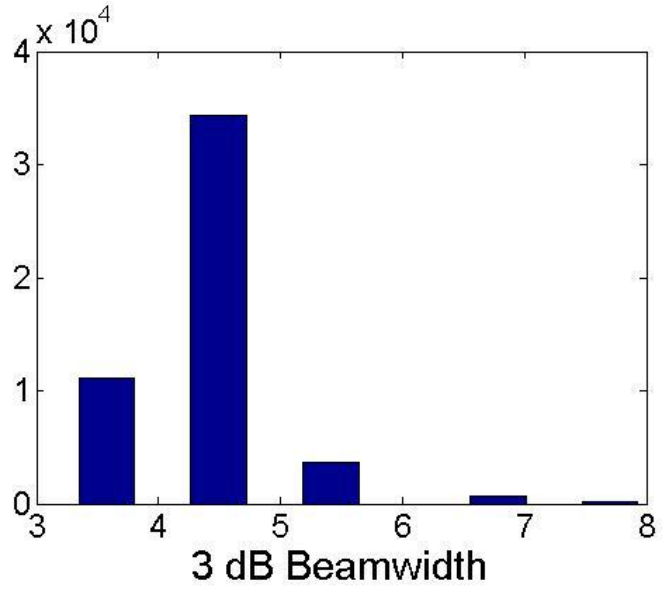

Figure 10-3: Beamwidth histogram generated form the random array algorithm

Possibly more revealing is the statistically generated plot of SLL versus beam width provided in Figure 10-4 which shows that the beam width and side lobe level follow a linear trend.

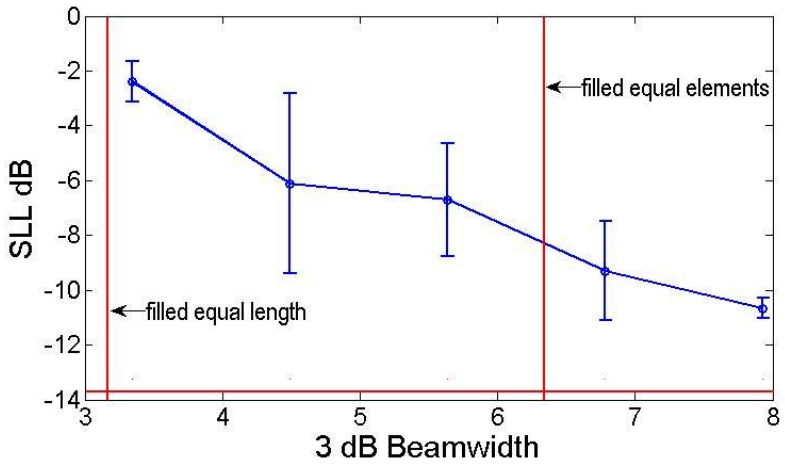

Figure 10-4: Statistically generated plot of SLL versus beam width

Fortunately if it is allowed the array length to be a bit more reasonable at 10 λ this trade of becomes less pronounced and one can in fact achieve superior performance by way of iterating a very basic random array "Guess and Check" algorithm a mere 50,000 times which takes only 94 seconds utilizing equation 6-2 in MatLab. The resulting beam is provided in Figure 10-5.

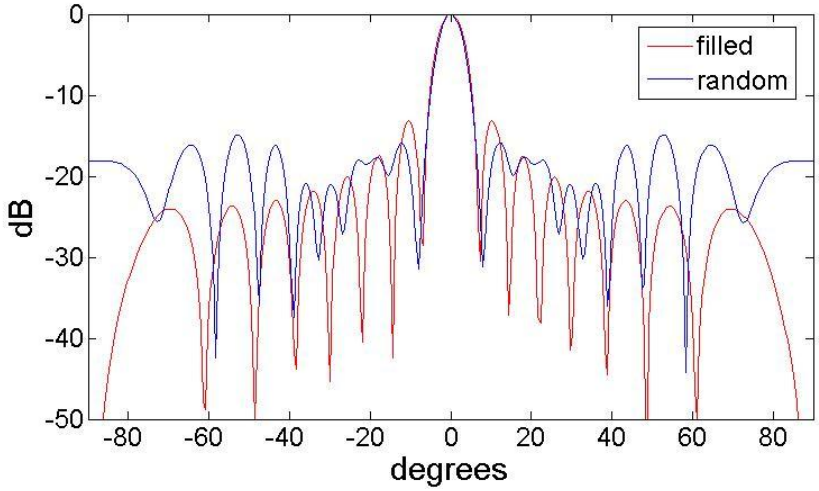

Figure 10-5: Random sparse array with lower side lobes and narrower beam

This is a very promising result, although, literature review leads one to believe that sparse arrays appear great in theory but in practice are a bit disappointing. The characteristics of this random array are provided in Table 10-1 along with those of a filled array.

SLL [dB]	3 dB width	6 dB width	pitch configuration	length
-14.9	5.8^o	8^o	2 1 1 1 1 1 1 1 1 1 1 1 1 1 5	10 λ
-13.2	6.3^o	8.6^o	1 1 1 1 1 1 1 1 1 1 1 1 1 1 1	7.5 λ

Table 10-1: characteristics of random sparse and filled array

10.3 Preliminary Experimental Investigation of Sparse Arrays

There has been little experimental evidence that a sparse array is indeed worth considering. Therefore, the author has devised a rather efficient method of experimentally checking the performance of sparse arrays presented in the literature. As opposed to fabricating a collection of ultrasonic arrays with element distributions according every promising synthesized array in this work and the literature, the synthetic array method is utilized. This method of course suffers from grating lobes as discussed in chapter 6.5. However, this may be alleviated by simply dividing the pitch by two, which results in a two way synthetic beam pattern that is nearly identical to the phased or FMC array of double pitch. This pitch reduction was applied to the far field two way beam pattern model, the result of which is displayed below where the Nyquist criteria is intentionally not met for the sake of illustration and the beam is steered to 20^o.

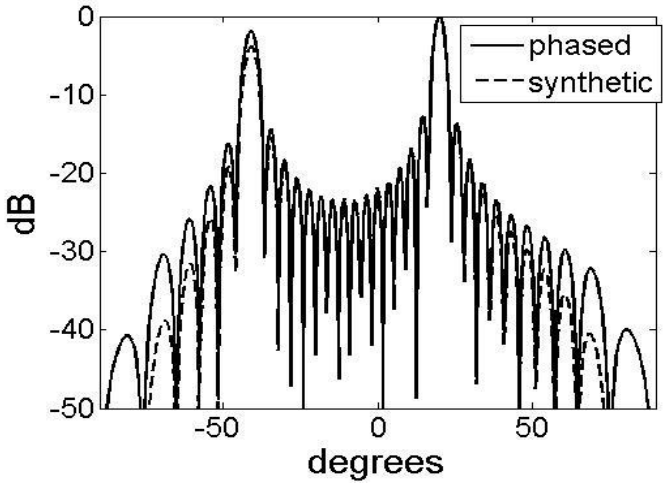

Figure 10-6: Two way beam patterns of a 16 element phased array of λ pitch and a 16 element synthetic array of λ/2 pitch

Now this method is utilized to image a target consisting of three 0.7 mm diameter copper wire immersed in water arranged as shown in Figure 10-7.

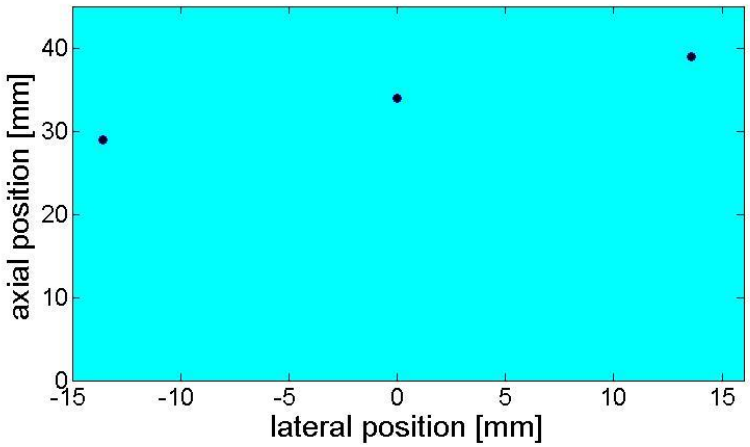

Figure 10-7: 0.7 mm diameter wire targets to be imaged with the synthetic array

The transducer utilized is a comprised of a single slot element 18.24 λ tall and 1.37 λ wide with a center frequency of 2.25 MHz. This transducer produces a 'fairly' wide

beam allowing for a reasonable angular range as shown by the two way absolute amplitude beam plot in Figure 10-8 which has a 3 dB and 6 dB beam width of 19.1 ± 2^{o} and 9.3 ± 1.5^{o} respectively. Ideally the beam would be much wider, however this beam will suffice.

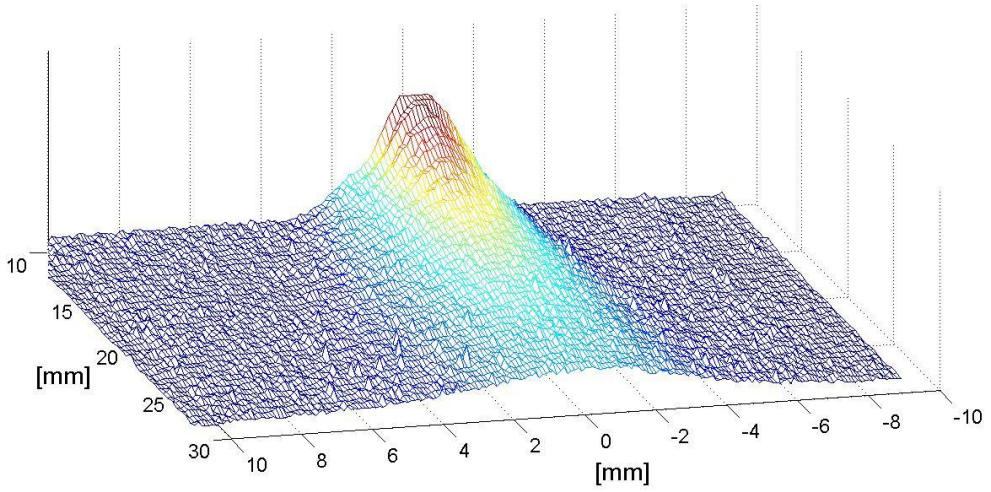

Figure 10-8: Absolute amplitude beam plot of the synthetic array element

The transducer is then scanned laterally in 160 steps of λ/4 or 0.16 mm effectively generating a 160 element synthetic array, the resulting B-scan produced by way of the delay and sum algorithm discussed in chapter 6.5 is shown in Figure 10-9. The sparse arrays considered herein have between 10 and 20 elements, so 160 elements will provide more than enough positions to choose from.

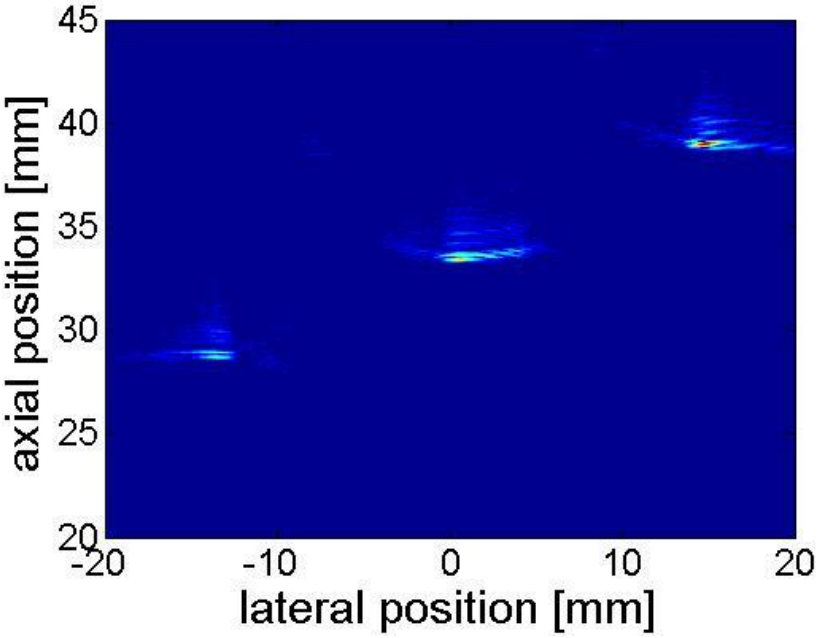

Figure 10-9: B-scan image of three wire target generated by a 160 element λ/4 pitch synthetic aperture

Note in Figure 10-9 the wire at position (-13.6 mm, 28 mm) is the least well resolved in terms of contrast due to the large angle form the array and the directivity of the element.

Now 4 different arrays all containing 10 elements are considered as described in Table 10-2. The resulting B-scan image of an area only containing the center wire is provided in Figure 10-10.

Array Type	Pitch Configuration	Reference
filled	1 1 1 1 1 1 1 1 1	
Restricted Minimum Redundancy	1 2 3 7 7 7 4 4 1	(Moffet, 1968)
Unrestricted Minimum Redundancy	16 1 11 8 6 4 3 2 22	(Moffet, 1968)
Periodic Sparse	3 3 3 3 3 3 3 3 3	

Table 10-2: Configuration of four 10 element arrays utilized to generate B-scans. Note the pitch configuration represents the pitch in λ/4

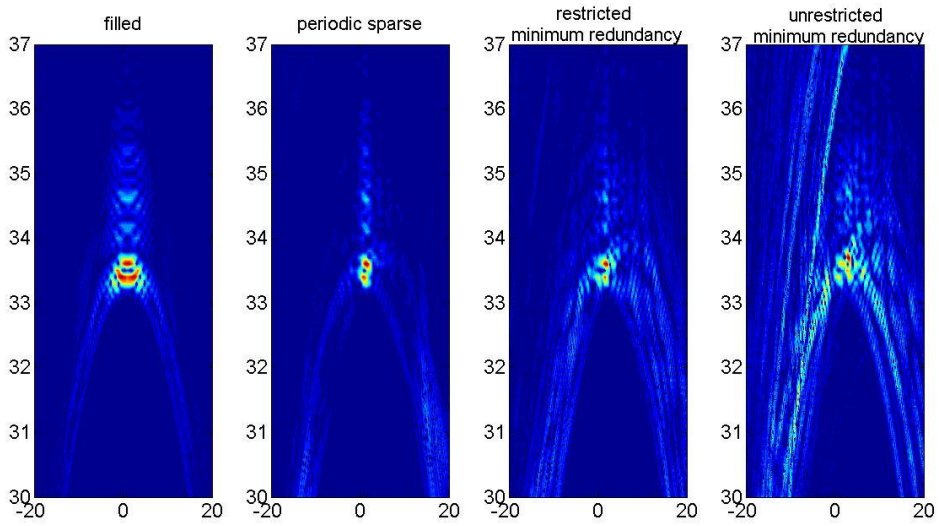

Figure 10-10: B-scans generated by four 10 element arrays. Note the same number of color levels are utilized in each image.

From Figure 10-10 it is apparent that the contrast resolution decreases as the spatial resolution increases for the 3 sparse arrays considered.

Next the procedure is utilized to performed to check the performance of the array designed by (Yang, Chen, & Shi, 2006) with a combination of the genetic algorithm and the minimum redundancy procedure and compare the B-scans to those form an equivalent filled array, sparse periodic and the array developed via the random algorithm in the previous section. One may notice that the periodic sparse array appears, from Figure 10-10, to be a step in the right direction but the side lobe level results a reduction in contrast resolution. Therefore the pitch of the periodic sparse array is pitch is now limited to 2 as opposed to 3. The four arrays compared are:

Array Type	Pitch Configuration	Reference
periodic sparse	2 2 2 2 2 2 2 2 2 2 2 2 2 2 2	
genetic+minimum redundance	1 2 3 3 1 3 3 2 2 2 2 3 4 4 1	(Yang, Chen, & Shi, 2006)
random synthesis	2 1 1 1 1 1 1 1 1 1 1 1 1 1 5	

Table 10-3: Configuration of four 16 element arrays utilized to generate B-scans. Note the pitch configuration is the represents the pitch in λ/4

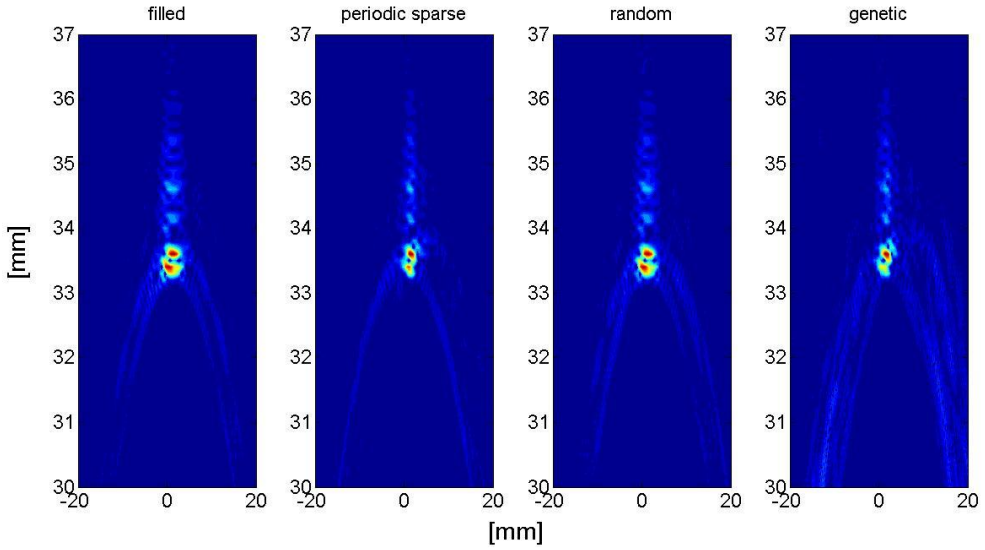

Figure 10-11: B-scans generated by four 16 element arrays. Note the same number of color levels are utilized in each image.

Although, the pictures are very illuminating, at this point it seems important to assign a quantitative measure of an arrays performance in B-scan mode. One first creates a rectangular window including only the center wire. In this window the peak amplitude at the wire location is measured and divided by the average level outside the 6 dB down

area and place into decibel form. The spread function is approximated by counting the number of pixels contained in the 6 dB down area surrounding the wire, since each pixel represents a square 0.1 mm on edge one then converts this to an area and divide by the area of the actual wire, ideally giving a number close to one. The four B-scans of Figure 10-11 are processed in this manner and the results are displayed in Table 10-4.

	Filled	Periodic Sparse	Random	Genetic + Minimum Redundancy
Spread	2.34	1.19	2.2	1.01
Contrast dB	34	37	34	33

Table 10-4: Analysis of b-scan images from the four arrays of 16 elements

For the most part Table 10-4 is self-explanatory and is consistent with what one sees in the B-scan images. At this point one would like to conclude with a judgment as to which array performs the best. This is naturally a context based judgment however it seems clear that the periodic sparse array performs quite well given that it is the best by 3 dB in terms of contrast and is second best in terms of resolution losing to the genetic-minimum redundancy hybrid by only 1.7%. It seems worth pointing out that the assertion that one may improve both contrast and spatial resolution has been confirmed as correct by the periodic sparse array. The uniform sparse array was best in this case due largely to element directivity suppressing the grating lobes.

10.4 Element Position Optimization

Before the details of the optimization procedure are discussed it must be mentioned that it has been found by the author that choosing the appropriate cost function is of utmost importance and this fact cannot be overstated. Specifically a sidelobe distribution which falls off strongly and monotonically is superior to one which has a uniform sidelobe level. This was discovered by trial and error. Even if the array with uniform sidelobes has lower maximum sidelobe level the array producing the monotonic fall off will produce superior B-scans.

In this section the array is optimized by utilizing element position as the degree of freedom. A genetic algorithm which was written by the author in MatLab is utilized. Isotropic elements with continuous wave excitation have been assumed. The element directivity shown in Figure 10-8 is taken advantage of by optimizing the beam pattern of the range of 0 to $\pm$ 40^{o} degrees.

The deterministic approach was the method of choice when affordable and powerful computers where not so common place. As a result one can expect the greatest progress to be had with non-deterministic approaches. There are two other non-deterministic approaches that come to mind. First, the random approach, which has been utilized already, is not likely to find a global minimum. Second, the synthetic annealing algorithm; however, Haupt has shown the genetic algorithm to be superior to this technique.

One must note however, that these algorithms have many tunable parameters and therefore the fact that the genetic algorithm has outperformed the simulated annealing algorithm in one relevant instance is not the end all to be all. The details of writing a MatLab code or outlined in (Haupt & Werner, 2007) and as such will not be explained thoroughly here, but are provided in Appendix B. However, the relevant tuning parameters are listed below

Type	non-binary
Mate selection	roulette wheel
Offspring generation	uniform crossover
Population size	64
Number of naturally selected	14
Mutation percentage	8

In light of the desire to limit the number of electrical leads one begins by considering an array of 4 elements. The most obvious cost function seems to be one in which the main lobe is narrowed and the maximum side lobe level does not exceed that of the uniform sparse array. This was found to be impractical, i.e. could not be achieved after iteration for 8 hours, for less than 12 elements. In the case of 12 elements the beam is shown in Figure 10-12 along with the convergence plot.

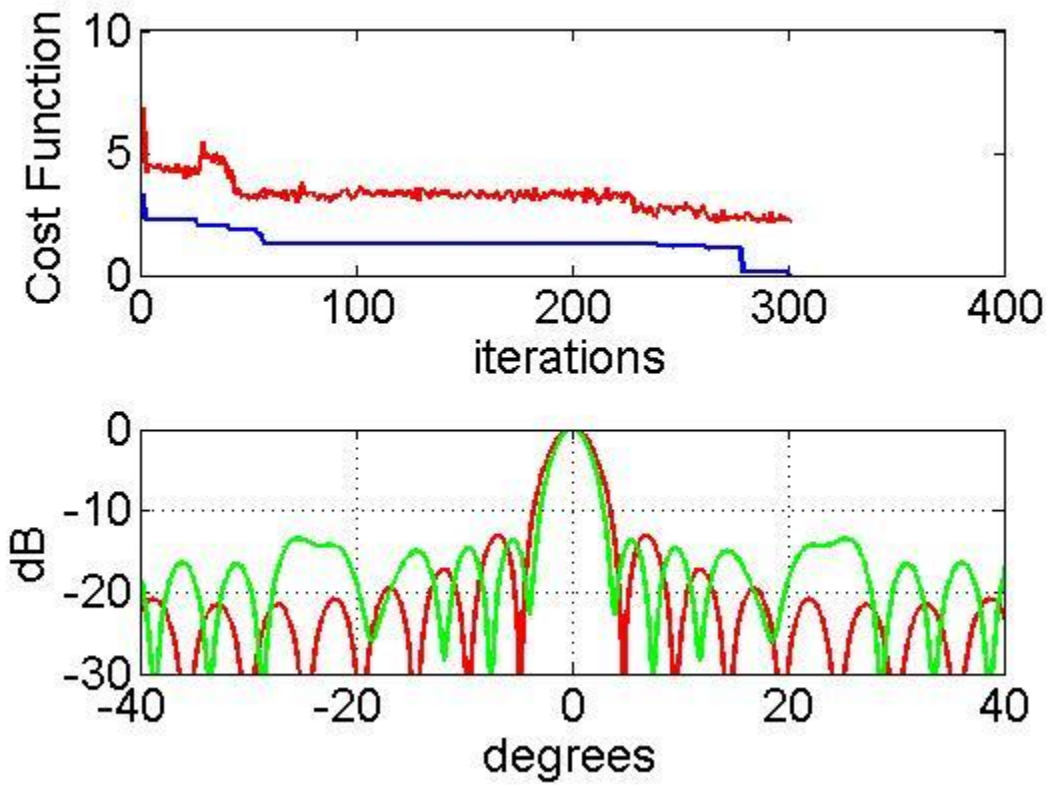

Figure 10-12: 12 element array beam optimized for narrow beam and equivalent SLL, upper image presents the convergence plot with the red indicating the average cost function of the population and the blue showing the minimum cost function. The lower image displays the beam plot of the optimized array in green and the uniform sparse array in red.

The resulting B-scan however has a contrast resolution of 33 dB compared to 35 for the uniform sparse. On the other hand the spread is 1.4 compared to 1.6 for the uniform sparse. The reduction in contrast resolution shows that the far out side lobes have a large impact as can be seen in Figure 10-13.

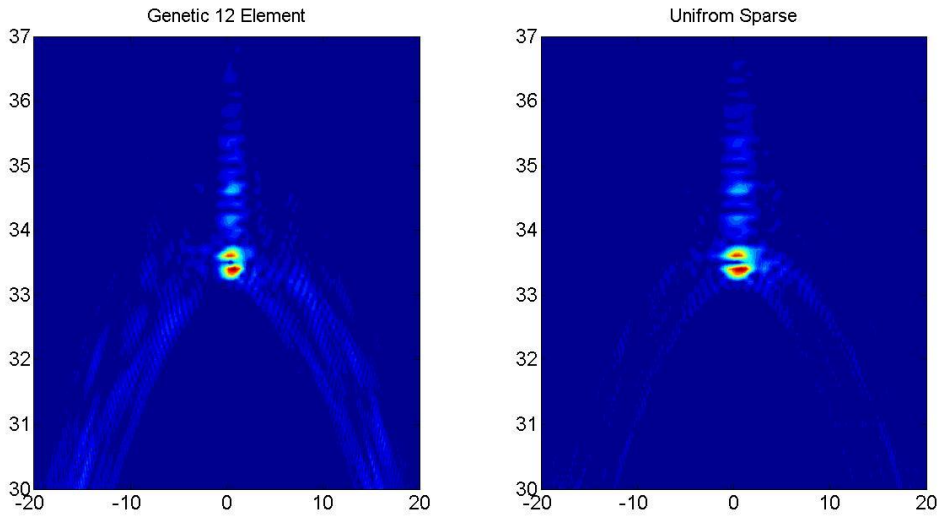

Figure 10-13: B-scans generated by the 12 element arrays genetic and 12 element uniform sparse array. Note the same number of color levels are utilized in each image.

With this knowledge one may now modify the cost function. The cost function of choice is given by the maximum amount by which the generated beam which exceeds desired side lobe level, which is constructed to decrease with angle. After extensive trial and error it was concluded that is necessary to have roughly 32 elements for the genetic sparse array to outperform the uniform array by any significant amount, the resulting B-scans are shown in Figure 10-14.

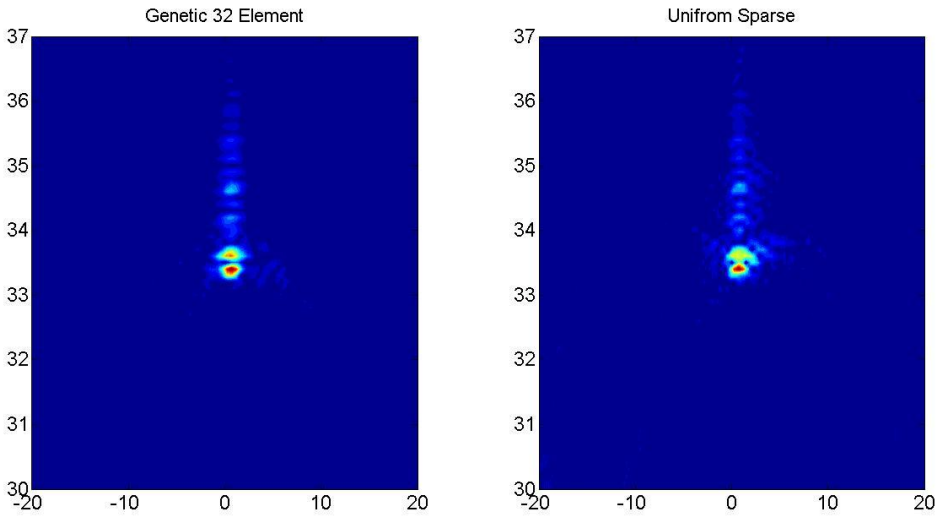

Figure 10-14: B-scans generated by the 32 element arrays genetic and 12 element uniform sparse array. Note the same number of color levels are utilized in each image.

The 32 element genetic array has a contrast resolution of 39 dB compared to 36 for the uniform sparse and an equal spread at 1.09.

10.5 Conclusion

When the element locations are optimized the resulting contrast and spatial resolution was not able to exceed that of the periodic sparse array which was designed by a full enumeration unless many elements are used. The deliberate use of a sparse array is not recommended for the application of interest here.

11 Finite Element Modeling

11.1 Introduction

The finite element method (FEM) is ubiquitous in many engineering fields including ultrasonics. The benefit quickly becomes apparent when one attempts to model the directivity of a phased array with a matching layer, not to mention the backing material. However, the Nyquist criteria must be met when the model is discretized, in fact one should over sample and discretize the model with 10 to 12 degrees of freedom per wavelength (COMSOL Multiphysics User's Guide). As a result when modeling in 2-D the number of DOFs is 144 times the model area when measured in wavelengths and 1728 time the model volume when modeling in 3-D. A typical 64 bit PC is said to be able to handle a few million DOFs at best. In this case the model is that of linear ultrasonic arrays on the order of 10 wavelengths long. Models in this dissertation will include in the transit zone and just beyond, that is, very close to the end of the nearfield which is roughly 100 wavelengths in this case. Given it is desired to model a hemispherical domain in 3-D with absorbing boundary conditions the volume is then just over 2 million wavelengths cubed and one would need some 20 million DOFs which is a bit too much for a typical 64 bit PC to handle. Fortunately there are two solutions to this problem. Solution one is to model the array in two dimensions and assume that the acoustic field is of the separable sort as explained in chapter 9.6 in which case one would need roughly 15 thousand DOFs. Solution two is to utilize a remote connection to the high performance computers provided by Penn State. The system utilized has 48 GB of memory and 12 Intel X 5670 2.93 GHz processors per server. In this dissertation both

methods are utilized as the 3-D model is time consuming even when using the Penn State high performance computers and as such prevents parameter sweeps. Additionally, the remote connection is slow, fickle and subject to random improvements, which makes the interactive aspect of the modeling painful at best.

11.2 Basic Directivity Analysis

To begin consider the baffled single element radiator. Note the change in terminology as the piezoelectric elements are referred to radiators to avoid confusion given that in FEM the model is discretized into "elements". Due to the need to meet the Nyquist criteria with some cushion and given that COMSOL utilizes a second order shape function one must discretize the model with 5 elements per wavelength. In COMSOL the 2-D acoustic module provides some flexibility by allowing one to define the wavenumber in the direction of the dimension which is not being explicitly modeled. The default setting of zero, utilized here, implies the ultrasonic beam does not spread in the neglected direction.

In this model Z-cut AlN is utilized as the radiator which is excited with 25 volts at 5 MHz. The surfaces of the AlN which are not electrode are specified as charge free boundaries. The baffle condition is selected in COMSOL and is therein referred to as a "sound hard boundary". The sound hard boundary condition specifies the following

$$-\hat{n}\left[-\frac{1}{\rho}(\nabla p - q)\right] = 0$$

where $\hat{n}$ is the outward normal from the boundary and q is a dipole term which here is taken as zero. This condition amounts to the normal component of acceleration being zero and hence is a rigid baffle. At the surface of the AlN which is modeled as in direct contact with the fluid one selects continuity of the normal acceleration and thereby relates force in the solid to pressure in the fluid as

$$F = -\hat{n}p.$$

11-2

The last boundary condition to discuss is the boundary which allows energy to leave the system and not be reflected back in the continuous wave analysis. This boundary condition is called a "radiation boundary condition" in COMSOL and one may select plane wave or spherical (cylindrical in 2-D) wave types. Here the cylindrical radiation condition is chosen as is appropriate for a 1 λ wide radiator with the radiation boundary 67 λ from the radiator.

The results of this study are compared to those obtained using a numerical evaluation of the Rayleigh-Somerfield equation with a uniform velocity radiator in Figure 11-1.

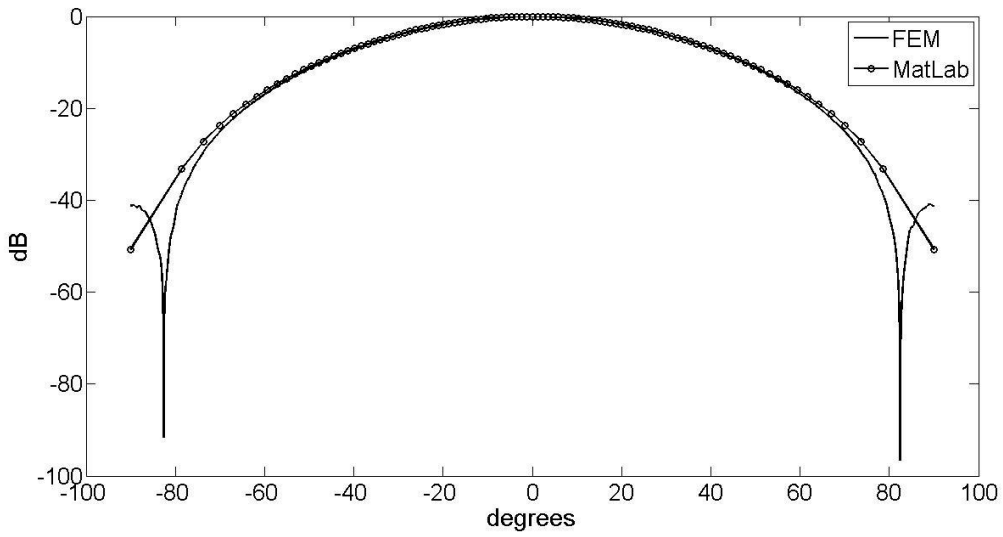

Figure 11-1: Directivity profiles calculated with FEM and numerical evaluation for a 1 λ wide radiator

The directivity profiles are quite similar up to 45 degrees at which point they differ by 0.14 dB. At the extreme edges one observes a large variation which is attributable to the intersection of the sound hard boundary with the radiation boundary. Additionally, the velocity distribution on the piezoelectric element is not uniform in this case since a realistic radiator is being simulated.

11.3 Matching Layer Analysis

The use of a matching layer is a design necessity which complicates the acoustic beam produced by an array element. The need to use radiation hard and mechanically robust materials complicates the matching layer design further, given that such materials will typically possess a high acoustic velocity and therefore, transmit substantial energy from the shear waves generated in the matching layer. This situation is well illustrated in Figure 11-2 where a single AlN array element with a matching layer is modeled in the

time domain via COMSOL. The element is excited with a decaying sinusoidal voltage of the form $V = \sin(\omega t)e^{-\frac{\omega}{2\pi}t}$ which was chosen due to its continuous nature which prevents errors that may be introduced in the FEM analysis when utilizing piecewise functions.

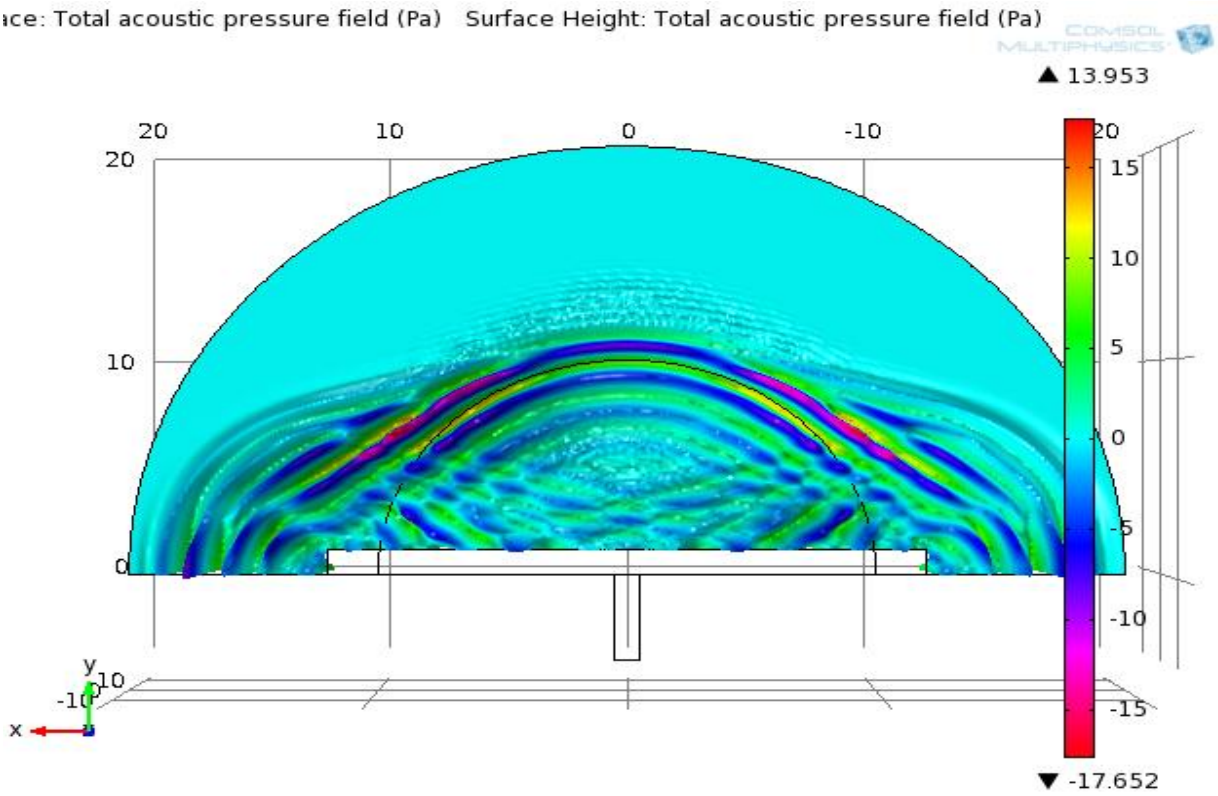

Figure 11-2: Pressure field from a single array element with an aluminum λ/4 matching layer transmitting into water

One can see in Figure 11-2 that the increased transmittance of shear waves from the matching layer creates a complicated beam pattern. The arc midway into the fluid domain in Figure 11-2 is located at roughly 10 λ from the piezoelectric element. For a

more quantitative illustration this arc is used to extract data and generate the polar beam plot below.

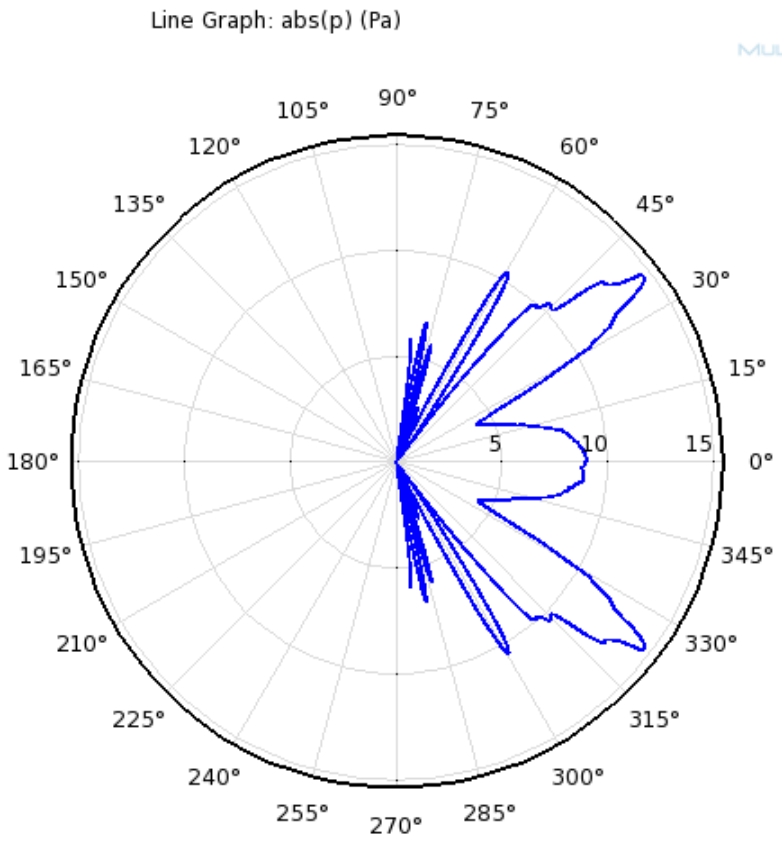

Figure 11-3: Polar beam plot of the pressure filed generated by narrow piezoelectric element with an Al matching layer.

In practice it the matching layer is often diced to prevent these effects (Qi, 1997), (Presque & Fink, 1984) as illustrated in Figure 11-4.

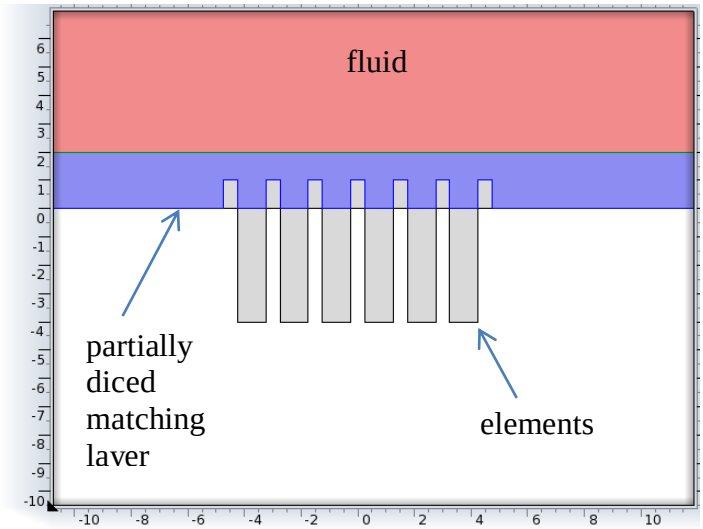

Figure 11-4: Schematic of an array with a partially diced matching layer

This not only prevents the spurious modes but also alters the diffraction of the longitudinal mode within the matching layer. Additionally, the diced region and the space between the elements is typically filled with a low density epoxy. Therefore, a simulation is conducted on a 16 element array of λ/3 wide elements with λ pitch and an Al λ/4 matching layer diced through 75% of the thickness. The filler material has an acoustic velocity of 4.8 mm/μs and a density of 1 g/cm^3. The directivity is thus drastically improved as can be seen in and Figure 11-5 and Figure 11-6. Note, although many elements are present only one is excited in this simulation.

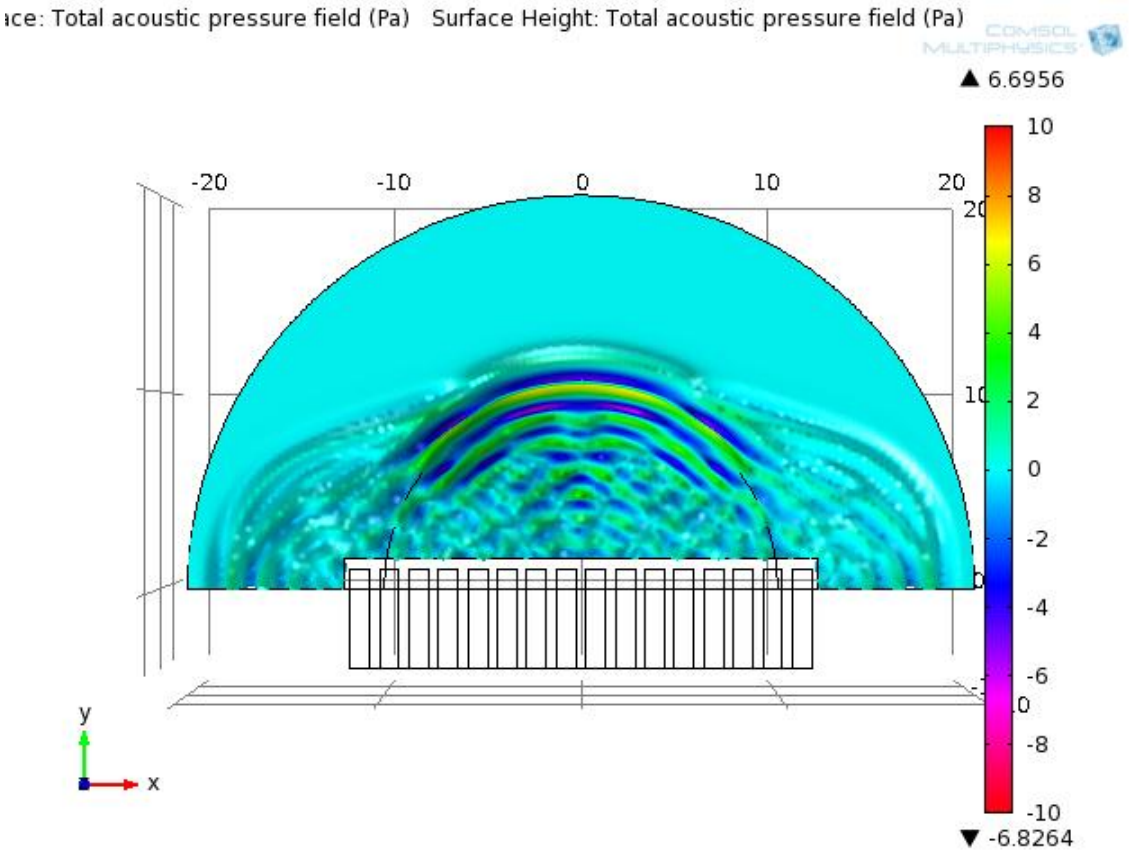

Figure 11-5: Pressure field from a single active array element surrounded by inactive elements with an aluminum λ/4 matching layer transmitting into water. Matching layer dicing, filler and neighboring elements are included and modify the field substantially for the better

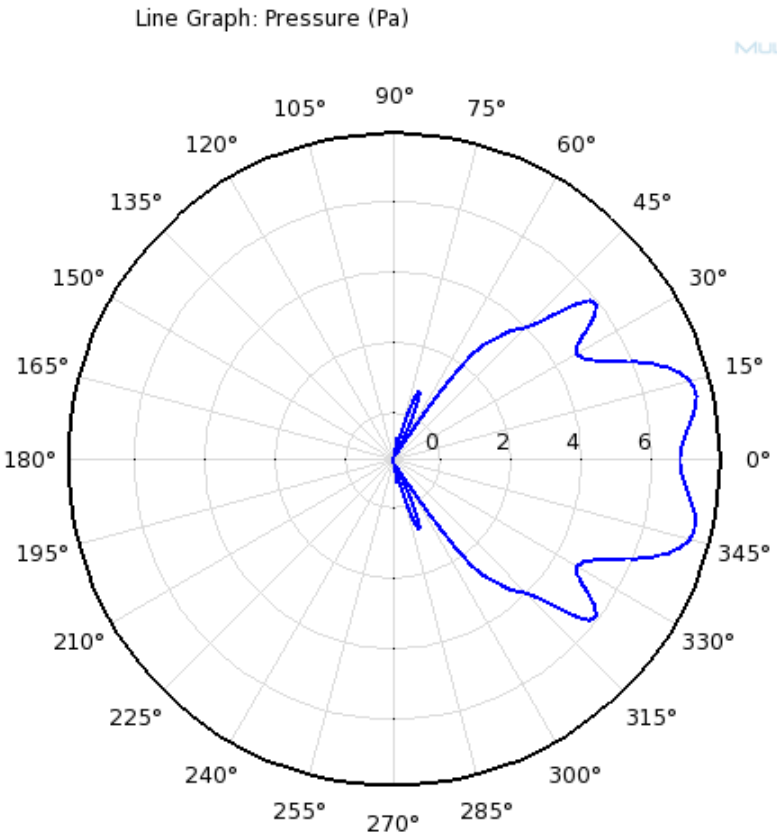

Figure 11-6: Polar plot of the pressure field shown in Figure 11-5

This simulation capability is easily taken a step further by applying time delays to the electrical excitation of each element to achieve a focused beam as illustrated in the following sequence of images where a focal point is chosen at 20 mm axial and 5 mm lateral position.

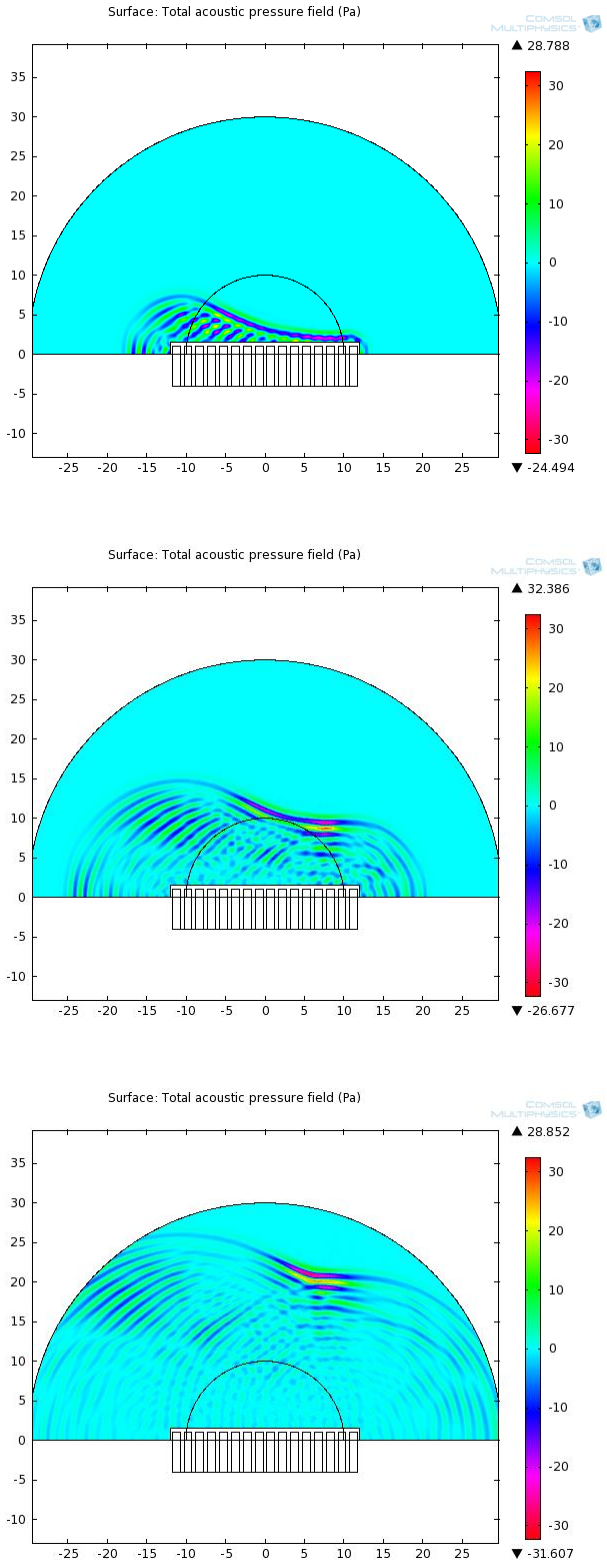

Figure 11-7: sequence in time of a focused array

12 Conclusion

12.1 Theoretical Contributions

This work has made great progress towards the development of an ultrasonic sensor for use in a reactor core. The development of a framework for considering the effects of radiation on piezoelectric materials is provided. The framework indicates that a material must

1. Not depole due to thermal spikes, which will be achieved by selecting a materials with an exceptionally high transition temperature
2. Not be subjected to additional damage and stoichiometric alteration due to atomic species with large transmutation cross sections
3. Not be rendered amorphous by displacement spikes, which will be achieved by selecting a materials with a Wurtzite structure having low topological freedom

This is anything but a trivial task as radiation tolerance has been of interest for many years and many insufficient models have been developed to like damage to effects. Currently no robust model exists for ceramics let alone piezoelectric materials. For example the first calculation that one may make when investigating radiation damage is that of the number of displaced atoms. This calculation is difficult for compound materials and once performed shows that it is not a useful metric. Rather one must utilize the criteria listed above and explained in this dissertation.

The first criteria above was developed by the author by adopting the thermal spike model and assuming it applies to the Curie temperature in the same way it was intended

to apply to the melting temperature. Once this assumption was made it was found that the depoling fluence could be calculated with reasonable accuracy for low Curie temperature piezoelectric materials.

As for the; phased array optimization, limitations where revealed. It was confirmed that a sparse array is not a viable option for the intended application. The optimization procedure was applied to actual data and numerous optimized arrays from the literature where checked experimentally. This was done reconstructing the desired array from a library of waveforms obtained from a 160 element synthetic array which was used to image a simple target. This procedure is entirely new to the best of the author's knowledge. This procedure has great potential for optimizing array performance in complex geometries where theoretical models are preventively arduous.

Lastly, finite element analysis was utilized to check the performance of an array which incorporated only radiation hard materials.

12.2 Experimental Contributions

Atypical passive components and design concepts are necessitated by the harsh conditions, therefore appropriate choices were made and piezoelectric ultrasonic sensors were operated under the following conditions:

1. High temperature 1000^{o} C for 8 hours
2. Elevated temperatures 600^{o} C for 60 hours
3. In a nuclear reactor core for a total fluence of $7.7X10^{18}$ n/cm^2 and a gamma dose of 26.8 MGy over over period of more than 3 months

All the experiments above produced clear A-scan data with at least two significant echoes. The high temperature experiments covered two materials that are entirely new as ultrasonic transducer elements. Specifically the new experiments included:

- Testing of bulk single crystal AlN as a transducer material
- Testing of bulk single crystal YCOB as a transducer material
- Testing of the long term high temperature transduction capability of
    - ALN
    - YCOB
    - $LiNbO_3$

Although, on the surface the latter three experiments seem a bit straightforward, conducting them with repeatable results is not. There is an abundance of literature on high temperature transducers; however the time dependence or thermal cycling dependence of their performance is conspicuously absent. In this work steps have been taken to eliminate the absence of such data in the public realm.

12.3 Future Work

The radiation hardness test was a step in the right direction; however the attainment of data to a higher fluence is desired.

The radiation tolerant array described in this work needs to be built and placed in the reactor to prove the concept to the fullest. This array will consist of the following:

- Piezoelectric: AlN

- Cabling: MgO insulation with stainless steel conductors in a coaxial configuration (Obtainable commercially from thermocoax)
- Matching layer: $\lambda/4$ Aluminum and density tailored $\lambda/4$ TiO_2
- Backing: Stainless steel sponge
- Couplant: Hot isostatic pressed bond with AlN and the $\lambda/4$ Aluminum matching layer

A 1-D array has been considered; however one may wish to increase the inspection volume by increasing the dimension of the array. This naturally requires additional channels, which is undesirable. To this end the author's colleagues have investigated the use of a 1.5 D array which relies on time delays imposed by a physical offset of stacked linear arrays. This method showed promise but appeared to need improvement in regard to the directivity of the linear arrays therein. Utilizing the sparse arrays developed in this work should provide the needed directivity. Alternatively, the linear arrays may be separated by a frequency signature. That is a stack of linear arrays each operating in its own bandwidth. This procedure has been applied by (Gran, Hansen, Nielsen, & Jensen, 2006).

Appendix A: Parameters used in Calculating dpa for PZT

Atomic density	1.36E+22					
Lead						**Averages**
Isotope	2.04E+02	2.06E+02	2.07E+02	2.08E+02		
Abundance	1.40E+00	2.41E+01	2.21E+01	5.24E+01		
spectral average elastic scattering cross section (barn)	4.76E+00	4.82E+00	5.17E+00	6.00E+00		
Macroscopic Cross Section [cm-1]	2.00E-04	3.20E-03	3.10E-03	8.60E-03		
PKA energy keV	9.80E+00	9.71E+00	9.66E+00	9.62E+00		
PKA rate cm^3/s (assuming 10^{14} n/cm^2)	1.82E+10	3.17E+11	3.12E+11	8.57E+11		
Weighted average PKA energy keV	1.37E-01	2.34E+00	2.14E+00	5.04E+00		9.65E+00
Weighted Average PKA rate	2.54E+08	7.63E+10	6.89E+10	4.49E+11		5.95E+11
Displacements caused per PKA						8.70E+01
dpa at 10^21 n/cm^2						3.76E-02
Zirconium						
Isotope	9.00E+01	9.10E+01	9.20E+01	9.40E+01	9.60E+01	
Abundance	5.15E+01	1.12E+01	1.72E+01	1.74E+01	2.80E+00	
spectral average elastic scattering cross section	4.40E+00	4.22E+00	3.90E+00	3.90E+00	4.30E+00	
Macroscopic Cross Section [cm-1]	4.00E-03	8.00E-04	1.20E-03	1.20E-03	2.00E-04	
PKA energy keV	2.22E+01	2.20E+01	2.17E+01	2.13E+01	2.08E+01	
PKA rate cm^3/s (assuming 10^{14} n/cm^2)	4.01E+11	8.39E+10	1.19E+11	1.20E+11	2.13E+10	
Weigthed average PKA energy keV	1.14E+01	2.47E+00	3.73E+00	3.70E+00	5.83E-01	2.19E+01
Weighted Average PKA rate	2.06E+11	9.42E+09	2.03E+10	2.09E+10	5.98E+08	2.58E+11
Displacements caused per PKA						1.75E+02
dpa at 10^21 n/cm^2						3.26E-02

Titanium						
Isotope	4.60E+01	4.70E+01	4.80E+01	4.90E+01	5.00E+01	
Abundance	8.00E+00	7.30E+00	7.38E+01	5.50E+00	5.40E+00	
spectral average elastic scattering cross section	2.70E+00	2.30E+00	2.30E+00	2.80E+00	3.00E+00	
Macroscopic Cross Section [cm-1]	2.00E-04	2.00E-04	1.60E-03	1.00E-04	2.00E-04	
PKA energy keV	4.35E+01	4.25E+01	4.16E+01	4.08E+01	4.00E+01	
PKA rate cm^3/s (assuming 10^{14} n/cm^2)	2.06E+10	1.60E+10	1.62E+11	1.47E+10	1.55E+10	
Weigthed average PKA energy keV	3.48E+00	3.10E+00	3.07E+01	2.24E+00	2.16E+00	4.17E+01
Weighted Average PKA rate	1.65E+09	1.17E+09	1.20E+11	8.08E+08	8.35E+08	1.24E+11
Displacements caused per PKA						2.83E+02
dpa at 10^21 n/cm^2						2.58E-02
Oxygen						
Isotope	1.60E+01	1.70E+01	1.80E+01			
Abundance	9.98E+01	3.90E-02	2.01E-01			
spectral average elastic scattering cross section	2.40E+00					
Macroscopic Cross Section [cm-1]	1.96E-02					
PKA energy keV	1.25E+02					
PKA rate cm^3/s (assuming 10^{14} n/cm^2)	1.96E+12					
Weigthed average PKA energy keV	1.25E+02					1.24E+02
Weighted Average PKA rate	1.96E+12					1.96E+12
Displacements caused per PKA						368
dpa at 10^21 n/cm^2						5.30E-01
total dpa at 10^21 n/cm^2						**5.93E-01**

Appendix B: Genetic Algorithm in MatLab

```
clear
close
clc

%%%%%%%%%%%%%%%%%%%%%%%%%%%%%
%constants
%%%%%%%%%%%%%%%%%%%%%%%%%%%%%
%number of elements
N=16;
%angular range and steering angle
t=0:0.01:20*pi/180;
to=0*pi/180;
%desired side lobe level in dB down;
dB=26;
%desired beam width
width=12;
%minumum pitch in wavelengths
po=1;
%initial population
pop_size=64;
%max pitch
mp=4;
%mutation percent
mut_percent=12;
%number of surviving chromosomes
natsel=8;

%initializing stop watch
tic

%%%%%%%%%%%%%%%%%%%%%%%%%%%%%
%begining of algorithm
%%%%%%%%%%%%%%%%%%%%%%%%%%%%%
iterations=1e5;
for m=1:iterations;

%initial poulation
if m==1;
pop=ceil(mp*rand(pop_size,N-1))*po;
for n=1:pop_size;
q=[0 cumsum(pop(n,:))];
xne(n,:)=q-max(q)/2;
end
else

%natural selection
[cost_sort  ind]=sort(cost);
pop=pop(ind(1:natsel),:);
```

```
parents=1:natsel;

   wheel=[1:natsel]/sum([1:natsel]);
   wheelLL=1-cumsum(wheel);
   wheelUL=[1 wheelLL(1:natsel-1)];

for w=1:natsel;
    r=rand(1,1);
   mate(w,:)=pop((find(wheelLL<r  &  wheelUL>r)),:);
end

%crossover
masks=round(rand(natsel,N-1));
notmasks=abs(masks-1);

%generating offspring
for z=1:pop_size-natsel;
offspring(z,:)=mate(1,:).*masks(1,:)+mate(2,:).*notmasks(1,:);
end
pop=[pop; offspring;];

%mutations
for mut=1:round(mut_percent*pop_size*(N-1)/100);
mutindexr=ceil(pop_size*rand(1));
mutindexc=ceil((N-1)*rand(1));
pop(mutindexr,mutindexc)=ceil(mp*rand(1,1))*po;
end

%formating current polulation for the cost function
for n=1:pop_size;
q=[1+[0 cumsum(pop(n,:))]]*1/2;
xne(n,:)=q-max(q)/2;
end
end

%objective function
for l=1:pop_size;
for n=1:length(xne(1,:));
    xn=xne(l,n);

ui(n,:)=exp(i*2*pi*xn*(sin(t)-sin(to)));

end

%fitness evaluation
u=sum(ui);
u=20*log10(abs(u)/max(abs(u)));
g=diff(u);
cost(l)=std(u(width:length(u)))+30/max(abs(u(width:length(u))))+dB/abs(
max(u(width:length(u))));
end
COSTm(m)=min(cost);
COSTa(m)=mean(cost);
```

```
[100*m/iterations COSTm(m)]

%stoping algorithm if desired patern is obtained
 if COSTm(m)<1
         FIT=pop(find(cost==min(cost)),:);
     break
 end

 %saving the best configuration thus far
 if COSTm(m)<=min(COSTm)
  FIT=pop(find(cost==min(cost),1,'first'),:);
 end


end
%reporting time for completion
toc

%ploting the cost against iterations
plot(COSTm,'.')
hold on
plot(COSTa,'r.')
```

References

Agrawal, V. D., & Lo, Y. T. (1972). Mutual Coupling in Phased Arrays of Randomly Spaced Antennas. *AP-2*(3).

Anon. (1971). *Evaluation of Irradiation Test Results for Candiate NERVA Piezoelctric Accelerometers, Ground Test Reactor Irradiation Test No. 22.* Aerojet Nuclear Systems Company.

Atobe, K., Okada, M., & Nakagawa, M. (2000). Irradiation temperature dependence of defect formation of nitrides. *Nuclear Instruments and Methods in Physics Research B*, 57-63.

Baba, A., Searfass, C., & Tittmann, B. (2010). High temperature ultrasonic transducer up to 1000 °C using lithium niobate single crystal. *Applied Physics Letters* .

Bae, M. H., Sohn, I. H., & Park, S. B. (1991). Grating Lobe Reduction in Ultrasonic Synthetic Focusing. *Electronics Letters.*

Baranov, V. M., & Martynenko, S. P. (1982). Durabiloty of ZTL Piezoceramic Under the Action of Reactor Irradiation. *Translated from Atomnaya Energiya*, 5.

Becquart, C. S., Domain, C., & Society, M. (2010). Modeling Microstructure and Irradiation Effects. *Metallurgical and Materials Transactions A, 42A*, 852-870. doi:10.1007/s11661-010-0460-7

Begaud, X. (2011). *Ultra Wide band Antennas.* Hoboken: Wiley.

Braun, F. K. (1909, December 11). *Electrical oscillations and wireless telegraphy*. Retrieved August 3, 2011, from Nobelprize.org: December 11, 1909

Brinkman, J. A. (1954). On the Nature of Radiation Damage in Metals. *Journal of Applied Physics*, *25*(8), 961. doi:10.1063/1.1721810

Broomfield, G. H. (1984). High Temperature nad Post Irradiation Piezoelectric Properties of Strontium Niobate. *The Mettalurgist and Materials Technologist, 16*(10), 515-520.

Bucci, O. M., D'Urso, M., Isernia, T., Angeletti, P., & Toso, G. (2010). Deterministic Sythesis of Uniform Amplitude Sparse Arrays via New Density Taper Techniques. *IEEE Transaction on Antennas and Propagation*, 1949.

Chadderton, L. T. (1964). *Radiation Damage in Crystals.* New York: John Wiley & Sons.

Chilton, A., Shultis, J., & Faw, R. (1984). *Principles of Radiation Shielding.* Englewood Cliffs: Prentice-Hall.

Chynoweth, A. (1959). Radiation Damage Effects in Ferroelectric Triglycine Sulfate. *Physical Review*, *113*(1), 159-166. doi:10.1103/PhysRev.113.159

Claeys, C., & Simoen, E. (2002). *Radiation Effects in advanced Semiconductor Materials and Devices.* Springer-Verlag.

Collin, R. E., & Zucker, F. J. (1969). *Antenna Theory part 1* (Vol. 7). McGraw-Hill.

Coltman, R., Klabunde, C., & Redman, J. (1967). Survey of Thermal-Neutron Damage in Pure Metals. *Physical Review*, *156*(3), 715.

COMSOL Multiphysics User's Guide. (2011)

Dienes, G. J., & Vineyard, G. H. (1957). *Radiation Effects in Solids.* New York: Interscience Publishers Inc.

Evaluated Nuclear Data File (ENDF) . (2011). Retrieved September 2011, from IAEA Nuclear Data Services: http://www-nds.iaea.org/exfor/endf.htm

Foster, A. R., & Wright Jr., R. L. (1983). *Basic Nuclear Engineering.* Englewood Cliffs: Prentice-Hall.

Friedland, E. (2007). Influence of electronic stopping on amorphization energies. *Surface Coating and Technology*, *201*, 8220-8224. doi:10.1016/j.surfcoat.2006.01.095

Genral Catalog. (1989). *Endevco Div.* . San Juan Capistrano, CA: Allied Signal.

Glower. (1965). Effects of Radiation-Induced Damage Centers in Lead Zirconate Titanate Ceramics. *Journal of The American Ceramic Society*, *48*(8), 417-421.

Goodman, J. W. (1968). *Introduction to Fourier Optics.* San Francisco: McGraw Hill.

Gran, F., Hansen, K., Nielsen, M., & Jensen, J. (2006). Preliminary in-vivo Results for Spacially Coded Synthetic Transmit Aperrture Ultrasound Based on Frequency Division. *IEEE Ultrasonics Symposium* (p. 1086). IEEE.

Hansen, R. (1997). *Phased Array Antennas.* New Jersey: Wiley Interscience Publications.

Haupt, R. L., & Werner, D. H. (2007). *Genetic Algorithms in Electromagnetics.* Hoboken: Wiley-Interscience.

Hobbs, L. W. (1995). The role of topology and geometry in the irradiation-induced amorphization of network structures. *Journal of Non-Crystalline Solids*, *182*, 27-39.

Hobbs, L. W., Clinard, F. W., Zinkle, S. J., & Ewing, R. C. (1994). Radiation effects in ceramics. *Journal of Nuclear Materials*, *216*, 291-321. doi:10.1016/0022-3115(94)90017-5

Hobbs, L. W., Jesurum, C. E., & Berger, B. (1999). RIGIDITY CONSTRAINTS IN AMORPHIZATION OF SINGLY AND MULTIPLY-POLYTOPIC STRUCTURES. In Thorpe & Duxbury (Eds.), *Rigidity Theory and Applications* (pp. 191-216). Kluwer Academic/Plenium Publishers.

Hodgson, E. R., & Agullo-Lopez, F. (1987). OXYGEN VACANCY CENTRES INDUCED BY ELECTRON IRRADIATION IN LiNbO3. *Solid State Communications, 64*(6), 965-968.

Holbert, K., Sank, S., & McCready, S. (2005). Response of Lead Metaniobate Acoustic Emission. *IEEE TRANSACTIONS ON NUCLEAR SCIENCE*, 2583-2590.

Ito, Y., Yasuda, K., Ishigami, R., Sasase, M., Hatori, S., Ohashi, K., et al. (2002). Radiation Damage of Materials Due to High Energy Ion Irradiation. *Nuclear Instruments and Methods in Physics Research*, 530.

Jorgensen, P. J., & Bartlett, W. R. (1969). HIGH TEMPERATURE TRANSPORT PROCESSES IN Lithium Niobate. *J. Phys. Chem. Solids*, 2639-2648.

Kažys, R., Voleišis, A., & Voleišienė, B. (2008). High temperature ultrasonic transducers: review. *ULTRAGARSAS (ULTRASOUND), Vol.63(2).*

Kazys, R., Voleisis, A., Sliteris, R., Maze, L., Van Nieuwenhove, R., Kupschus, P., et al. (2005). High Temperature Ultrasonic Transducers for Imaging and Measurements in a Liquid Pb/Bi Eutectic Alloy. *ieee transactions on ultrasonics, ferroelectrics, and frequency control,*, 525-537.

Kok, K. D. (2009). *Nuclear Engineering Handbook.* CRC Press.

Krautkramer, J., & Krautkramer, H. (1977). *Ultrasonic Testing of Materials.* Springer Verlag.

Kucheyev, S. O., Williams, J. S., Zou, J., Jagadish, C., Pophristic, M., Guo, S., Ferguson, I. T., et al. (2002). Ion-beam-produced damage and its stability in AlN films. *Journal of Applied Physics, 92*(7), 3554. doi:10.1063/1.1501746

Lee, J., Lee, M., Kim, J., Luk, V., & Jung, Y. (2006). A study of the characteristics of the acoustic emission signals for condition monitoring of check valves in nuclear power plants. *Nuclear Engineering and Design, 236*(13), 1411-1421. doi:10.1016/j.nucengdes.2006.01.007

Lefkowitz, I. (1958). Radiation-Induced Changes in the Ferroelectric Properties of Some Barium Titanate-Type Materials. *J. Phys. Chem. Solids, 10*, 169-173.

Lockwood, G. R., Li, P.-C., O'Donnell, M., & Foster, F. S. (1996). Optimizing the Rdaiation Pattern of Sparse Periodic Linear Arrays. *IEEE Transactions on Ultrasonic Ferroelectric and Frequancy Control*, 7.

Macovski, A. (1979). Ultrasonic Imaging using arrays. *IEEE* (pp. 484-495). IEEE.

Mahafza, B. R. (2009). *Radar signal analysis and processing using MATLAB* (Vol. 1). Boca Raton: CRC Press.

Meldrum, A., Boatner, L. A., Weber, W. J., & Ewing, R. C. (2002). Amorphization and recrystallization of the ABO 3 oxides. *Journal of Nuclear Materials*, *300*, 242-254.

Meleshko, Y. P., Babaev, S. V., Karpechko, S. G., Nalivae, V. I., Safin, Y. A., & Smirnov, V. M. (1984). STUDYING TIIE ELECTROPHYSICAL PARAMETERS OF PIEZOCERAMICS OF VARIOUS TYPES IN AN IVV-2M REACTOR. *Translated from Atomnaya ~nergiya,*, 111-114.

Meleshko, Y., Karpechko, S., Leont'ev, G., Nalivaev, V., Nikiforov, A., & Smirnov, V. (1986). RADIATION RESISTANCE OF THE PIEZOELECTRIC CERAMICS TsTS-21 AND TNV-I. *Translated from Atomnaya Energiya*, *61*(1), 50-52.

Miclea, C., Tanasoiu, C., Miclea, C. F., Spanulescu, I., & Cioangher, M. (2005). Effect of neutron irradiation on some piezoelectric properties of PZT type ceramics. *Romania, 128*, 115-120. doi:10.1051/jp4

Moffet, A. T. (1968). Minimum-Redundancy Linear Arrays. *AP-16*(2).

Mrowec, S. (1980). *Defects and Diffusion in Solids.* New York: Elsevier Scientific Publishing.

Naguib, H., & Kelly, R. (1974). Criteria for Bombardment-Induced Structural Changes in Non-Metallic Solids. *Radiation Effects, 25*, 1-12.

P.V. Vladimirov, D. L. (1998). Damage calculation in fusion ceramics: comparing neutrons and light. *Journal of Nuclear Materials*, 104–112.

Parks, D. A., Tittmann, B. R., & Kropf, M. M. (2009). Aluminum Nitride as a High Temperature Transducer. *Quantatative Nondestructive Evaluation*, 1029-1034.

Patel, N. D., & Nicholson, P. S. (1990). High Frequency - High Temperature Ultrasonic Transducers. *NDT International*, 262-266 .

Pavlov, P., Zorin, E., Tetelbaum, V., Lesnikov, G., Ryzhkov, G., & Pavlov, A. (1973). Phase Transformations at Bombardment of A1 and Fe Polycrystalline Films with B+, C+, N+, P+, and As+ Ions. *PHYS STATUS SOLIDI A, a19*, 373-378.

Phani, K., Sanyal, D., & Sengupta, a. (2007). Estimation of elastic properties of nuclear fuel material using longitudinal ultrasonic velocity – A new approach. *Journal of Nuclear Materials, 366*(1-2), 129-136. doi:10.1016/j.jnucmat.2006.12.045

Pool, R. (2011). FUKUSHIMA: THE FACTS. *Engineering & Technology*, *112*(4), 221-2. Retrieved from http://www.ncbi.nlm.nih.gov/pubmed/21819007

Presque, P., & Fink, M. (1984). Effect of Planar Baffle Impedance on the Acoustic radiation of a Phased Array Element Theory and Experiment. *Ultrasonics Symposium* (pp. 1034–1038). IEEE.

Primak, W., & Anderson, T. (1975). Metamimictization of Lithium Niobate by Thermal Neutrons. *Nuclear Technology*, *23*, 235.

Qi, W. (1997). *Piezocomposite Transdcuer and Transdcuer Array Design for Medical Ultrasonic Imaging.* University Park: PSU PhD Dissertation.

Rauschenbach, B. (2000). Ion Implantation, Isolation and Thermal Processing of GaN and Related Materials. In M. Omar, *III-Nitride Semniconductors, Structural and Defects Properties* (pp. 193-249). Amsterdam: Elsevier Science B.V.

Ritter, T. (2000). Design, Fabrication and Testing of High Frequency (>20 MHz) Composite Ultrasound Imaging Arrays. *PhD Dissertation*. University Park: Penn State University.

Rogers, F. T. (1956). Effect of Pile Irradiation on the Dielectric Constant of Ceramic BaTiO3. *Journal of Applied Physics*, *27*(9), 1066. doi:10.1063/1.1722542

S.B. Ubizskii, A. M.-U. (2000). Radiation displacement defect formation in some complex oxide. *Nuclear Instruments and Methods in Physics Research*, 40-46.

Şahin, D., & Kenan , Ü. (2009). Activity, exposure rate and spectrum prediction with Java programming . *Journal of radioanalytical and nuclear chemistry 282*(1).

Schmarje, N., Kirk , K. J., & Cochran, S. (2007). 1–3 Connectivity lithium niobate composites for high temperature operation. *Ultrasonics 47*.15-22

Schmerr, L. W., & Song, S.-J. (2007). *Ultrasonic Nondestructive Evaluation Systems Models and Measurements.* New York: Springer.

Sickafus, K. E., Kotomin, E. A., & Ub, B. P. (2007). *Radiation Effects in Solids (Proceedings of the NATO Advanced Study Institute on Radiation Effects in Solids).* Springer NATO Science Series: Erice, Sicily, Italy.

Sinha, M., & Buckley, D. (2007). Acoustic Properties of Polymers. In J. E. Mark, *Physical Properties of Polymers Handbook* (pp. 1021-1031). New York: Springer.

Stubbs, D., & Dutton , R. (1996). High-Temperature Ultrasonic Sensor for in Situ Monitoring of Hot Isostatic Processing. *SPIE*, 164-172.

Svaasand, L., Eriksrud, M., Nakken, G., & Grande, A. P. (1974). SOLID-SOLUTION RANGE OF L1NbO3. *Journal of Crystal Growth*, *22*(January), 230-232.

Szabo, T. (2004). *Diagnostic Ultrasound Imaging: Inside Out.* Elsevier Academic Press.

Szenes, G. (2005). Ion-induced amorphization in ceramic materials. *Journal of Nuclear Materials*, *336*, 81-89. doi:10.1016/j.jnucmat.2004.09.004

Szenes, G. (2011). Thermal spike analysis of ion-induced tracks in semiconductors. *Nuclear Inst. and Methods in Physics Research, B*, *269*(19), 2075-2079. Elsevier B.V. doi:10.1016/j.nimb.2011.06.014

Thomas, R. L. (1973). *Vibration Instrumentation for Nuclear Reactors (Endevco Technical Paper 258).* Pasadena: Endevco.

Thomas, R. L. (1973). *Vibration Instrumentation for Nuclear Reactors (Endevco Technical Report 258)* (pp. 1-8).

Tipping, P. (1996). LIFETIME AND AGEING MANAGEMENT OF NUCLEAR POWER PLANTS: A BRIEF OVERVIEW OF SOME LIGHT WATER REACTOR COMPONENT AGEING. *Int. J. Pres. Ves. & Piping*, *66*, 17-25.

Trachenko, K. (2004). Understanding resistance to amorphization by radiation damage. *Journal of Physics: Condensed Matter*, *16*(49), R1491-R1515. doi:10.1088/0953-8984/16/49/R03

Turner, R. C., Fuierer, P. A., Newnham , R. E., & Shrout, T. R. (1994). Materials for High Temperature Acoustic and Vibration Sensors: A Review. *Applied Acoustics*, 299-324.

Villard, J.-f, & Schyns, M. (2009). Innovations for in-pile measurements in the framework of the CEA-SCK • CEN Joint Instrumentation Laboratory. *Osiris*.

Vives, A. A. (2008). *Piezoelectric Transducers and Applications.* Berlin: Springer.

Wittels, M. C., & Sherril, F. A. (1954). Radiation Damage in Si02 Structures. *Advances in Physics*, *93*(5), 1117.

Wittels, M. C., & Sherrill, F. a. (1957). Fast Neutron Effects in Tetragonal Barium Titanate. *Journal of Applied Physics*, *28*(5), 606. doi:10.1063/1.1722811

Yang, P., Chen, B., & Shi, K.-R. (2006). A novel method to design sparse linear arrays. *Ultrasonics*, e717.

Yano, T., Inokuchi , K., Shikama , M., & Ukai , J. (2004). Neutron irradiation effects on isotope tailored aluminum aluminum nitride ceramics by a fast reactor up to 2 · l026 n/m2. *Journal of Nuclear Materials* , 1471–1475.

Zhang, S, Fei, Y., Frantz, E., Snyder, D., Chai, H., & Shrout, T. (2008). High-Temperature Piezoelectric Single Crystal ReCa4O(BO3)3 for Sensor Applications. *IEEE transactions on ultrasonics, ferroelectrics, and frequency control*, *55*(12), 2703.

Zhang, Shujun, & Yu, F. (2011). Piezoelectric Materials for High Temperature Sensors. *J. Am. Ceram. Soc.*, *94*(10), 3153. doi:10.1111/j.1551-2916.2011.04792.x

Zheng, Y., Martinez, C., Easton, D., Park, G., & Farinholt, K. (2011). Sensor Self-Diagnostics for Piezoelectric Transducers Operating in Harsh Environments. *Industrial and Commercial Applications of Smart Structures Technologies 2011*. SPIE.

Zhu, J. (2008). Optimization of Matching Layer Design for Medical Ultrasonic Transducer. *PhD Dissertation*. The Penn State University.

Ziegler, J. F., Biersack, J. P., & Ziegler, M. D. (2008). *SRIM The Stoppoing and Range of Ions in Matter*. Chester: SRIM Co.

Zingle, S., Snead, L., Eartherly, W., Jones, J., & Hensley, D. (1991). *Effect of Low temperature Ion Irradiation on the Microstrucure of Nitride Ceramics*.

VITA

David A Parks was born in Corvallis Oregon on January 20th 1981. He received his Bachelor's degree with honors in physics from Millersville University of Pennsylvania in 2005, followed by a Masters in Engineering Science and a PhD in Engineering Science and Mechanics from the Pennsylvania State University in 2007 and 2012 respectively.